

**ω Meson Production
in the $pn \rightarrow d\omega$ Reaction
at ANKE**

Inaugural-Dissertation
zur
Erlangung des Doktorgrades
der Mathematisch-Naturwissenschaftlichen Fakultät
der Universität zu Köln

vorgelegt von
Inti Lehmann
aus Juliaca – Peru

Köln, 2003

Berichterstatter:

Prof. Dr. H. Ströher
Prof. Dr. J. Jolie

Tag der mündlichen Prüfung: 4. Juni 2003

Abstract

In the framework of this thesis a first measurement of the $pn \rightarrow d\omega$ total cross section has been performed at mean excess energies of $Q \approx 26$ and 60 MeV. The motivation, apparatus, analysis, results and their tentative interpretation are discussed in the following.

The comparison of the cross sections for meson production in proton-proton and proton-neutron collisions close to threshold, constrain theoretical models describing the production mechanisms. For η production the observed cross section ratio $R = \sigma_{\text{tot}}(pn \rightarrow pn\eta)/\sigma_{\text{tot}}(pp \rightarrow pp\eta) \approx 6.5$ is generally attributed to isovector dominance in model calculations based on meson exchange. It is therefore interesting to investigate whether a similar isospin dependence is found also for the ω , the next heavier isoscalar meson. Relatively few experiments were performed for the $pp \rightarrow pp\omega$ reaction, but in proton-neutron collisions no data whatsoever are available.

The $pn \rightarrow d\omega$ reaction was studied in the $pd \rightarrow p_{\text{sp}}d\omega$ reaction at four proton beam momenta between 2.6 and 2.9 GeV/c at the ANKE spectrometer of COSY-Jülich. A deuterium cluster-jet target was used as an effective neutron target, detecting the low momentum recoil protons (p_{sp}), which have momenta of about 80 MeV/c, in a silicon telescope placed close to the target. These recoil protons can be treated as “spectators” that influence the reaction only through their modification of the kinematics. By variation of angle and momentum of the spectator protons, a certain range in excess energy Q is selected experimentally. This range is used to extract results in pn collisions for the corresponding Q values. The deuterons emitted at angles below 8° with a momenta around 2 GeV/c were detected in the forward system of the ANKE spectrometer. Inclined Čerenkov counters in combination with two layers of scintillation counters enabled us to identify these deuterons despite a two orders of magnitude higher proton background. Their momenta were reconstructed using the information from two multi-wire proportional chambers. The $pn \rightarrow d\omega$ reaction was then identified *via* the missing mass technique. In order to normalise the data, first the efficiencies of all detectors were evaluated. Secondly the absolute luminosity was determined by the pd elastic scattering reaction, employing the possibility to identify slow deuterons simultaneously in the silicon telescope.

Measurements in $pp \rightarrow pp\omega$ at SATURNE show there to be a strong contribution from multi-pion production below the ω peak in the missing mass spectrum. This can only be reliably estimated by comparing data above and below the ω threshold. Used are the experimental data at 2.6 , 2.7 , 2.8 and 2.9 GeV/c beam momentum, which correspond to mean Q values in $pn \rightarrow d\omega$ of -40 , -5 , 26 and 60 MeV respectively. At the highest energy, there is clear evidence for an ω peak, whereas at 2.8 GeV/c the residual ω signal depends much

more sensitively upon the background description. The cross sections extracted for $pn \rightarrow d\omega$ at $Q \approx 26$ MeV and 60 MeV are significantly smaller than theoretical predictions. This suggests that the reaction mechanism for ω production differs from the one for the η , possibly implying a relatively larger contribution from isoscalar meson exchange. Measurements with higher precision in both Q and in cross section are scheduled already for August 2003. The results are expected to shed even further light on the basic production mechanisms.

Zusammenfassung

Im Rahmen dieser Arbeit wurde eine erste Messung des Wirkungsquerschnittes der Reaktion $pn \rightarrow d\omega$ bei Überschußenergien $Q \approx 26$ bzw. 60 MeV durchgeführt. Motivation, experimenteller Aufbau, Analyse der Daten, Ergebnisse und deren Interpretationsmöglichkeiten werden im folgenden dargelegt.

Der Vergleich der Wirkungsquerschnitte schwelennaher Meson-Produktionsreaktionen in Proton-Proton und Proton-Neutron Stößen läßt in theoretischen Modellen Rückschlüsse auf Produktionsmechanismen zu. So wird das in der η -Produktion gefundene Verhältnis $R = \sigma_{\text{tot}}(pn \rightarrow pn\eta)/\sigma_{\text{tot}}(pp \rightarrow pp\eta) \approx 6.5$ in auf Meson-Austausch basierenden Modellrechnungen gewöhnlich einer Isovektordominanz in dieser Reaktion zugeschrieben. Es ist deshalb von hohem theoretischen Interesse, herauszufinden, ob sich für das ω -Meson, das nächstschwerere isoskalare Meson, eine ähnliche Isospinabhängigkeit ergibt. In der Reaktion $pp \rightarrow pp\omega$ wurden bisher relativ wenige Experimente durchgeführt, für Proton-Neutron-Stöße existieren sogar gar keine Daten.

Die Reaktion $pn \rightarrow d\omega$ wurde durch den Nachweis der Reaktion $pd \rightarrow p_{\text{sp}}d\omega$ bei vier Strahlimpulsen zwischen 2.6 und 2.9 GeV/c am ANKE-Spektrometer am Beschleuniger COSY in Jülich untersucht. Als effektives Neutronen-Target diente ein sogenanntes Deuterium-Cluster-Jet-Target, unter Nachweis der langsamen Rückstoßprotonen (p_{sp}) mit Impulsen um die 80 MeV/c in einem Silizium-Teleskop in Targetnähe. Diese Protonen können als sogenannte „Spektatoren“ – also nicht am Prozess der Meson-Produktion beteiligte Zuschauer – einzig durch ihren Einfluß auf die Reaktionskinematik berücksichtigt werden. Experimentell wird durch deren Verteilung ein gewisser Bereich in der Überschußenergie Q festgelegt, der genutzt werden kann, um Wirkungsquerschnitte in pn -Reaktionen zu bestimmen. Deuteronen, welche unter kleinen Winkeln mit ca. 2 GeV/c Impuls emittiert werden, wurden im Vorwärts-System des ANKE-Spektrometers nachgewiesen. Trotz eines um zwei Größenordnungen höheren Proton-Untergrundes wurde die Identifikation dieser Deuteronen durch geneigte Čerenkov-Zähler in Kombination mit zwei Lagen von Szintillationszählern ermöglicht. Die Impulse wurden durch die Informationen aus zwei Vieldraht-Proportionalkammern rekonstruiert. Damit konnten Ereignisse aus der Reaktion $pn \rightarrow d\omega$ mit Hilfe der fehlenden Masse („Missing Mass“) bestimmt werden. Um die Daten zu normieren, wurden einerseits die Effizienzen aller Detektoren bestimmt. Andererseits wurden Ereignisse aus elastischer Proton-Deuteron-Streuung unter dem Nachweis von langsamen Deuteronen im Silizium-Teleskop genutzt, um die absolute Luminosität zu ermitteln.

Messungen im $pp \rightarrow pp\omega$ Kanal an SATURNE haben gezeigt, daß unter dem ω -Peak im „Missing-Mass“-Spektrum ein beträchtlicher Beitrag der Viel-Pionen-Produktion vorliegt. Die Stärke dieses Untergrundes kann nur zu-

verlässig abgeschätzt werden, indem Ergebnisse oberhalb und unterhalb der ω -Schwelle miteinander verglichen werden. Hierzu wurden die Daten bei 2.6, 2.7, 2.8 und 2.9 GeV Strahlimpuls, die mittleren Q -Werten von -40, -5, 26 bzw. 60 MeV in $pn \rightarrow d\omega$ entsprechen, genutzt. Bei der höchsten Energie besteht ein eindeutiges Signal für die Produktion von ω -Mesonen, wogegen der Beitrag bei 2.8 GeV/c viel stärker von der Beschreibung des Untergrundes abhängt. Die ermittelten Wirkungsquerschnitte für $pn \rightarrow d\omega$ bei $Q \approx 26$ MeV bzw. 60 MeV sind bedeutend niedriger als theoretischen Voraussagen. Dies legt den Schluß nahe, daß der Reaktionsmechanismus in ω - und η -Produktion unterschiedlich ist, was eventuell einen stärkeren Beitrag isoskalaren Mesonaustausches vermuten läßt. Messungen mit höherer Genauigkeit, sowohl in Q als auch im Wirkungsquerschnitt, sind für August 2003 geplant. Es wird erwartet, daß deren Ergebnisse noch genauere Aufschlüsse über die grundlegenden Produktionsmechanismen liefern.

Contents

1	Physics Case and Motivation	1
1.1	Meson Production in Nucleon-Nucleon Collisions	1
1.2	Spectator Model	5
1.2.1	Test of the Model	6
1.2.2	Experimental Applications	6
1.3	Measurement of the $pn \rightarrow d\omega$ Reaction	8
2	Experimental Set-Up	9
2.1	The ANKE Spectrometer at COSY-Jülich	9
2.2	Silicon Telescope	11
2.3	Forward Detection System	13
2.4	Trigger and Data Acquisition	15
2.5	Data Taking in August 2001	16
3	Spectator Proton Detection	19
3.1	Energy Calibration	19
3.2	Hit Selection	21
3.3	Particle Identification and Energy Determination	21
3.4	Tracking	23
4	Fast Deuteron Detection	25
4.1	Tracking and Momentum Reconstruction	25
4.1.1	Cluster Analysis	26
4.1.2	Track Reconstruction	27
4.2	Identification of Fast Deuterons	29
4.2.1	Čerenkov Proton Suppression	29
4.2.2	Energy Loss in the Hodoscope	31
5	Efficiency Determination	35
5.1	Trigger and Data Acquisition	35
5.2	Detection in the Silicon Telescope	37
5.3	Tracking in the Forward System	39
5.3.1	Method of Efficiency Determination	39
5.3.2	Global Plane Efficiency	41
5.3.3	Spatial Distributions	42
5.3.4	Chosen Procedure	44
5.3.5	Cross-Checks of the Method	44
5.4	Fast Deuteron Identification	47

5.5	Overall Result for the $pd \rightarrow p_{\text{sp}}d\omega$ Reaction	50
6	Luminosity Determination	53
6.1	Normalisation Concept	53
6.2	Selection of pd Elastic Scattering	54
6.3	pd Elastic Cross Section	55
6.4	Acceptance Determination	57
6.4.1	Target Geometry	57
6.4.2	Transverse Slice of the Target	59
6.4.3	Fraction Observed Along the Beam	60
6.5	Luminosity in August 2001	62
6.6	Cross-Check by Other Methods	64
6.7	Luminosity in the pn System	64
7	Experimental Results	67
7.1	Acceptance Determination	67
7.2	Missing-Mass Distributions	70
7.3	Background Parametrisation	73
7.4	Cross Section for $pn \rightarrow d\omega$	75
7.5	Systematic Uncertainties	76
7.6	Results and Comparison with Predictions	77
8	Outlook	81
8.1	Ongoing $pn \rightarrow d\omega$ Measurements	81
8.2	Further ω Production Channels	83
8.3	Test of the OZI Rule	83
A	Mathematical Considerations	85
A.1	Observables in Spectator Kinematics	85
A.2	Elastic Kinematics	86
A.3	Error Propagation	87
A.4	Ratio of Isospin Channels	88
B	Silicon Telescope	89
B.1	Geometry and Angular Reconstruction	89
B.2	Silicon Detectors	90
B.2.1	Surface Barrier Detectors	90
B.2.2	Silicon Strip Detectors	91
B.3	Signal Processing	94
B.3.1	Shaping and Dynamic Range	94
B.3.2	Resistor-Chain Read-Out	94
B.3.3	Set-up at ANKE	95
C	Figures and Tables	97

Chapter 1

Physics Case and Motivation

The use of hadronic probes to study meson production reactions and their theoretical interpretations are briefly reviewed. In the case of η production, a strong enhancement of the pn -channels is observed compared to the pp -channels. Most theoretical models also predict such a behaviour for the ω -production. However, up to now, the only channel, where data are present for ω -production is $pp \rightarrow pp\omega$. The possibility of using deuterium as an effective neutron target to study the $pn \rightarrow d\omega$ reaction at ANKE is introduced. It is shown that the spectator model is well understood within our experimental requirements. Furthermore, the method to tag pn -reactions by detecting slow spectator protons is described. The goal of the presented experiment is to extend the data to the isospin-zero channel by measuring the $pn \rightarrow d\omega$ reaction in quasi-free kinematics.

1.1 Meson Production in Nucleon-Nucleon Collisions

The existence of the nucleon substructure in terms of quarks and gluons has been first established using electromagnetic probes. Nevertheless, deep inelastic scattering with hadronic probes presents a complementary approach, due to the interaction via the strong force. In Quantum Chromo Dynamics (QCD) the interaction of coloured quarks is described via the exchange of massless gluons. Apart from the fact that the gluons carry colour charge, this is in direct analogy to the coupling of charged leptons via photons in the electromagnetic interaction described in the theory of Quantum Electro Dynamics (QED). However, there is a major difference for coloured objects, namely the confinement. In contrast to the small electromagnetic coupling constant $\alpha \approx 1/137$ which varies only weakly with energy¹, the coupling constant of the strong interaction α_s is about 0.1 at high energies and even approaches 1 at lower energies. Thus, especially at medium energies, which is the region of the experiments discussed in this

¹A variation with time is disputed currently due to some cosmological arguments [1].

document, the summation over higher order diagrams in perturbative models will not converge.

Despite the underlying QCD basis, over larger ranges (on the order of fermis), only colourless objects can be exchanged. Nuclear forces at medium energies are quantitatively described by these quark-antiquark pairs – the mesons – as virtual particles with a finite mass. In this picture, originally proposed in 1935 by Yukawa, the range of the strong interaction naturally comes in through the uncertainty principle $\Delta E \Delta s \geq \hbar c/2 \approx 100 \text{ MeV fm}$, where $\Delta s = \Delta t/c$. The mass of the lightest meson, the pion, was thus predicted to be about $100 \text{ MeV}/c^2$ from the range of the nucleon-nucleon force alone. Only in 1947, was the pion observed, with a mass of about 140 MeV , and the nuclear forces were attributed to it. Meson exchange is also the basis of the model calculations, which are performed to describe reactions in “medium energy physics” such as the η and ω -production reactions at threshold.

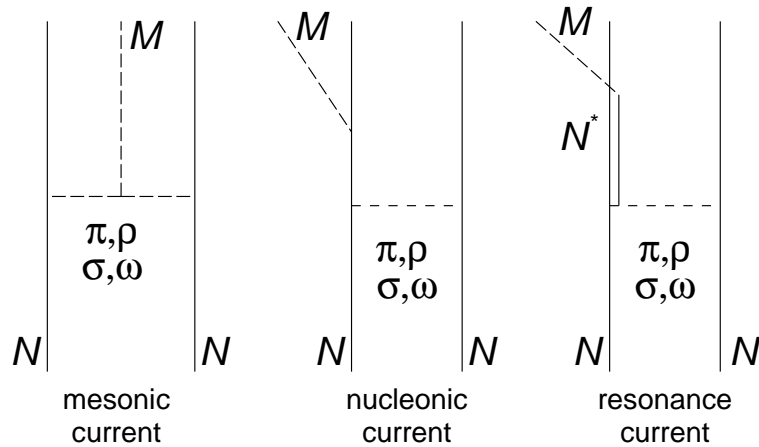


Figure 1.1: A few graphs illustrating meson production in NN collisions by the exchange of isovector or isoscalar mesons. Initial and final state interactions are not shown. Note that depending on the meson M in the final state or the intermediate resonance N^* , selection rules restrict the meson types to be exchanged in the mesonic or resonance currents respectively.

In Fig. 1.1 several graphs illustrate how a meson is believed to be produced in NN collisions via meson exchange. Shown are examples for mesonic and nucleonic currents, where the final state meson is produced either in a vertex with the exchange mesons or in the latter case via a nucleonic state. In the rightmost sketch the final state meson is produced via a baryonic resonance. For example the $N(1535) S_{11}$ is believed to dominate for η production e.g. in Refs. [2, 3], whereas in the $pp \rightarrow pp\omega$ reaction e.g. the $N(1710) P_{11}$ together with the $N(1700) D_{13}$ are assumed to play significant roles in Ref. [4, 5]. It will be shown later, that the assumption of either pure isovector or isoscalar meson exchange, like π, ρ or σ, ω respectively², alters the results significantly,

²The σ is a $I = 0$ resonance, which is either attributed to $\pi\pi$ or f_0 states, or could be due to uncorrelated two pion exchange.

and thus gives a handle on the production mechanisms. Experimentally this can be observed in the ratio of the pn to pp cross sections.

A general goal of the model calculations is to determine the coupling constants for the vertices in such graphs. Especially pion induced reactions and photon induced reactions (assuming vector dominance) are used to fix MN and MM coupling constants. This knowledge can be used to compute the total strength in NN collisions summing over all contributing graphs. However, the interference of several exchange channels has to be taken into account. Furthermore, initial (ISI) and final state interactions (FSI) play significant roles in many model calculations³. Thus data from several reaction channels are necessary to constrain the models. Especially the simultaneous knowledge of different isospin channels in meson production are an essential input. In the following an example illustrates how quantitative predictions can be made for the ratio of experimental cross section, if simplifying assumptions are made.

The relation between different charge channels can be fixed by isospin factors, if the exchange currents, the interferences, the ISI, and the FSI are assumed to be identical for both channels. Consider the production of an isoscalar meson M like the η or ω in pp and pn collisions and the ratio of their cross sections. The reactions $pp \rightarrow ppM$ and $pn \rightarrow dM$ are pure isospin channels with $I = 1$ and $I = 0$ respectively, whereas the reaction $pn \rightarrow pnM$ is a mixture of both. Isospin considerations alone imply that the ratio of $\sigma_{I=0}$ to $\sigma_{I=1}$ is 9 or 1 for pure isovector or isoscalar exchange respectively⁴. However, this can not be directly identified with the ratio $R_{d/pp} := \sigma_{\text{tot}}(pn \rightarrow dM) / \sigma_{\text{tot}}(pp \rightarrow ppM)$ as the first is a two-body final state including d formation, whereas the latter three-body final state is convoluted with pp FSI. It is straightforward, though, to compute the ratio

$$R_{pn/pp} := \frac{\sigma_{\text{tot}}(pn \rightarrow pnM)}{\sigma_{\text{tot}}(pp \rightarrow ppM)} = \begin{cases} 5 & \text{for isovector exchange, e.g. } \pi, \rho \\ 1 & \text{for isoscalar exchange, e.g. } \sigma, \omega \end{cases} \quad (1.1)$$

using $(\sigma_{I=0}/2 + \sigma_{I=1}/2)/\sigma_{I=1}$ being equal to $(\frac{9}{2} + \frac{1}{2})$ or $(\frac{1}{2} + \frac{1}{2})$ respectively. As soon as this ratio is fixed, it is claimed that it is possible to extract as well the ratio $R_{d/pp}$ in a rather model-independent way, by computing phase-space and isospin and using the relation between bound and scattering state wave functions [8].

Let us compare now these considerations with the available experimental data. For η -production experimental total cross sections in all isospin configurations are available, as shown in Fig. 1.2. Note, that the experimental techniques to explore the pn -reactions in quasi free kinematics and its validity will be described in the following section. The data from PINOT and SPESIII at SATURNE [10, 11], WASA at CELSIUS [12–15] and COSY11 [16] cover excess energies Q down to a few MeV. Moreover, there are results expected from COSY11 [17] filling the gap at $Q \leq 20$ MeV for $pn \rightarrow pn\eta$. The excess energy $Q = \sqrt{s} - \sum m_f$ is the energy available as kinetic energy in the final state of a

³There is a large variety of different approaches. An analytical approach keeping the transition matrix fixed is presented in Ref. [6] and microscopic calculations including FSI are shown e.g. in Refs. [7, 8]. In the latter case the coupling of the NN FSI to the production operator is vigorously discussed [9].

⁴In this case any differences in ISI and FSI are neglected. In App. A.4 the values are derived from the transition amplitudes.

reaction. It can be defined as the centre-of-mass energy \sqrt{s} minus the sum of the masses of the particles in the final state m_f .

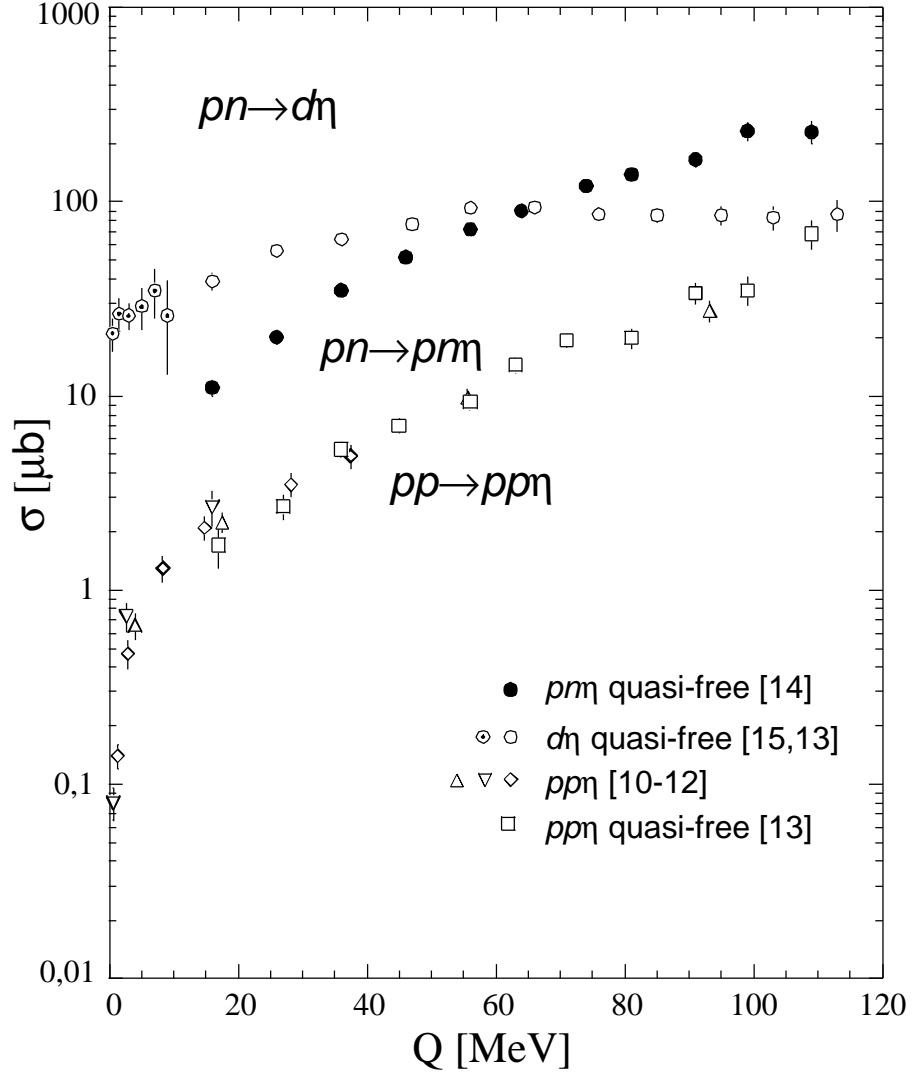


Figure 1.2: A compilation of experimentally obtained total cross sections for η -production [18]

From Fig. 1.2 the ratio $R_{pn/pp}$ is deduced to be 6.5 in the η -case over a wide range of excess energies, exceeding even the value of 5 from the naïve estimation for isovector exchange. Nevertheless, most of the effect is generally attributed to the dominance of isovector exchange. The data on $pn \rightarrow d\eta$ [13] show an enhancement compared to the pn -final state at low excess energies. This is generally attributed to the two-body phase space and the reader is advised to consult Refs. [2,3] for a survey of the field, as the details are clearly beyond the scope of the current discussion.

The reaction $\pi^- p \rightarrow \omega N$, measured almost 30 years ago [19–21] was a challenge to theoreticians for a very long time. At present only one group managed to describe the energy dependence of these data [22,23]. Thus, the credibility of the experimental data is vigorously disputed in Refs. [24–26]. The theoretical explanation required a rather strong influence of a $P_{11}(1710)$ as well as $D_{13}(1950)$ already rather close to the production threshold. As most models assume pion exchange to play the dominant role in the production amplitude [27], one should expect both resonances to have significant influence also on the $pn \rightarrow d\omega$ cross section. This would imply the population of higher ω partial waves already at rather low excess energy. Another question of high theoretical interest is the ωN scattering length. A possibility to get a handle on the real part would be through a study of the energy dependence of the reaction $pn \rightarrow d\omega$ for low excess energies. In the η case an enhancement of the cross section was observed [15] at excess energies below 10 MeV, which can be related to the ηd scattering length [28]. Both questions will not be solved within this work but are to be addressed experimentally in the upcoming experiments at ANKE.

1.2 Spectator Model

The deuteron is a remarkable nucleus, because of its small binding energy ≈ 2 MeV. Though the wave function of the two nucleons is about 95% in a relative s-wave, the deuteron diameter is about 4 fm [29]. This is in the very tail of the nuclear force. At such distances most of the reactions on this nucleus take place on one of the nucleons, whereas the other remains largely undisturbed. Taking only energy and momentum conservation into account, certain conclusions can already be drawn. If the target nucleus is at rest, the nucleon which takes part in the reaction must carry the inverse momentum of the residual “spectator” nucleon. Moreover, as this recoil nucleon can be observed, it must be real and thus the struck nucleon is off its mass shell. It will be shown in the following that at energies high enough to probe the constituent nucleons of the deuteron, these simple kinematical considerations in fact are sufficient to describe experimental data.

The pn cross section in the deuteron is generally less than that in free pn collisions due to the shadow effect [30]. Consider a geometrical arrangement where the neutron inside the deuteron is hidden from the incident beam particles by the proton. This situation would appear statistically and change the effective luminosity for the the reaction on the neutron. It is estimated to decrease the value by about 5% in the deuteron [31].

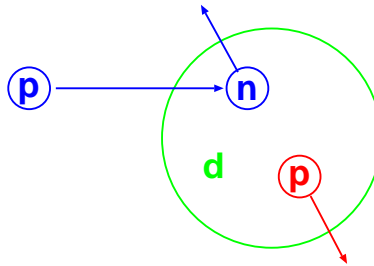


Figure 1.3: Naïve sketch of a deuteron and an impinging proton in the Spectator Model

1.2.1 Test of the Model

Even though the picture presented seems simplistic, several experiments have shown that it can describe the situation at COSY energies quite well. In the reaction $pd \rightarrow ppp\pi^-$ at TRIUMF [32] the spectator proton has been reconstructed by fixing a pp -pair in a 1S_0 state together with a pion. From the tagged reaction $pn \rightarrow pp(^1S_0)\pi^-$ the momentum of the spectator proton was reconstructed as shown in Fig. 1.4(a). For comparison, results from Monte Carlo simulations assuming the spectator model (solid line) and four body phase space (dashed line) are added in Fig. 1.4(a). Another approach has been performed at WASA/CELSIUS. η -production in $pp \rightarrow pp\eta$ has been measured both on a hydrogen target and quasi free on a deuterium target [14] (see Fig. 1.4(b)).

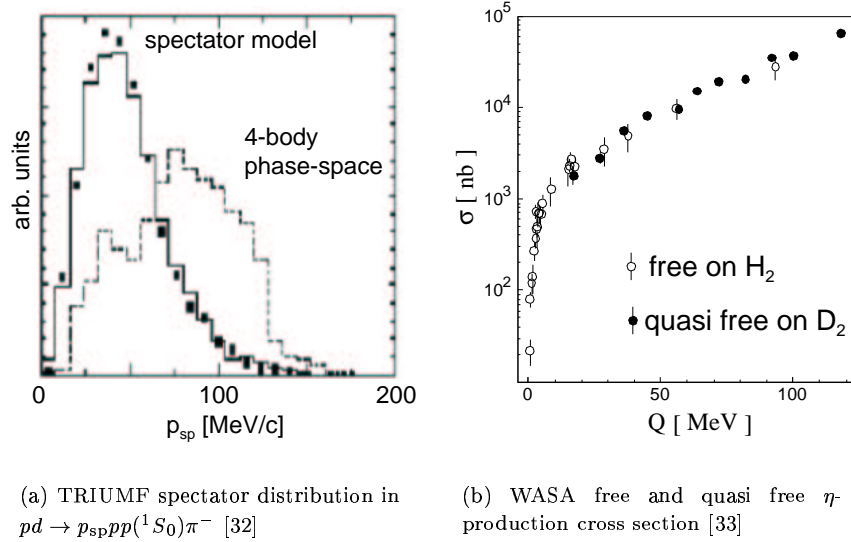


Figure 1.4: Two results showing the agreement of the spectator model predictions with experimental results

Both results show a striking agreement with the naïve model predictions. The correspondence of the model to the experimental distribution up to spectator momenta of about 150 MeV/c is observed in Fig. 1.4(a). In the case of $pn \rightarrow d\omega$ it is generally assumed that the model holds for spectator momenta up to about 200 MeV/c [34, 35]. This value is of course strongly dependent on any assumption on the final state interactions involved. Furthermore, Fig. 1.4(b) illustrates for the $pp \rightarrow pp\eta$ channel that the observable aimed at, namely the total cross section, is largely independent whether free or quasi free kinematics are studied.

1.2.2 Experimental Applications

As neutrons are unstable particles, one approach is to perform experiments with neutrons from heavy nuclei, like ^7Li [36,37]. However, it is difficult to disentangle

the various contributions in such large nuclei. Neutrons from reactors are limited in momentum and the tail to lower momenta prevents any precise determination of reaction kinematics. Even for stripped deuteron beams [38] the intrinsic momentum spread is typically about 7% FWHM. Studies on the weakly bound neutron inside the deuteron hence present an attractive alternative approach.

The results discussed in the last section showed the feasibility of the approach assuming quasi-free kinematics. The Fermi motion of the nucleons of course imposes a smearing of the experimental observables. On the other hand, in the experiment this can even be used to scan a range of excess energies with a single beam setting, if the resolution of the apparatus allows a kinematical reconstruction of the momentum of the quasi-free nucleon. Two different approaches to study pn -reactions in quasi-free kinematics are currently being employed:

Tagging by Kinematical Constraints has e.g. been used to obtain the already mentioned η -production cross sections measured at WASA in $pn \rightarrow d\eta$ [13] and $pn \rightarrow pn\eta$ [14] (see Fig. 1.2). In order to identify the reaction channel one has to determine all pn -reaction products. Alternatively, as was done in the latter case, the kinematical variables must be determined to such a level that the separation can be obtained using kinematical considerations on a statistical basis. Nevertheless, the Fermi motion of the nucleons imposes a smearing of the centre of mass energy \sqrt{s} in the pn system, which results in an uncertainty in the excess energy Q for the production.

Neutron Tagging by Spectator Detection is a technique, where the kinematical variables of the pn -entrance channel can be determined directly.⁵ Thus not only \sqrt{s} is fixed but also the transverse momentum and off-shellness of the neutron is, apart from rescattering⁶, fully determined by the measurement of the spectator proton. The excess energy of a reaction channel can then be calculated up to the intrinsic width of the produced particle. See App. A for a more detailed discussion of the kinematics. Experimentally two approaches are feasible and are being explored:

- **Deuteron beams** were used already in the 70s in bubble chamber experiments [39]. Such a beam, in conjunction with a liquid hydrogen target, is proposed for studying the $np \rightarrow pp\pi^-$ reaction at COSY-TOF [40]. Then the spectator protons are boosted with half the beam momentum and can be detected easily even with a rather thick target. However, only half of the beam momentum is transferred to the pn -reaction, imposing limits on the reactions possible at a given beam momentum. At COSY even η production is practically excluded with this technique. Furthermore, the kinematical observables of the fast spectator proton relative to its laboratory momentum have to be determined precisely. Additionally these protons are emitted at angles very close to 0° .
- Another technique, introduced for the first time at PROMICE/WASA in the reaction $pn \rightarrow d\pi^0$, is the detection of slow spectator protons from

⁵In general, the detection of a slow proton alone does not uniquely identify the reaction to having taken place on the neutron, but almost any additional information helps to eliminate quasi free reactions on the proton or coherent interactions with the deuteron.

⁶Experimental results shown before prove this effect to be small at $p_{sp} \leq 200$ MeV/c.

a **deuterium target** with silicon detectors and proton beam [41]. The same method is being applied to study $pn \rightarrow dM$ with $M = \omega, \eta, \pi^0$ at ANKE [42,43] and for $pn \rightarrow pn\eta$ at COSY11 [17]. Furthermore, studies on η' -production at COSY11 [44] and the mesons $\phi, a_0^0/f_0$ [45,46] at ANKE are planned. However, the requirements for spectator tagging are the use of a thin windowless target and the precise measurement of the slow spectator protons, which is by no means trivial.

1.3 Measurement of the $pn \rightarrow d\omega$ Reaction

The latter technique is the one applied to study the reaction $pn \rightarrow d\omega$ at ANKE. In order to do that the slow “spectator” proton (p_{sp}) from the $pd \rightarrow p_{\text{sp}}d\omega$ reaction was detected with $70 \leq p \leq 200$ MeV/c in a telescope of three silicon detectors close to the target. The coincident detection of the fast deuteron in the ANKE forward system enables us to identify the reaction via the missing mass technique. The spectator model is used to perform the transition into the neutron system, which is moving with respect to the laboratory system. Due to the acceptance of the silicon telescope, the kinematics is restricted to a certain range and hence a range in excess energy Q is defined. It is the goal of this work to extract cross sections for certain Q ranges. In order to do the normalisation, the luminosity is determined simultaneously with the same set-up using elastic $pd \rightarrow pd$ scattering.

As in the η case, measurements of the isospin channels of a certain reaction shed light on the production mechanisms in NN collisions and thus severely constrain any model calculation. In the case of ω production only data for $pp \rightarrow pp\omega$ have been published by SPESIII [47] and COSY-TOF [48]. The other channels were expected to be enhanced in cross section compared to the existing pp -data in a similar manner to the η -production. Thus, the experiment on $pn \rightarrow d\omega$ was considered as an “ideal early experiment for the ANKE facility” [49].

The results of the week of beam time in August 2001 have shown that these estimates were in fact far too optimistic. In this thesis a detailed discussion of the work done for the identification of the reaction and the analysis of the data is presented. Previously unknown cross sections on the ω -production in $pn \rightarrow d\omega$ have been extracted at two excess energy ranges and lie well below all current theoretical predictions. In the outlook, the goal to improve these data already within 2003 will be discussed. Furthermore, other complementary experiments will be outlined.

Chapter 2

Experimental Set-Up

The experiment has been performed at the magnetic spectrometer ANKE at the COoler SYnchrotron COSY-Jülich. The detection systems used to study ω production in pn reactions are the silicon telescope and the ANKE forward system. The telescope of three silicon detectors covers angles around 90° and serves two purposes: firstly to tag reactions on the neutron by the detection of slow spectator protons and secondly to perform an absolute luminosity determination. With the ANKE Forward Detection System the tracking and momentum reconstruction of fast ejectiles emitted at angles close to 0° is performed. Moreover the separation of deuterons from a 100 times higher proton background is, in particular, feasible due to the installation of inclined Čerenkov counters.

In this chapter, the technical aspects of the detectors are discussed, concluding with a description of the data acquisition and an overview of the experiment performed in August 2001. The actual method to identify and measure a spectator proton and a fast deuteron in ω -production reactions is described in the subsequent Chapters 3 and 4 respectively.

2.1 The ANKE Spectrometer at COSY-Jülich

The **Cooler Synchrotron COSY** (see Fig. 2.1) at the Research-Centre Jülich [50] provides stochastically and electron-cooled proton and deuteron beams in a momentum range from 300 MeV/c up to 3.65 GeV/c. The circulating beam can be used for internal experiments (EDDA, COSY11, ANKE and PISA), with thin gas or foil targets, or extracted to external experiments (TOF, MOMO/GEM at BIG KARL, NESSI & JESSICA). Furthermore, polarised proton beams have been provided for internal as well as external experiments.

The **Apparatus for Nuclear and Kaon Ejectiles ANKE** [51] is a magnetic spectrometer placed at an internal target position of the storage ring COSY. The overlap with the COSY beam is used for experiments on thin solid targets or a jet target providing hydrogen or deuterium clusters with densities of about 10^{14} atoms/cm² in an overlap region of about 1 cm³. An order of magnitude higher luminosity is expected from a target in preparation yielding frozen pellets with typical diameters of 50 μ m [52]. Furthermore a polarised gas target, together with a storage cell of 40 cm length, will yield a similar beam target overlap as the cluster target with densities of about 10^{13} atoms/cm² [53]. After the

commissioning of this set-up, double polarisation measurements will be feasible at COSY. For this purpose a completely redesigned target chamber has already been installed. This will also allow us to improve significantly the upcoming studies on ω -production in 2003, due to additional space for the placement of silicon counters.

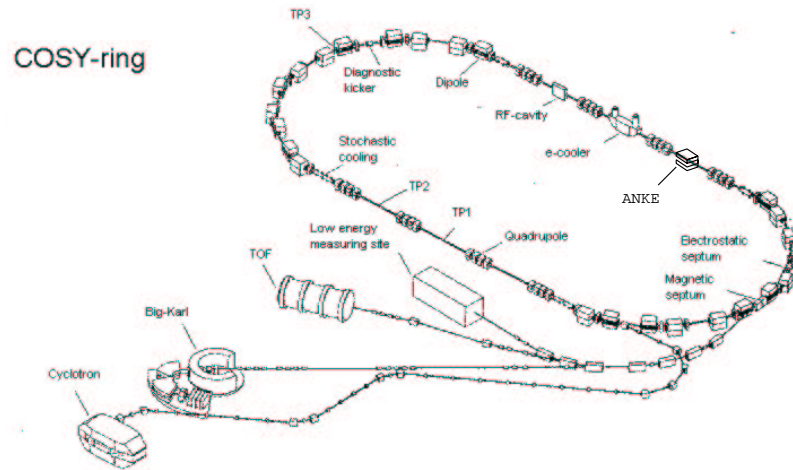


Figure 2.1: The Cooler Synchrotron COSY at the Forschungszentrum Jülich

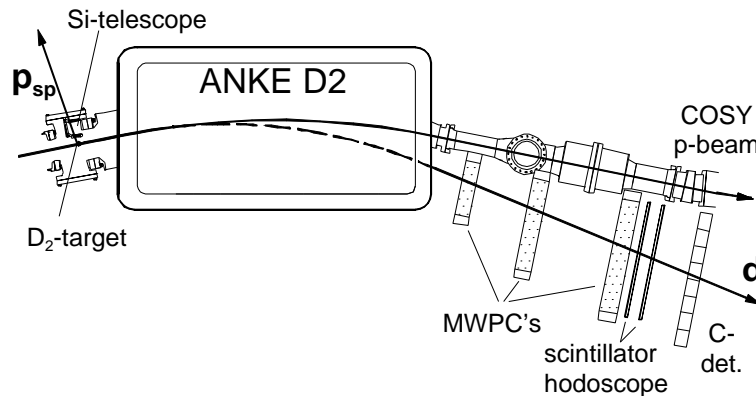


Figure 2.2: Part of the ANKE set-up used for ω -measurements: sketched are the circulating COSY beam, the target chamber with the telescope for spectator proton detection, the spectrometer dipole D2 and the forward detection system used to track and identify fast deuterons.

The spectrometer is designed as a zero degree facility to study meson production close to threshold. Charged ejectiles emitted at small forward angles

can be traced through the magnetic field of the main spectrometer magnet D2 by the detection in one of the various sensitive elements of ANKE. The reader is advised to consult Ref. [51] for an overview. The following description will be limited to the components used for this specific analysis, namely the forward detection system and the silicon telescope close to the target (see Fig. 2.2).

2.2 Silicon Telescope

As discussed before, it is necessary to detect protons of a few MeV kinetic energy to study the $pn \rightarrow dM$ reactions. The set-up presented in this section provides all the information needed and serves as a tool to determine simultaneously the luminosity. Here, only the set-up will be described; the experimental results will be discussed in Chap. 3 and 6.

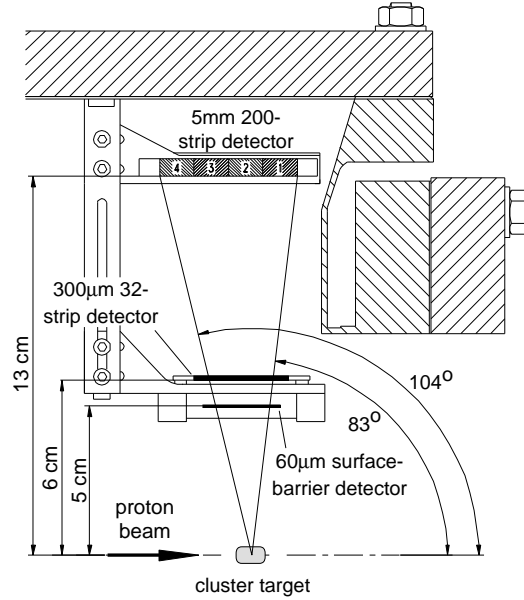


Figure 2.3: Silicon telescope in the ANKE target chamber: shown is the COSY beam, the cluster target and the telescope structure consisting of three silicon detectors. A kinetic energy range for protons of 2.5–30 MeV is covered providing identification and full momentum reconstruction.

To achieve tracking, energy determination and particle identification within the boundary conditions of restricted space inside the vacuum chamber of ANKE, a telescope structure of three layers of silicon detectors has been chosen. For particle identification via the $\Delta E/E$ -method, the particle has to be stopped after traversing a preceding detector and depositing part of its energy in it. (See Chap. 3 for a detailed discussion.) A 5 mm thick lithium-drifted strip detector [54] stops protons with up to 30 MeV kinetic energy ($p_p = 250$ MeV/c). In combination with a 300 μm thick detector, protons with $T_p \geq 6$ MeV can be identified. In order to extend this range down to kinetic energies of 2 MeV – note, that the Fermi distribution of the deuteron reaches its maximum value

at $T \approx 1 \text{ MeV}$ ($p \approx 50 \text{ MeV}/c$) – a $60 \mu\text{m}$ thick surface barrier detector was chosen as the first layer. The choice combines small stopping power, thus a low threshold for protons, with energy deposits sufficient to distinguish protons from deuterons in view of the resolution decreasing with thickness¹. A $18 \mu\text{m}$ thick detector has been tested, but was not used due to its resolution of 130 keV FWHM comparable to the band separation of 150 keV [55].

The set-up shown in a top view in Fig. 2.3 has been positioned such, that in the horizontal plane, angles from 83° to 104° are covered (See Fig. B.1 in App. B.1 for precise dimensions). In the vertical direction $\pm 10^\circ$ and $\pm 7^\circ$ are covered for the second and third layers respectively. We will see in Chap. 6, that the coverage of the forward angles allows us to determine the luminosity simultaneously to the ω -measurement. However, to determine the kinematics of the neutron, and thus the excess energy in the pn -reaction, not only the energy of the recoil proton is required but also its polar angle. We will see in Chap. 7 that the missing mass determination is much more sensitive to a variation in the polar angle than in the energy of the recoil proton. The second and third layers are composed of strips arranged perpendicular to the beam such that an angular resolution of 0.4° can be obtained in the horizontal plane neglecting angular straggling². For particles stopped in the second layer, neglecting a small background not originating at the target, the finite target size leads to a determination of this angle within $\pm 5^\circ$.

The first generation telescope, in use initially in September 1999, has since seen only two small modifications. The first detector, originally only $18 \mu\text{m}$ thick, was replaced by a larger $60 \mu\text{m}$ thick surface barrier detector. Secondly two weak α -sources (50 and 500 Bq) were mounted in order to monitor continuously the calibration of the $300 \mu\text{m}$ and the 5 mm thick detectors. The count rates are chosen such, that within two hours (typical time for a run) for each read-out channel, more than 300 events are collected yielding clean peaks on the experimental distributions.

	1 st layer	2 nd layer	3 rd layer
sensitive thickness	$60.9 \mu\text{m}$	$300 \mu\text{m}$	5.1 mm
active area	450 mm^2	$32 \times 15 \text{ mm}^2$	$46.8 \times 23 \text{ mm}^2$
segmentation	none	32	4×50
pitch	—	1 mm	$235 \mu\text{m}$

Table 2.1: Basic properties of the detectors used in the ANKE experiment in August 2001: the first layer is circular and not segmented whereas, for the other layers, the number of strips and their width – the so called “pitch” – is given.

The basic features of the detectors used are listed in Table 2.1 and a more detailed description can be found in Appendix B.2. The surface barrier detector and all 32 strips of the $300 \mu\text{m}$ detector are read out individually. The 5 mm thick detector is read out in four divisions of 50 strips connected by a resistor chain. Please refer to App. B.3 for more details on the read-out.

¹Oscillations and noise increase with capacitance, being itself proportional to the area of the detector and inversely proportional to its thickness.

²The contribution from angular straggling will be discussed in Chap. 3

2.3 Forward Detection System

The forward detection system [56, 57] consists of three multi-wire proportional chambers (MWPCs) for tracking, a scintillator hodoscope with two planes, and inclined Čerenkov Counters for particle identification. The subsequent arrangement behind the forward exit window of the main spectrometer magnet D2 allows one to detect nearly all the charged particles exiting through this window. In the following the components and their operation are described, whereas all the data analysis is described in Chap. 4 on page 25 *et seq.*

Multi-Wire Proportional Chambers (MWPCs)

Each of the three wire chambers [58] comprises two sensitive planes, which are rotated by 90° with respect to each other, but are identical in design. Each plane consists of 300 to 400 signal wires of $30\ \mu\text{m}$ thickness with 1 mm spacing and a gap of 1.5 mm to the cathode plane. A dielectric foil of $100\ \mu\text{m}$ on the opposite side separates wires from cathode strips. These strips, which are also read out by the data acquisition, have a pitch of 3.5 mm and are inclined by 18° with respect to the wires. The basic principle is sketched in Fig. 2.4 and a detailed description can be found in Ref. [56].

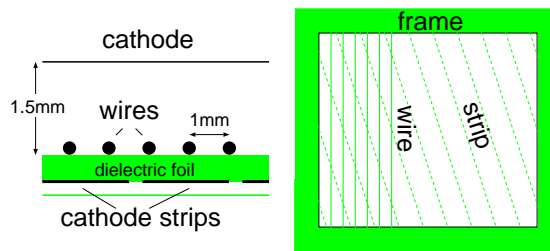


Figure 2.4: Sketch of the arrangement in one sensitive plane of the MWPCs. Shown is a cut through a plane and a schematic top view of the by 18° inclined arrangement of anode wires and cathode strips.

The analysis of the so called X (vertical wires providing the X-coordinate) and Y-plane (horizontal wires) enables the reconstruction of a point in space with a resolution of approximately 1 mm on a single event basis. Moreover the additional information from the inclined strips provides another less sensitive criterion to determine the coordinate. This is applied for efficiency determination in Sec. 5.3. In this case a track is formed with the information of three sensitive planes only. The actual cluster analysis leading to a full track reconstruction is discussed in Sec. 4.1.

Scintillator Hodoscope

Two sets of 8 and 9 vertical scintillators are arranged in two layers respectively. Their width decreases from 80 to 40 mm to account for the increase in count rates close to the beam pipe. The timing and amplitude signals are read out via photomultipliers placed on both ends of each scintillator; and a hardware mean timer is used to form the trigger for the data acquisition [59]. The obtained

individual amplitudes have been calibrated to provide the energy loss per centimetre and this information can be used for particle identification, as described in Sec. 4.2.2.

Inclined Čerenkov Counters

The deuterons from $pn \rightarrow d\omega$ with momenta around 2 GeV/c are accompanied by a two-orders-of-magnitude higher proton background in the same momentum range. In order to distinguish between these two types of particles, inclined Čerenkov counters [57] have been installed behind the hodoscope. They enable us to suppress the proton contribution such that an identification by the energy loss in the hodoscope counters becomes feasible. The light yield in the Čerenkov material is a function of the particle velocity β . Together with the reconstructed momentum in the magnetic field a criterion for identity of the particle can be obtained.³ Above 1.7 GeV/c, protons as well as deuterons produce Čerenkov light. Nevertheless the opening angle of the Čerenkov light cone is very sensitive to the velocity of the particle (see Fig. 2.5(b)). This fact can be exploited for particle identification using the counters as threshold detectors.

Consider the detector response to a proton and a deuteron with the same momentum, as illustrated in Fig. 2.5(a). Since the proton is faster, its Čerenkov light cone has a larger opening angle. The inclination angle of the panel can then be adjusted such that part of the light cone of the proton is totally reflected at its back surface and reaches finally the photomultiplier at the end of the counter. On the other hand all the light produced by the deuteron leaves the counter as the counters are wrapped in non-reflecting foil.

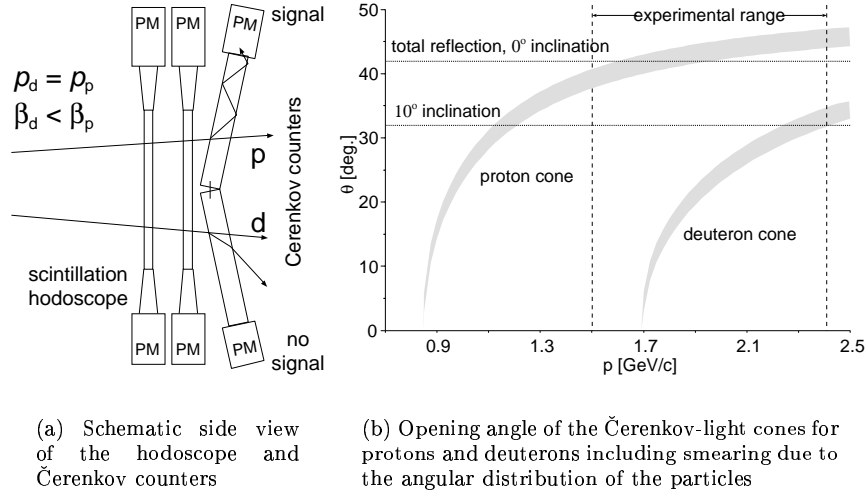


Figure 2.5: Side view of the forward set-up (partially), illustrating the detection principle of the Čerenkov counters and the opening angles of the light cones for protons and deuterons over the experimental momentum range of interest.

³The reconstruction is in principle sensitive only to the rigidity, but particles having more than one elementary charge are easily distinguished by their energy losses.

The adjustment for this angle between $+15^\circ$ to -5° , was obtained from Fig. 2.5(b) and cross-checked experimentally. Here the opening angle of the Čerenkov-light cones of protons and deuterons *versus* their momenta are plotted as bands. The width of the bands stems from the vertical angle distribution of the particles in the region of the counters ($0 - 3^\circ$). Furthermore, the experimental momentum range in which deuterons have to be identified and the total reflection angle with and without inclination are indicated. From these considerations and experimental studies an angle of -10° was chosen to achieve a high proton suppression without significant losses of deuterons. Though the deuteron cone already exceeds the total reflection angle in the high momentum range, no significant signal from these particles was observed. This can be understood qualitatively due to the amplitude dependence on the fraction of the cone reflected into the photo-multiplier.

2.4 Trigger and Data Acquisition

The main trigger for the experiment is a coincidence of the forward hodoscope and the second layer of the silicon telescope. In order to achieve this, an OR of the mean timer signals of all forward hodoscope counters has been prepared. Additionally, an OR of the 32 individually discriminated amplifier signals from the $300\ \mu\text{m}$ thick strip detector is used. The thresholds have been set at a level, that corresponds to below 300 keV energy deposit in this second layer of the telescope. In parallel the trigger from the silicon telescope alone has been used, pre-scaled by a factor of 999, such that the dead time of the data acquisition was not significantly increased. This trigger is useful for recording data with the online calibration sources of the set-up and as a cross check for the operation of the system, e.g. to check the trigger efficiency as discussed in Chap. 5.

	trigger	read out	mean rate [1/s]
1	telescope & forward	all detectors	2000
2	telescope/999	all detectors	15
3	parasitic tests	all detectors	10
4	10 Hz	scalers	10

Table 2.2: Trigger setting during the data taking for the beam time in August 2001: the coincidence of the telescope and forward T1 has been used as the main trigger.

In Table 2.2 the settings are summarised, showing also that for each trigger (except trigger #4) all sub-systems of ANKE have been read out. Clearly, this includes the full forward system and the silicon telescope. Moreover, the detection systems of the positive side and negative side have been included in the readout to have access to charged pion detection, efficiency determination and further cross-checks. Trigger number 4 is used to read out the scalers periodically (ten times per second). Furthermore typical rates obtained during the beam time are included.

By the use of single board PCs, connected via a synchronisation bus, one achieves read-out times of about $100\ \mu\text{s}$. This is due to the fact that the data are labelled event-by-event but transferred as separate clusters of one sub-system to

the central data acquisition and written to DLT tape. Only thereafter, dedicated software disentangles the sub-events and combines them to a full event [60]. For the online analysis, part of the events can be distributed to several streams in order to run several analysis programs simultaneously.

2.5 Data Taking in August 2001

The above described set-up has been used to study ω production during calendar week 33 (August 11th to 19th) in 2001. The machine development week before (week 32) had already been used to develop the beam for our purposes. Furthermore detectors and electronics were checked and adjusted during this phase. The nights of this machine week could be used to collect statistics with a hydrogen target and two beam momenta: 1.219 and 2.806 GeV/c. The data were taken with the trigger set as a coincidence of the two layers of the forward hodoscope and an additional signal from the fast trigger chamber. This allowed off-line alignment of the exact MWPC geometry, calibration of the hodoscope, and efficiency calibration of the inclined Čerenkov counters.

For the following production runs the cluster-jet target was operated with deuterium and four different proton beam momenta listed in Table 2.3 were used to gather statistics in the reaction $pd \rightarrow p_{\text{sp}}dX$ below and above the threshold for ω production. As we will see later, only the full set of data enables us to disentangle the ω signal from the large multi-pion background. The excess energy ranges (FWHM) for $pn \rightarrow d\omega$ production are shown for the two spectator energy ranges SP1: $2.6 \leq T_p \leq 4.4$ and SP2: $8 \leq T_p \leq 22$ MeV, which will be introduced in the next chapter.

The data taking was performed with 2 to 4×10^{10} protons in the COSY ring with typical luminosities of 5×10^{30} / (cm²s) (see Table C.1 on page 99 for a run by run listing). Coincidence trigger rates were on average about 2000/s, where the individual rates were about 60×10^3 /s for the forward hodoscope and about 15×10^3 /s for the silicon telescope (see Fig. C.1 on page 101 for the development over the beam time).

p_{beam} [GeV/c]	1.219	2.600	2.700	2.807	2.900
α_{ANKE} [°]	7.3	7.3	7.3	7.3	7.0
B_{max} [T]	0.6679	1.4454	1.5050	1.5701	1.5548
D2 position [mm]	255.5	255.5	255.5	255.5	247.0
Q^{SP1} [MeV]	—	-58 to -22	-23 to +13	+8 to +44	+42 to +78
Q^{SP2} [MeV]	—	-87 to -27	-55 to +5	-22 to +38	+13 to +73
\mathcal{L} [1/pb]		0.93	0.49	0.97	0.49

Table 2.3: Beam time in August 2001: Beam momenta p_{beam} , experimental settings, resulting excess energy range for $pn \rightarrow d\omega$ for the low Q^{SP1} and high energy spectator protons Q^{SP2} (see Chap. 3 on page 19) and the integrated luminosity \mathcal{L} recorded are shown.

In Table 2.3 several important features are listed for all beam momenta. ANKE was used in the so called “Kaon Mode”, where the main spectrometer magnet D2 is shifted by 24.6 mm to the outer side of the ring fixing simultane-

ously the target in its nominal position for a given deflection angle α_{ANKE} (see Ref. [51] for a closer description). Thus the forward detection systems get closer to the beam covering a larger acceptance for ejectiles emitted at small angles. The maximum magnetic field B_{max} in the D2-magnet is given. Integrated luminosities L of $\approx 1/\text{pb}$ and $\approx 0.5/\text{pb}$ were recorded for the two lower and upper beam momenta respectively.

Chapter 3

Spectator Proton Detection

The silicon telescope described in Sec. 2.2 is capable of detecting slow charged particles in three layers of silicon. The present aim is to identify protons and to determine their kinetic energy and azimuthal angle in an energy range from 2.5 to 30 MeV. Thus, within the spectator model, the proton-neutron reaction can be tagged and all the kinematical variables of the neutron in the initial state can be fixed. Consequently, the centre-of-mass energy is also defined event by event for the pn system.

Due to the requirement of particle identification, the natural subdivision is into two groups, namely particles stopped in the second layer and those which penetrated this layer and have been stopped in the last layer. The second subdivision is into protons and deuterons selected by the $\Delta E/E$ -method. For these events the polar angle at the target can be reconstructed using magnetic field corrections. For the particles stopped in the second layer one has to assume their origin to be at the centre of the beam-target overlap region, whereas for the ones stopped in the last layer the coordinate along the beam axis can be reconstructed.

3.1 Energy Calibration

For each readout channel the amplitudes were calibrated individually. In order to do this an α source was used in combination with an electronic pulser designed to deliver precise attenuation factors. Thus the exact input-to-amplitude dependence of the whole electronic chain can be determined in the laboratory. Taken together with the known energy deposit from the α particles, an absolute calibration is obtained in the laboratory. For example in Fig. 3.1(a) the amplitude spectrum(a) obtained with 5 different attenuation settings of the pulser (narrow peaks) and the α energy is shown. However, the amplitudes may well change for the measurement in the COSY-ring. As the system was found to be linear, within 1% accuracy, a first order polynomial was fitted and the pulser was calibrated in terms of energy loss. After the installation of the set-up inside the accelerator ring, the calibrated pulser¹ can be used at any time to perform an *in situ* calibration. Furthermore, two permanently mounted α -sources could be used to obtain an independent absolute calibration and hence to check the

¹Attenuations in the cables have been measured and were found to be negligible.

calibration. As an example, the upper and lower distributions in Fig. 3.1(b) show the energy loss in the second layer for particles emitted at forward and backward angles respectively. As the detector response was required for the trigger, the events from the mounted on-line α source were recorded together with particles from the target. Sharp α peaks reproducing the tabulated energy of 5.48 MeV within $\leq 1\%$ are visible on broad distributions from protons and deuterons. The upper edge of these distributions reflect the stopping power for protons and deuterons in this layer. Including energy straggling this corresponds to approximately 6 and 8 MeV, respectively.

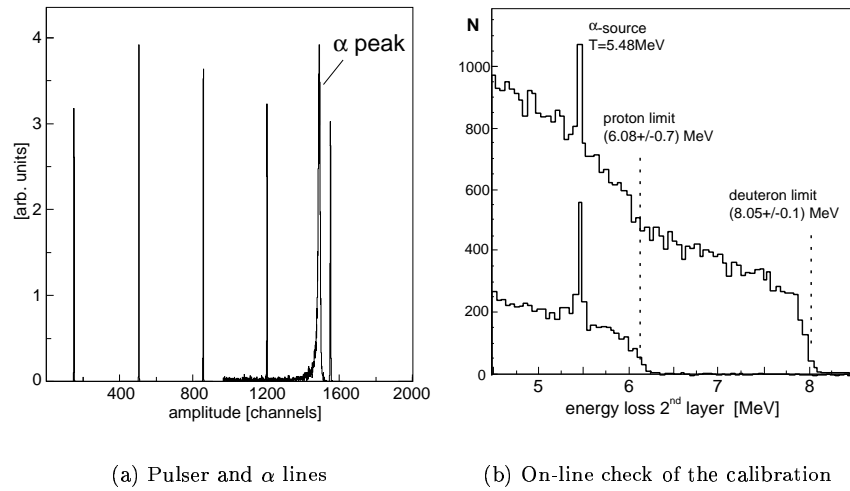


Figure 3.1: Calibration of the 300 μm thick second detector. The pulser signals and α peak position allow an absolute calibration (a), which can be checked by the permanently mounted α source (narrow peaks in (b)) and the stopping power for protons and deuterons in the upper and lower curve at respectively forward and backward angles.

3.2 Hit Selection

Given the segmentation in one coordinate only for the second and third layers, no multiple-track analysis can be performed in the set-up. Thus events with a signal in several segments of one detector had to be rejected. As a compromise between having a small fraction rejected and a low threshold in energy deposit, a software threshold was set in the segmented second and third layer detectors. Using the calibrated energy deposit a common threshold of 600 keV has been set for the 32 channels of the second layer. Nevertheless in 6% of the events, a signal has been obtained from more than one strip. These we call multiple hits. Possible reasons for this are charge splitting, the presence of several tracks through the detector, or noise. As the sources cannot be reliably distinguished, these events have been dropped from the later analysis. From the largely unchanged shape of distributions of single and multiple hits (see e.g. Fig. 3.2), one concludes that the loss in events can be overall corrected.

In the 5 mm-thick last detector, with its resistor-chain readout (see App. B.3.2), the hardware threshold was already high enough to reduce the amount of multiple hits to a level of about 1%. Therefore, after checking also here the distributions, no additional threshold was set. For both detectors the ratio of multiple to single hits has been recorded for each run to be used as a correction factor (see Sec. 5.2).

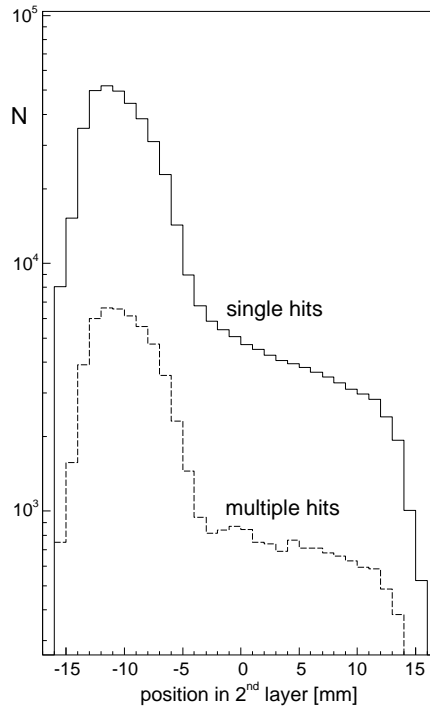


Figure 3.2: Spatial event distribution in the second layer of the silicon telescope for a single (solid) and several signals (dashed line) in the 2nd layer.

3.3 Particle Identification and Energy Determination

The energy range of the set-up is naturally divided into two subsets. Protons with kinetic energies between 2.3 and 6.7 MeV traverse the 60 μm thick surface barrier detector and are stopped in the second layer. However, protons penetrating the 300 μm detector and being stopped in the 5 mm thick last detector, cover energies up to 31 MeV (250 MeV/c). Nevertheless, the identification of protons by the $\Delta E/E$ -method is spoiled below that upper limit, because the band from deuterons traversing the corresponding detector overlaps the band from stopped protons (see overlap region of the particle bands in Fig. 3.3). Furthermore, the finite energy resolution does not allow a distinction from not-stopped protons even slightly above this limit.

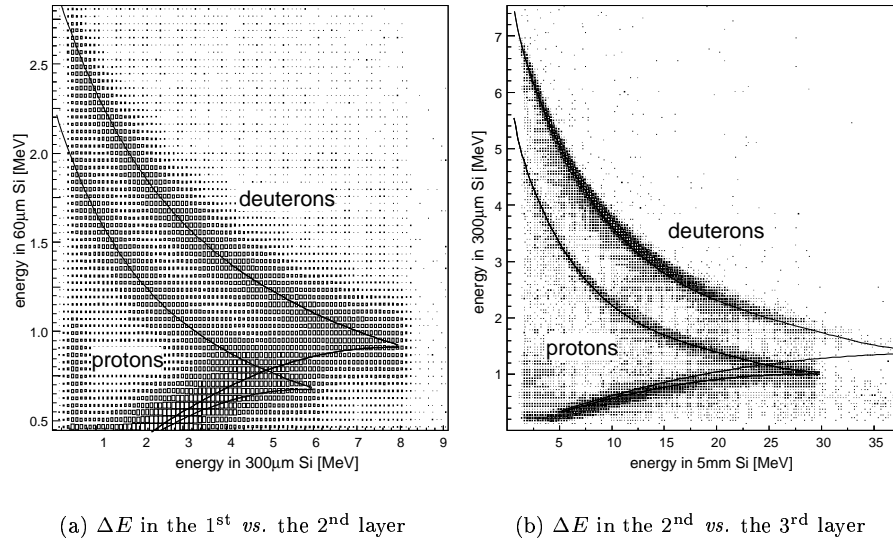


Figure 3.3: Particle identification by plotting energy deposits in two detectors of the telescope *versus* each other: Boxes correspond to experimental data. Lines are Monte-Carlo simulations [61] for energy losses of protons and deuterons in silicon.

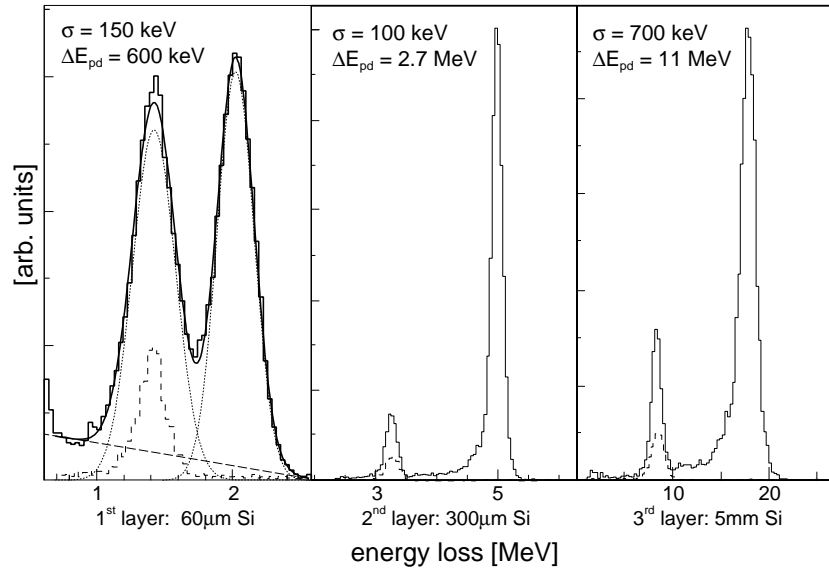


Figure 3.4: Slices of the $\Delta E/E$ spectra in Fig. 3.3 obtained by applying a narrow ΔE -cut in another layer show the separation of the proton and deuteron bands in the three layers (solid distributions). The dashed distributions are obtained after rejecting elastic events by the forward system. For the first layer a fit of two Gaussians (dotted) plus a straight line (dashed) is drawn as a solid curve.

The observed agreement of the simulations and experimental data in Fig. 3.3 can be described more quantitatively by comparing the experimental mean energy losses with simulations. Monte Carlo simulations [61] (curves in Fig. 3.3) and the experimental data coincide within 1%. Thus the systematic error of the absolute kinetic energy determination can be estimated to be below 1%.

A clear separation of protons and deuterons for the high energy range can already be observed in Fig. 3.3(b). For the lower momenta in Fig. 3.3(a), the separation is poorer, due to a combination of worse resolution and smaller energy losses in the $60\ \mu\text{m}$ thick first layer. Slices of the distributions for each layer are plotted in Fig. 3.4. Note that, using slices, the obtained resolution is worsened by the change of energy loss within the slices. Nevertheless, due to rather narrow cuts, this effect is small. For simplicity the peaks are approximated by Gaussian distributions. The experimental resolutions are deduced to be 150 keV, 100 keV and approximately 700 keV for the first, second and third layers, respectively. The distinction between protons and deuterons depends on the ratio of the band separation (0.6, 2.7 and 11 MeV respectively) to the resolution. A 2σ separation for protons and deuterons is deduced in the first layer. In the second and third layers the separation is well above 5σ . By the selection of inelastic particles in the forward detection system (see following Chap. 4) the deuteron contribution decreases dramatically, as indicated by the dashed distributions in Fig. 3.4.

3.4 Tracking

The $300\ \mu\text{m}$ and 5 mm thick detectors have strips perpendicular to the beam direction on one side, whereas the $60\ \mu\text{m}$ has no spatial resolution. Thus the angular resolution, neglecting angular straggling, is in principle about 0.4° in the horizontal plane, but this value can only be reached for very fast particles. For protons stopped in the set-up, straggling in fact dominates the resolution. For $T_p \geq 8\ \text{MeV}$ it is found to be between 1 and 3° . This value was obtained in a dedicated experiment using beam protons at the Tandem accelerator at the Institute of Nuclear Physics of the University of Cologne. In Fig. 3.5 the experimental results (points with error bars) and the calculation of small angle scattering (lines) are compared. Please refer to Ref. [55] for the details of the measurements and calculations.

For low energy protons ($T_p \leq 6\ \text{MeV}$) only a single position information is obtained, namely the strip number in the second layer. Thus the experimentally determined centre of the target was assumed as being the point of origin for these particles. Given the target length, the uncertainty in the angular determination is $\pm 5^\circ$ ². This results in a background contribution not originating from the target of the order of a few per cent. Similarly the vertical angle is determined only by target and detector sizes. Within the range of $\approx \pm 10^\circ$ the latter angle corresponds to the azimuthal angle acceptance, whereas the horizontal angle can be approximated well by the polar angle.

Magnetic field corrections have been introduced to compensate for the curvature of the particle tracks in the magnetic field. The field values in the target region where the telescope is situated are, with $B \lesssim 0.1\ \text{T}$, much smaller than the maximum values in the spectrometer $B = 1.6\ \text{T}$. Nevertheless, due to the low momenta (70 to 200 MeV/c) of the spectator protons detected, a significant

²In this case angular straggling is a minor contribution.

deflection had to be corrected for. A function relating the kinetic energy of the protons to an angular shift has been included (see App. B.1). The corrections from 0.6 to 1.8° from the straight line approach have been obtained using Monte Carlo simulations [62]. In Table 3.1 the two energy (i.e. momentum) ranges which have been selected to identify protons with the deduced angular resolution $\sigma(\theta)$ are shown.

combination	1 st & 2 nd	2 nd & 3 rd
T_p -range	2.6 – 4.4 MeV	8 – 22 MeV
p_p -range	70 – 91 MeV/c	123 – 204 MeV/c
$\sigma(\theta_{sp})$	$\approx 5^\circ$	$\leq 3^\circ$

Table 3.1: Ranges of detection and angular resolution in the silicon telescope

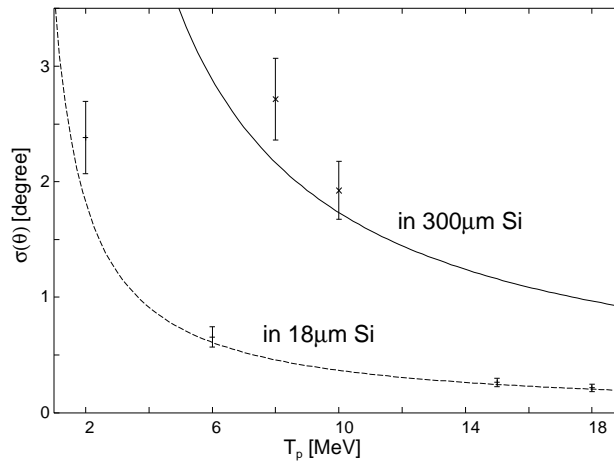


Figure 3.5: Angular straggling in $18 \mu\text{m}$ and $300 \mu\text{m}$ silicon measured at the Tandem accelerator in Cologne (points with error-bars) and multiple scattering calculations (solid and dashed lines respectively).

Chapter 4

Fast Deuteron Detection

In addition to the spectator protons, fast deuterons have also to be detected at forward scattering angles in order to identify the reaction $pd \rightarrow p_{sp}d\omega$. However, a huge number of charged particles are scattered through small angles into the acceptance of the forward detection system. With a deuterium target and a proton beam, most charged projectiles are elastically and quasi-free scattered protons. Furthermore, protons and pions from deuteron break-up reactions are strongly represented. The first goal of the analysis discussed here is to extract the deuteron contribution, which is two orders of magnitude smaller. Their momenta and angles at the interaction point have also to be determined.

The latter point is discussed first in this chapter, since the tracking is the basis for all further selections. A dedicated single cluster analysis has been chosen to obtain unambiguous information from the wire chambers. The tracking method implemented [63] allows us to suppress scattered background and to determine all the kinematic variables. Cross checks with known reaction kinematics and independently determined angles using coincident elastic deuterons in the silicon telescope show good agreement.

Subsequently the reconstructed tracks and momenta can be used for a dedicated analysis of the Čerenkov and hodoscope responses. As a result, deuterons in the momentum range from 1.5 GeV/c to 2.4 GeV/c can be identified on a single event basis with a residual background smaller than 10%.

4.1 Tracking and Momentum Reconstruction

A dedicated analysis using the whole information from the forward system to reconstruct tracks through ANKE has been developed by S. Dymov [63]. In this section the basic steps are sketched but the special selections applied for the data analysis from the beam time in August 2001 are described in detail. These considerations are made in view of electronic oscillations and an extremely low and inhomogeneous wire chamber efficiencies, whose determination is described in the following section.

4.1.1 Cluster Analysis

As described in Sec. 2.3, the two multi-wire proportional chambers (MWPCs), consisting of two sensitive wire planes each, provide information of responding wires and strips for each event. Due to resolution, the wire information alone is used for the data analysis. Thus a track is defined by two X and Y coordinates and is not over-constrained. In this case any additional signal from another particle or from oscillations leads to ambiguities. A procedure to obtain a selection of track candidates from up to 9 clusters per plane has been developed and used in deuteron break-up experiments at ANKE [64]. This so called “multiple cluster analysis” is indispensable for the analysis of multi-track events in reactions such as $pd \rightarrow ppn$ or $pp \rightarrow d\pi^+$. In our case, however, only events with a single track in the forward system were analysed. We could simplify thus the situation considerably by allowing only one cluster per plane. As we will see in the following, this reduces systematic effects considerably and the loss of statistics is below 20%.

Only events were considered in which a single cluster of only one or at most two wires width was obtained in each of the two X and two Y planes. This allows us to reconstruct a track without ambiguities and will be called “single-cluster analysis”. A drawback of this approach is, of course, the loss in statistics. Nevertheless only 10 to 20% of the data, which had been accepted using the multiple-cluster approach, had to be rejected¹. Moreover the following advantages of the single-cluster analysis in comparison to the analysis of all events have been found:

- The efficiency determination of the tracking relies on the assumption that it is the product of all individual plane efficiencies. As will be described in Sec. 5.3, the systematic uncertainty in the efficiency determination for the whole tracking method is strongly reduced by the single cluster selection.
- Experimental distributions of physical observables are smooth and correspond to their expected shape. For example the unphysical structures above the elastic peak in the momentum distribution vanish and the integral tail is suppressed by more than an order of magnitude (from originally 1.8% to 0.16% of the entries in the elastic peak, as shown in Fig. 4.1).
- The anticoincidence required with the signal from the Čerenkov counters is very likely to enhance the known 1 to 2% contribution of artefacts in the multiple-cluster analysis even further. This is due to the fact that any track reconstructed with a certain momentum inside the counter borders, but missing in reality the counter or being of lower momentum, is identified as a deuteron candidate. (Please refer to Sec. 4.2 for a description of the method.)²

¹The loss is about 10% and 20% for the first and second part of the beam time respectively, due to the changing MWPC efficiency (This division will be discussed in Sec. 5.3)

²This is, in fact, consistent with a statistical evaluation, giving a hint on a contamination with 10 to 20% artefacts after applying 92% Čerenkov proton suppression in the multiple-cluster analysis.

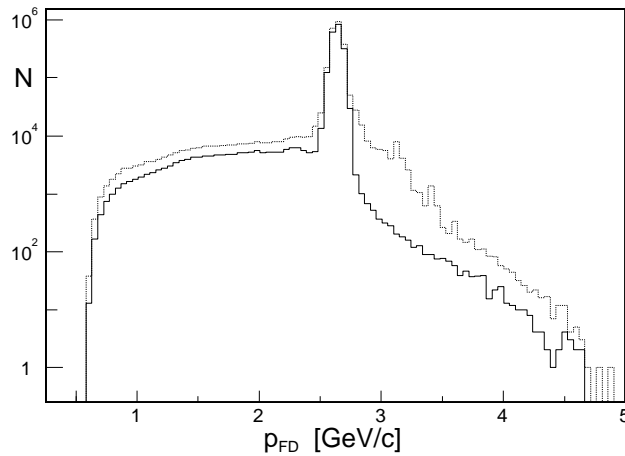


Figure 4.1: Reconstructed momentum distribution for 2.7 GeV/c: In the upper histogram up to 9 clusters per plane were considered for tracking, whereas the lower line shows the distribution for single cluster events selected in every plane.

4.1.2 Track Reconstruction

With the two points determined from the MWPC information described above, a straight line is defined. Using polynomials this line can be traced through the magnetic field to the known target position. The polynomial method used is described in Ref. [65,66] and has been implemented at ANKE and tested by S. Dymov [63]. Thus, the following description is very brief.

The polynomial approach comprises reasonable computing time and accuracy in reconstruction. The information gathered from the wire chambers is used to obtain parameters for a straight line (e.g. $\vec{x}_0, \partial\vec{x}$). The bending of the track in the magnetic field from the spectrometer is approximated by a third order polynomial. In order to obtain a relation between the straight line parameters and the initial three momentum of the particle at the target, the ANKE system has been implemented in Monte Carlo simulations [62]. The parameters describing this relation have been determined individually for every beam momentum and ANKE setting.

Two major assumptions have to be made. The first is that the starting point of the particle is indeed the target position. Several studies have been made on background not originating at the target or being scattered by large angles on their way [63]. Geometrical cuts on the scintillators and the exit window of the D2-vacuum chamber to exclude background tracks have been included in the analysis. The limits are set such that the acceptance for direct tracks is not reduced. It is estimated that the remaining background contribution is below 1% [63]. The second assumption is that, within the experimental uncertainties, one can describe the track of a particle through the chambers as a straight line. The chambers are positioned in a region where the stray field of the magnet is still significant. Nevertheless the parametrisation takes this effect into account at least up to first order. This is due to the fact that the parameters are determined with simulations including the stray field. Further tests with different reconstruction methods show agreement within a maximum deviation of 0.2% [63].

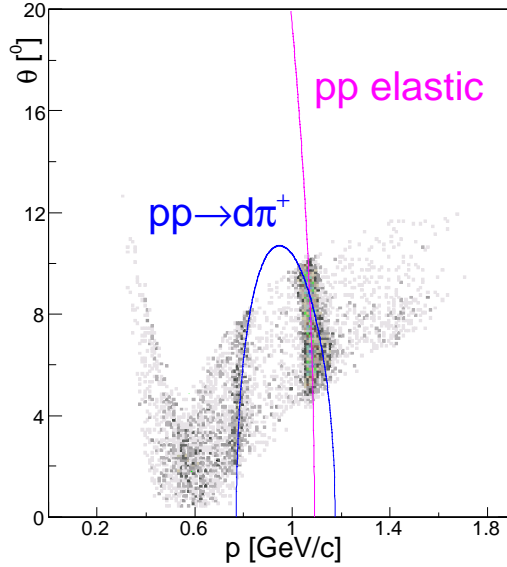


Figure 4.2: Polar angle *versus* momentum at $p_p = 1.1$ GeV/c for a H_2 -target [67]. The borders of the distribution are determined by the acceptance of the system. Shown as curves are the kinematics for pp -elastic scattering and $pp \rightarrow d\pi^+$ (see text).

Comparing the experimental data with kinematics from expected contributing reactions, one finds good agreement. In Fig. 4.2 the experimental distribution of the polar angle *versus* the momentum using a hydrogen target is plotted at a beam momentum of 1.1 GeV/c. Within the acceptance of the system one clearly observes the bands from pp -elastic scattering and $pp \rightarrow d\pi^+$ without applying any further cuts.

A completely independent check of the reconstruction can be carried out using the detection of deuterons in the silicon telescope. This allows us to check the reconstructed polar angle in the forward system in a restricted area. The principle is as follows. The kinematics in elastic two-body reactions is fully determined if one detects just one of the particles. In our case, beam protons are elastically and coherently scattered on a deuteron from the D_2 target. $pd \rightarrow pd$ is unambiguously tagged by selecting deuterons with kinetic energies above 8 MeV at $2.6 \leq p_{\text{beam}} \leq 2.9$ GeV/c in the silicon telescope. This is due to the fact that particles have to emerge from the target with angles larger than 80° to be detected in the silicon telescope. There is no other reaction providing deuterons in this angular range. This fact will also be used for luminosity determination (see Chap. 6). The measurement of the energy of these deuterons ($8 \leq T_d \leq 35$ MeV) with a 1% accuracy (see Sec. 3.3) yields an angular accuracy for the coincident protons in the forward system of about 0.03° , which is comparable with the contribution from angular straggling in the exit window of the spectrometer magnet D2. Comparing the experimental result with the kinematical calculation in Fig. 4.3 for a beam momentum of 2.7 GeV/c, agreement within a few tenths of a degree is found. Note that the statistics in the part with large deviation is small and the events are perhaps only accepted

due to re-scattering. Nevertheless this approach cannot be used for an overall calibration of the forward system, as the coincident protons only cover a narrow band (vertically a few centimetres) and include horizontally only the half of the chamber close to the beam pipe.

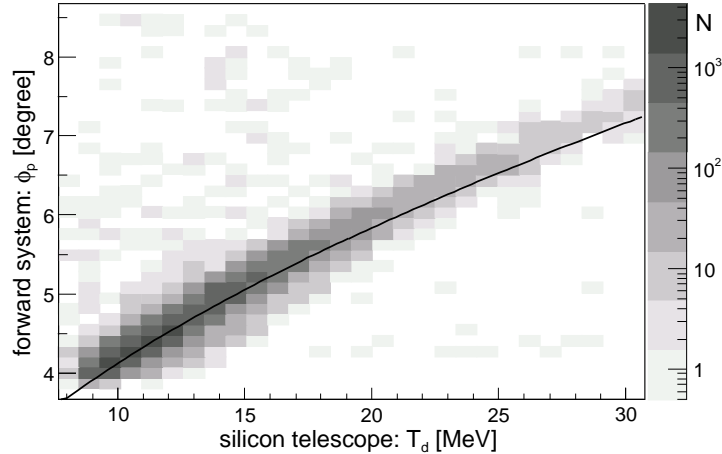


Figure 4.3: Polar angle reconstructed from the forward information alone *versus* the kinetic energy of elastically scattered deuterons identified by the silicon telescope alone (logarithmic scale in number of entries). The line indicates the result from kinematics for *pd*-elastic scattering (calculation in App. A.2).

4.2 Identification of Fast Deuterons

Using the knowledge of the track and momentum for each event, selection criteria can now be defined to identify deuterons with momenta of about 2 GeV/c. The first criterion is the Čerenkov counter response. A momentum-dependent threshold is used for each counter to match the proton suppression factors within the momentum range of interest [68]. Secondly, the energy losses in the two layers of the hodoscope provide two independent distinction criteria.

4.2.1 Čerenkov Proton Suppression

As discussed in Sec. 2.3 on page 13, the response of the inclined Čerenkov counters is β -dependent and thus particles with the same momentum but different mass and hence velocity can be distinguished from each other. Unfortunately for the selection of deuterons, this is not an active criterion but an anti-coincidence with a signal in the counter (which is believed to be passed by the particle). Thus it is clear that any inefficiency or assumption that the particle crossed the counter, where in fact it did not, will lead to a misinterpretation of the particle as a deuteron candidate. Moreover, due to the small Čerenkov light yield and high noise level, the peak from protons is not well separated from the noise. In Fig. 4.4 the amplitude spectra for protons with momenta around 1.1, 1.7 and 2.8 GeV/c are plotted as dotted, solid and dashed line respectively. The first one corresponds in β to deuterons with 2.2 GeV/c. Thus the amplitude distri-

bution can be taken as an approximation for the response of deuterons with this momentum. The latter two distributions show how the amplitudes evolve with particle momentum. As we want to distinguish deuterons from protons in the momentum range from 1.5 to 2.4 GeV/c, a fixed cut level would result in a momentum dependent p suppression efficiency.

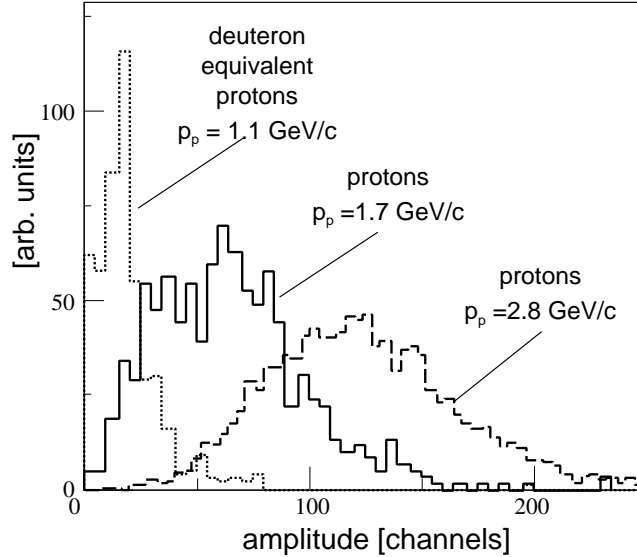


Figure 4.4: Amplitude distributions in a Čerenkov counter depending on the incident proton momenta. Assuming a pure β dependence this can be used to simulate also the response from deuterons.

The strategy of the analysis is as follows: After selecting cleanly reconstructed tracks by the single cluster method (see Sec. 4.1.1) the counter which was crossed by the track is selected. In order to achieve this, a track passing the counter not closer than 5 mm to the counter horizontal borders was required. In the vertical direction even 2 cm were required, because of the counter inclination. These geometrical cuts have been checked using tracks, which provided a signal in the counters.

A calibration was done by selecting protons from data obtained at two beam momenta (1.219 and 2.806 GeV respectively) with a hydrogen target [63, 69]. The small deuteron contribution can easily be suppressed by setting a restrictive upper limit for energy losses in the hodoscope. The protons can be used over a large momentum range to determine the detection efficiency. In the setting used to select deuterons, namely an anti-coincidence, this value corresponds to the proton suppression efficiency and is plotted in Fig. 4.5 *versus* the reconstructed momentum for a fixed threshold. Assuming the Čerenkov response to depend only on β , it is possible to simulate deuterons using protons with lower momenta. This can be extended to the consideration of opening angles (Fig. 2.5(b) on page 14 in Sec. 2.3) without changes. In Fig. 4.5 this region is shaded, as well as the momentum region in which protons have to be suppressed.

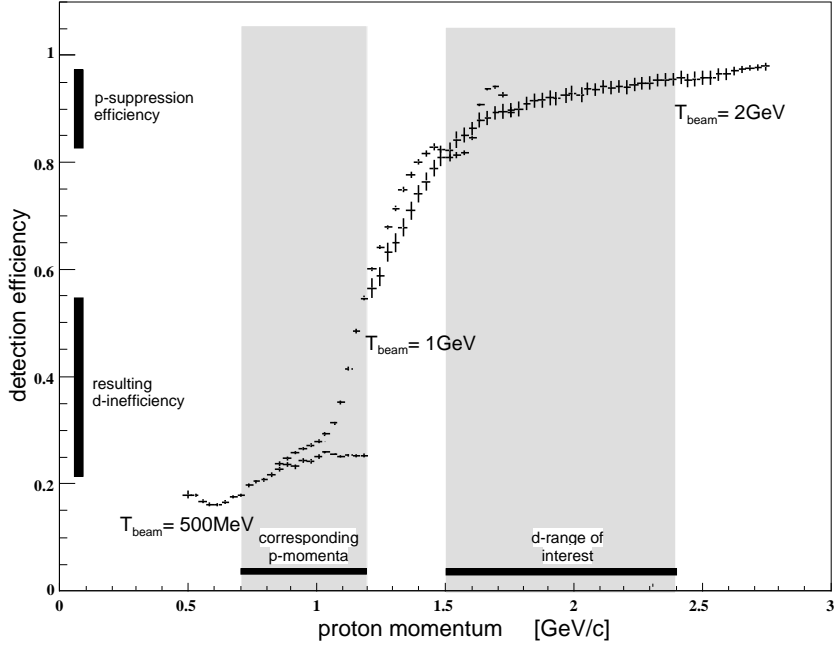


Figure 4.5: Detection efficiency for selected protons over a large momentum range with a fixed threshold [69]. Shaded areas are the corresponding momentum ranges for deuterons and protons (see text).

The detection efficiency in Fig. 4.5 varies strongly with momentum. In the momentum range from 1.5 to 2.4 GeV/c, which has been covered by deuterons from the $pn \rightarrow d\omega$ reaction and thus selected, the proton efficiency changes from 85% at 1.5 GeV/c to about 95% at 2.4 GeV/c. Thus, the proton background, after a selection of deuterons with this threshold level, would differ by a factor of three depending on the momentum. Clearly this would lead to a major distortion of all distributions. In order to avoid this, the detection efficiency *versus* threshold has been calibrated for every 50 MeV/c bin in the momentum range. The result is used to obtain a momentum-dependent threshold which guarantees a constant suppression factor over the whole range.

Finally the goal has been to set the maximum proton suppression efficiency where, for all counters, a constant value at all momenta can be guaranteed. For the analysis of the data from August 2001, a value of 92% has been obtained for the lower counters, whereas only 82% could be achieved for the upper counters³.

4.2.2 Energy Loss in the Hodoscope

For the obtained events the still dominant proton contribution can be further suppressed by the energy losses in the two layers of the forward hodoscope. Due to the low statistics the information has to be summed from all counters in one plane and over large time intervals of beam time. Thus all the photomultipliers must be calibrated beforehand.

³This was due to a bad optical contact between counter and photo-multiplier, which has been fixed subsequently.

Calibration of Energy Losses

Data with a hydrogen target and different beam momenta have again been used. At low beam momenta (around 1.1 GeV/c) the reactions: $pp \rightarrow pp$, $pp \rightarrow d\pi^+$ and $pp \rightarrow pX$ can be easily distinguished using the energy loss in the counters of the hodoscope and the reconstructed momentum (see Fig. 4.6). The two branches from $pp \rightarrow d\pi^+$ and pp -elastic already provide three points for calibration. At high beam momenta (around 2.8 GeV/c), where the channel $pp \rightarrow d\pi^+$ cannot be distinguished, the pp -elastic channel and the proton band itself can be used to provide further calibration points.

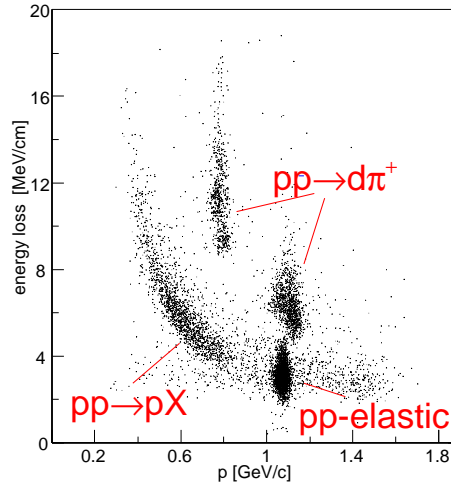


Figure 4.6: Energy loss in the first hodoscope layer *versus* momentum at a beam momentum of 1.1 GeV/c [67]. Visible are protons and deuterons from the indicated reactions.

The program GEANT3 [62] provides the most probable deposited energy ΔE_{mp} as a function of $\beta\gamma$, and this was used to fit the following function for each individual photomultiplier:

$$\Delta E_{\text{mp}}(\beta\gamma) = \frac{f(q)}{g(y)} = \frac{p_1 q^2 + p_2 q + p_3}{p_4 y^3 + p_5 y^2 + p_6 y + 1} \quad (4.1)$$

The fitted form can be factorised into a quadratic function $f(q)$ of the photomultiplier response q and a cubic function $g(y)$ of the vertical coordinate y in the scintillator panel. The latter y -value is determined by the vertical intersection point of the reconstructed track with the scintillator plane. Up to 60 experimental points for each readout channel are used to fit the parameters p_1 to p_6 . Finally the arithmetic mean of the upper and lower signal from one counter is used as the calibrated energy loss in this detector⁴.

⁴Nevertheless a small correction had to be introduced for a change in amplitudes, which occurred between runs 3643 and 3646.

Deuteron Selection

Deuterons with momenta from 1.5 to 2.4 GeV/c on average deposit only about 1 MeV more energy in the scintillators than the corresponding background protons. Nevertheless, applying a 92% proton suppression by Čerenkov counters (see Sec. 4.2.1) and plotting the calibrated energy loss *versus* the reconstructed particle momentum, one can observe a deuteron band (see Fig. 4.7). Furthermore the dependence of the energy loss, approximated by $1/\beta^2$, can describe both particle bands (solid lines in Fig. 4.7).

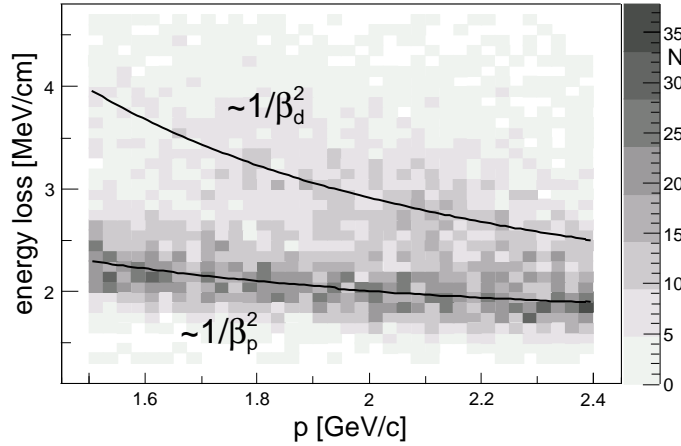


Figure 4.7: Calibrated energy loss in the first layer of the hodoscope *versus* the reconstructed momentum after 92% proton suppression by Čerenkov counters at $p_{\text{beam}} = 2.806$ GeV/c. The expected energy loss dependencies for protons and deuterons are approximated by $1/\beta^2$ and plotted as curves.

In a projection of this figure along the line for deuterons ($1/\beta_d^2$), shown in Fig. 4.8 (dotted line), a deuteron shoulder is observed on a dominating proton background. The same sort of result is obtained for the second layer of the hodoscope. Thus one can apply a cut level indicated as vertical line in Fig. 4.8 also in the second layer. Doing so, the solid line remains, showing a clear deuteron peak with a remaining proton contribution below 10%. This is deduced actively, selecting protons by a signal in the Čerenkov counters and scaling the distribution to the background shoulder (dashed line).

In summary, one can state that deuterons in a momentum range from 1.5 to 2.4 GeV/c can be identified and tracked in the forward detection system. The remaining background (mostly protons) of about 10% does not affect the overall result, as its shape in missing mass is shown to resemble the multi-pion background in $pm \rightarrow dX$ which is interpolated semi-phenomenologically. The approach to subtract the proton contribution integrally has been considered but has not been applied in order to keep systematic uncertainties as small as possible.

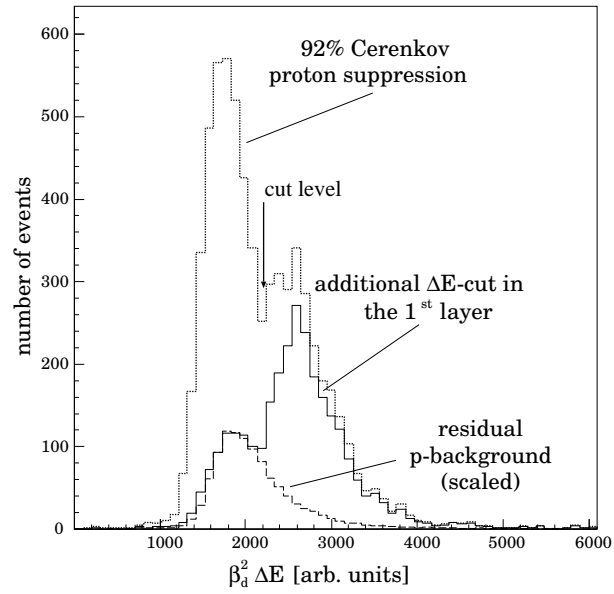


Figure 4.8: Energy loss in the first layer of the forward hodoscope scaled with $\beta_d^{-2} \propto \Delta E(\text{deuteron})$ at $p_{\text{beam}} = 2.806 \text{ GeV}/c$: Shown are distributions using \dot{C} -suppression only (dotted) and using an energy-loss cut in the 2nd layer in addition (solid). The proton contribution has been extrapolated by an active selection of these particles and scaled (dashed).

Chapter 5

Efficiency Determination

Having found a method how to detect a spectator proton and fast deuteron from $pd \rightarrow p_{sp}d\omega$, the efficiency has to be studied in order to normalise the data. As the luminosity will be obtained by the detection of pd -elastic scattering, the efficiencies for the identification of both reactions have to be controlled. For the latter reaction, only a slow deuteron is required, which can be detected with high efficiency in the silicon telescope. All the factors contributing in this case are discussed in Chapter 6 “Luminosity Determination”. However, for ω -production, the detection of a slow proton in the silicon telescope in coincidence with a fast deuteron in the forward system is required. The low, inhomogeneous and non-constant efficiency of the wire chambers in the forward system turned out to be a challenge for the analysis. Furthermore, the identification efficiency of the fast deuterons by means of Čerenkov counters and double energy loss cut in the hodoscope has to be taken into account.

5.1 Trigger and Data Acquisition

The trigger formed by a coincidence of the forward hodoscope and the telescope (described in Sec. 2.4) is used for both the luminosity determination as well as the measurement of $pd \rightarrow p_{sp}d\omega$. The intrinsic efficiency of the detectors and dead-time corrections of the order of 1% cancel out in the normalisation. Thus, only large or differing contributions for both processes are considered here. The charge efficiency in silicon is assumed to be 100%. The energy-loss distributions presented in Chap. 3 show that this is a reasonable assumption. Several approaches show that the triggering efficiency in the scintillator hodoscope is well above 95%. Furthermore, the mean energy loss for both spectator protons and deuterons used for normalisation is on average the same in the second layer of the telescope used for triggering. The gate of the forward hodoscope is stable within a few nanoseconds for any particle type. However, the timing from the silicon detector in the telescope changes with deposited energy, as shown in Fig. 5.2. This is due to the amplitude dependence of the fast shaper output signal (10 ns integration and 1 μ s differentiation time constant).

The trigger gates of both the forward system and the telescope are about 200 ns wide and have been adjusted such that the telescope gate is on average 80 ns before the forward gate (see Fig. 5.1 for illustration). Thus, the coincidence

timing is determined by the forward hodoscope. This ensures that the narrow gate for the chamber read-out to be always correct, allowing a shift in timing for the silicon read-out. Nevertheless this does not disturb the amplitudes read out for the telescope, because of its long shaping times ($1 - 3 \mu\text{s}$).

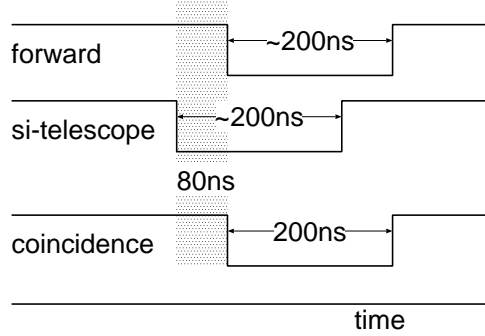


Figure 5.1: Sketch of the coincidence timing. The time axis shows the sequence of the gates. The trigger set as a coincidence only starts if both gates are present, but is fixed to 200 ns length.

The timing for the coincidence trigger relative to the forward system starts to shift only if the silicon trigger signal is late by more than 80 ns. In this case the gate from the silicon telescope in Fig. 5.1 would start after the forward gate. As the gate for the wire chamber read-out electronics should be correct within 20 ns, a maximum shift of 100 ns can be accepted without efficiency losses. From Fig. 5.2 one can see that in fact almost all the events within the correlation band fulfil this requirement. The tail of the band reaches only below 500 keV energy deposit, a mean time delay of 40 ns. At a delay of 70 ns only few percent of the events remain. Thus the trigger efficiency has not been corrected for and the uncertainty due to this is estimated to be well below 1%.

However, the dead-time of the data acquisition presents a strong correction for the luminosity determination. This value has been corrected for, even though effectively the correction cancels out in the normalised ω cross sections. The dead time is determined by the time interval during which the data acquisition is busy processing the previous event and cannot yet accept another event (about $180 \mu\text{s}$). Comparing this to typical trigger rates of a few 1000/s a considerable fraction of events statistically fall into this interval and are thus excluded from further analysis. Neglecting the trigger dead-time (about 200 ns), the correction factor is the ratio of triggers (so called “trigger-in” events T_{in}) to the accepted events by the data acquisition (T_{out})¹. As the trigger rates during the experiment were not stable, ranging from a few hundred to several thousand events per second, the dead-time was accounted for on a run-by-run basis. The obtained correction factors $f_{\text{dt}} = T_{\text{out}}/T_{\text{in}}$, reaching from close to unity up to 2.2, are listed in the run list in Table C.1 on page 99.

¹In principle, the dead-time for each trigger can differ. Nevertheless, no significant differences for the individual T_{in} to T_{out} rates in comparison with the integral rates were observed. Thus, summed rates of all triggers were used for the analysis.

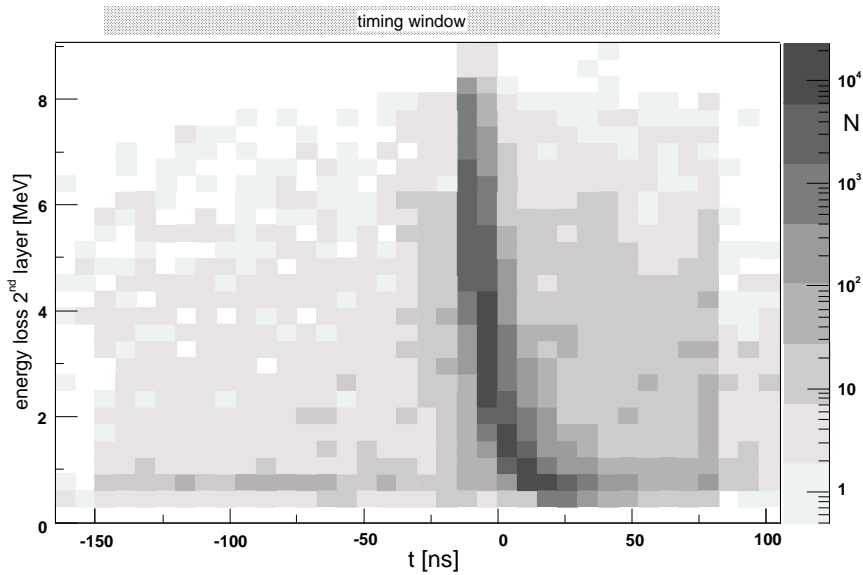


Figure 5.2: Deposited energy in the second layer of the telescope *versus* the time relatively to the mean value of the distribution.

5.2 Detection in the Silicon Telescope

Since the energy range for the particle identification is divided into two groups, this is also the natural separation for the efficiency determination. For the low energy spectator protons the inefficiency is dominated by the uncertainty in energy loss in the first layer and the rejection of multiple hits in the second layer. To deduce the first layer efficiency, particles identified and tracked with the second and third layer only, have been analysed. About 10% of the protons selected as being in the first layer acceptance are not observed within a range around the expected energy loss in this layer. The detection efficiency in the second layer has already been discussed in the previous Section, and affects the luminosity determination as well as the ω analysis. Thus, these corrections effectively cancel out. The ratio of rejected events due to multiple hits in the second layer (see Sec. 3.2) was recorded run-by-run. This factor f_{m2} (listed in Table C.1 $\langle f_{m2} \rangle \approx 1.06$) is used as an efficiency correction factor for each run². Thus the value of $90\%/f_{m2}$ has been taken with an estimated systematic error of 3% as efficiency for the detection of spectator protons with $2.6 \leq T_{sp} \leq 4.4$ MeV.

For the higher energy protons and deuterons the same multiplicity factor can be used for the second layer together with the corresponding value for the third layer f_{m3} ($\langle f_{m3} \rangle \approx 1.01$). As the normalisation is done with deuterons with kinetic energies between 17 and 18 MeV the efficiency for these can be set

²This implies that the rejected events contained a track, which could otherwise be analysed. To extract the ratio of “good” to pure noise events rejected by this method, the ratios of single to multiple hits has been analysed for several common thresholds. The difference from the simple assumption made before was found to be negligible. Please note, that the corrections are of the order of a few per cent and thus systematic errors are negligible.

arbitrarily to 100% divided by the multiplicity factors given above.

In the 5 mm thick third layer another effect arises due to the read-out of the 200 strips in four resistor chains with two-read out channels each (refer to App. B.3.2). For an analysis of the output in terms of position, the threshold for each channel translates into a floating threshold over the length of the detector. The acceptance obtained is shown in Fig. 5.3 for stopped protons and deuterons. The latter are seen as a triangular enhancement between -14 and -22 mm. For the luminosity determination deuterons are selected in the indicated range ($17 \leq T_d \leq 18$ MeV) on the right hand side of Fig. 5.3. The small acceptance correction will be taken into account in Chap. 6. However, as the rather small number of spectator protons in this range has not been analysed for ω production for several reasons, a tricky acceptance correction has been omitted in favour of the following simple approximation. From the area of the inefficient regions and the slope of the spectator proton distribution with kinetic energy, the overall effect was estimated to correspond to an efficiency of $(65 \pm 10)\%$ for the total range.

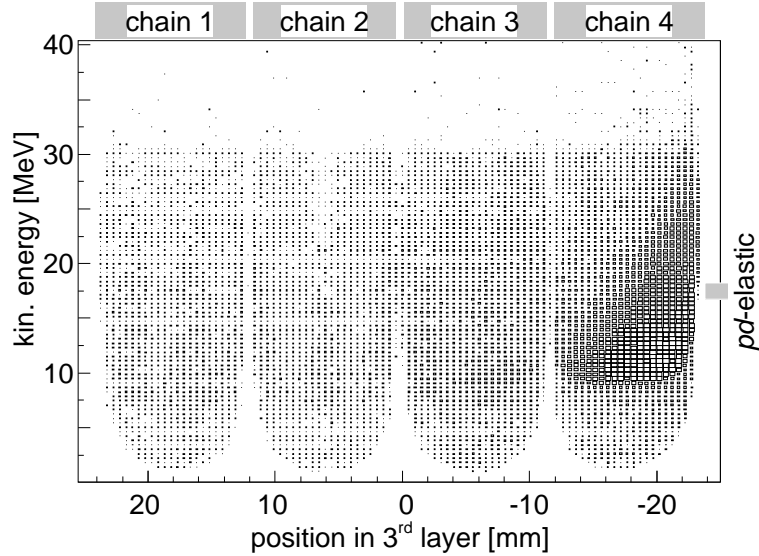


Figure 5.3: Total kinetic energy of protons and deuterons *versus* the position perpendicular to the strips (i.e. $-Z$ coordinate beam up stream) in the 5 mm thick 3rd layer of the telescope. The dependence of the acceptance on the energy loss and position is clearly visible by the rounded lower borders.

The Overall Results for the deuterons selected to determine the luminosity (next chapter) and the two ranges for spectator protons are given in Table 5.1. Arbitrarily, the detection efficiency for the deuterons with 17 to 18 MeV kinetic energy is set to 100%, apart from the multiple-hit correction. As the detection of these particles determines the normalisation, any inefficiency affects protons and deuterons in the same way and will finally cancel out.

particle	kinetic energy	overall efficiency
deuteron	17 – 18 MeV	100%/($f_{m2} f_{m3}$)
proton	2.6 – 4.4 MeV	(90 ± 3)%/ f_{m2}
proton	8 – 22 MeV	(65 ± 10)%/($f_{m2} f_{m3}$)

Table 5.1: Resulting efficiencies for the detection of protons and deuterons in the silicon telescope. The multiplicity correction factors are taken into account run by run (values listed in Table C.1).

5.3 Tracking in the Forward System

As discussed in Sec. 4.1, a track is formed using the two X and two Y-wire planes from the multi-wire proportional chambers with the requirement of a single cluster in each plane and scintillator response. Due to this unambiguous track reconstruction, the tracking efficiency is identified with the product of the efficiencies from the chamber planes. It will be shown later that this approach allows us to correct for the total tracking efficiency within a few per cent. In this section it will be shown how these efficiencies can be obtained and how their development in time and distribution over the planes behave. Furthermore, a method to correct for the strongly inhomogeneous and varying efficiencies is presented, concluding with two cross-checks. First, data taken at the same beam energy but with strongly different efficiencies have been compared and a systematic error of 5% deduced. Secondly, the approach has been tested by a completely independent measurement. Protons from pd -elastic scattering, identified by a deuteron in the silicon telescope alone, have been used to scan a small region of the chamber. Adding a 5% correction for the hodoscope efficiency, the efficiency-corrected spectra from the forward system correspond to the spectra obtained by the detection of a deuteron in the telescope.

5.3.1 Method of Efficiency Determination

To determine the efficiency of the two X and two Y wire planes used for the tracking, the following procedure has been developed [63]. Consider e.g. the X wire plane in the second chamber (X2W). A sample of events has first to be found, in which an unambiguously defined track crosses the plane under consideration. Of course, this plane itself has to be excluded from the method used to find this track. In order to obtain a track under such conditions the strip information from the other plane of the same chamber – i.e. the Y strip plane in the second chamber (Y2S) – has been used, together with the remaining three wire planes (X1W, Y1W, Y2W). Due to the inclination of the strip plane to the wire plane by 18° (see Sec. 2.3), a second X coordinate is obtained within a $\sigma = 5$ mm accuracy by the combination of wires and strips in the same plane (Y2W and Y2S). In Fig. 5.4 the procedure is sketched for illustration. To use the tracks for the efficiency determination, ambiguous tracks have to be excluded reliably. Thus, only events with a single cluster per plane have been accepted and conditions for crossed counters and exit window were required as for regular tracking³.

³This is a prerequisite for the efficiency determination. Nevertheless, the same condition is applied also in the further data analysis as discussed in Sec. 4.1.1.

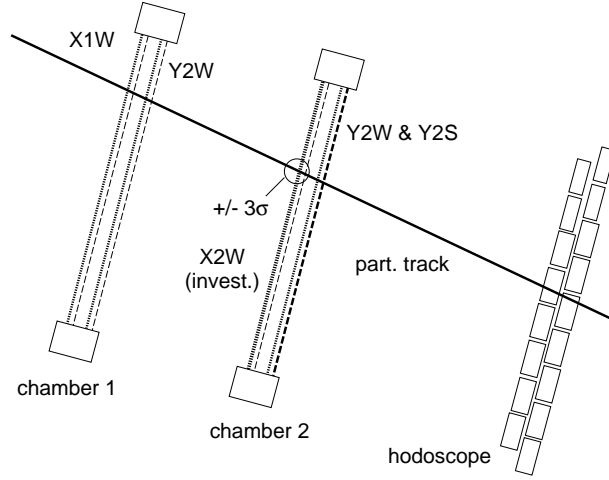


Figure 5.4: Schematic drawing of the efficiency determination in the X plane of chamber 2 (X2W) by a track reconstructed with the wire planes of chamber 1 (X1W and Y1W) and the Y wire and strip plane in chamber 2 (Y2W and Y2S). Wire and strip planes are sketched as dotted and dashed lines respectively.

Subsequently, the intersection point of the determined track with the investigated plane is determined. In a region of 3σ around this point a cluster is expected to appear in case of an efficient detection. The value ϵ_D determined is then just the ratio of events where a cluster was found N_D to the total number of tracks N having passed the considered cell. However, in the case of several clusters in the investigated plane ϵ_D cannot easily be attributed to an efficiency factor in the tracking procedure. At first an oscillation – appearing quite often during the measurements – can fake an efficient event. Secondly, the “multi-cluster analysis” (which was considered in Sec. 4.1.1 but rejected for several reasons) might well reject the considered cluster in favour of another track and hence make the determined efficiency difficult to interpret. This is just another reason to use the “single cluster analysis” introduced in Sec. 4.1 for the data analysis. Thus, identical conditions were required for this $\approx \pm 15$ mm region around the track intersection point as for the ω analysis. An event was determined to be efficient, if a single cluster in the investigated plane with a width of one or two wires was found this region. To calculate the statistical error of the ratio (ϵ_D) to the total number of tracks (N), the number of inefficient events $N_M = N - N_D$ has been introduced. The result from the binomial approach, described in App. A.3, is:

$$\epsilon_D = \frac{N_D}{N} = \frac{N_D}{N_D + N_M} \quad (5.1)$$

$$\sigma\epsilon_D = \frac{1}{N^2} \sqrt{\frac{N}{N-1}} \sqrt{N_M^2 N_D + N_D^2 N_M}$$

5.3.2 Global Plane Efficiency

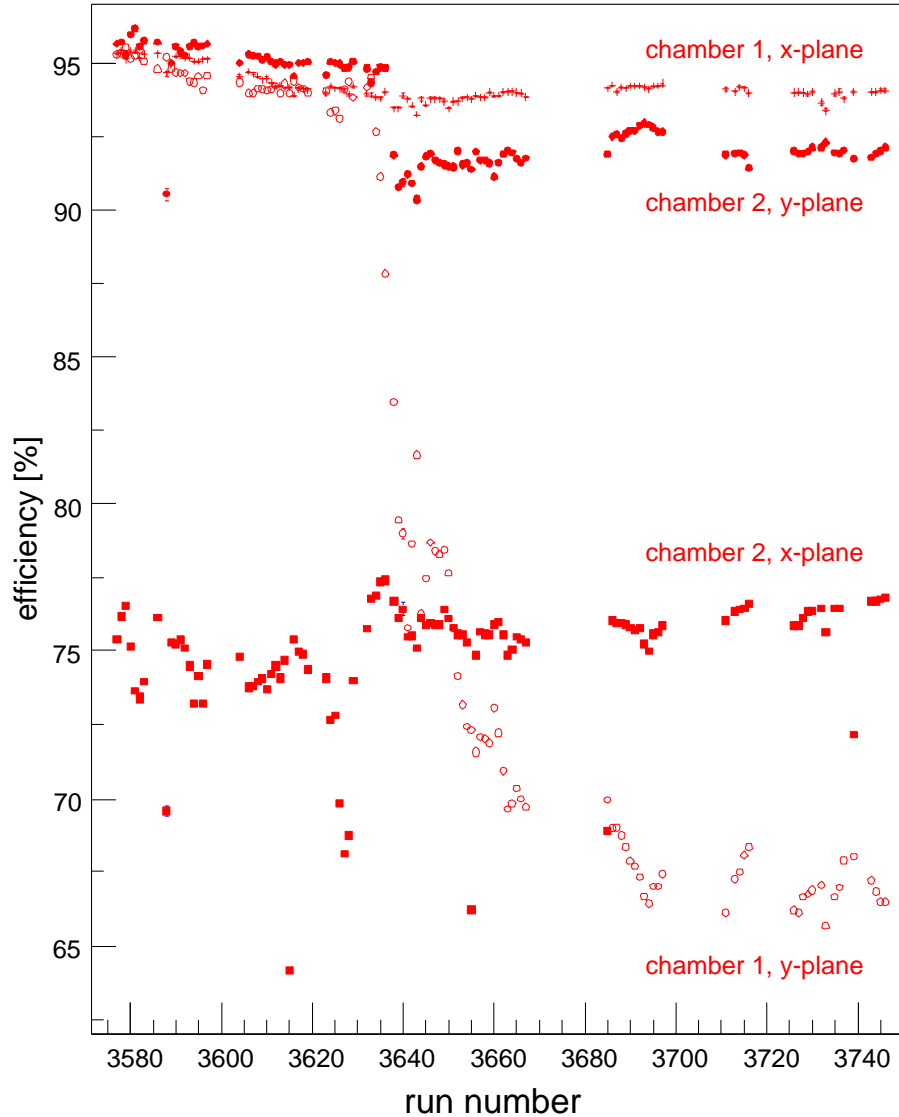


Figure 5.5: Average efficiency in each plane developing over the complete beam time (run numbers)

The efficiencies obtained separately for each run during the beam time in August 2001 are shown in Fig. 5.5. The observations are the following:

- In a few runs some plane efficiencies are lower by large factors. This may be explained by oscillations that are taken as inefficiencies due to the single cluster requirement⁴. These few runs were excluded from the

⁴Accepting also multiple clusters these single deviations disappear, but the average effi-

analysis, accepting a loss of 7% in statistics (see Table C.2).

- The X-plane of chamber 1 and the Y-plane of chamber 2 provide an efficiency of around 95% in the beginning of the beam time. The latter drops a few per cent around run 3638 but stabilises above 90%.
- The X-plane of chamber 2 shows an unstable and rather low efficiency of about 75%, stabilising at an even slightly higher level after run 3640.
- The Y-plane of chamber 1 starts with an efficiency above 95%, which drops dramatically after run 3633. The change is steady, but seems to ease out after run 3662. By the end of the beam time more or less stable conditions (within 5%) are reached at an efficiency level of only about 65%.

Multiplying these numbers, the average overall efficiency changes from about 63% to 42% in the course of the beam time. From the location of the four sets of beam momenta (see Fig. 5.5) it is clear, that no global factor can be used to correct the data. One could of course use the efficiency values obtained for each run to correct the data, but, as we will see in the following, the efficiency distributions are very inhomogeneous too. Thus such an approach would even fail integrally as the distributions differ strongly for protons from elastic scattering and deuterons from the reaction $pn \rightarrow d\omega$.

5.3.3 Spatial Distributions

In order to study these effects, each plane was artificially subdivided into 20 by 20 cells, each corresponding to an area of roughly $2 \times 2 \text{ cm}^2$. For each of these cells the efficiency was obtained. As an example the efficiency distribution over the Y plane of chamber-1 is shown for a run at the beginning and at the end of the beam time in Fig. 5.6 (a) and (b) respectively. Dramatic changes in the efficiency were observed from run to run and from cell to cell within the later run itself. Large variations between cells at the border might be explained by statistical fluctuations. However, also in regions where high statistics has been gathered, the efficiencies vary from 20 to 95%. The distortion of the experimental distributions can already be observed from the experimental data. From this observation and the considerations on the averaging effects done before, and it is obvious that no averaging over the full plane is feasible.

It has been suggested that one could determine the efficiency individually for each track by the product of the efficiencies of the cells in the four planes, which contain the track coordinates. However, the approach to use the individual maps obtained for each run is not feasible because the statistics is very low for some cells (few events). Nevertheless, the time development of individual cells seems to follow certain systematics, as shown for example for a few cells in Fig. 5.7. It is observed, that the time development in the individual cells follows qualitatively the development of the average efficiency (see Fig. 5.5). This has been observed in other cells and planes too, even though it was not possible to check all 1.6×10^5 values and additional errors individually.

ciency is only improved by 10% or 20% for the beginning and end of the beam time respectively.

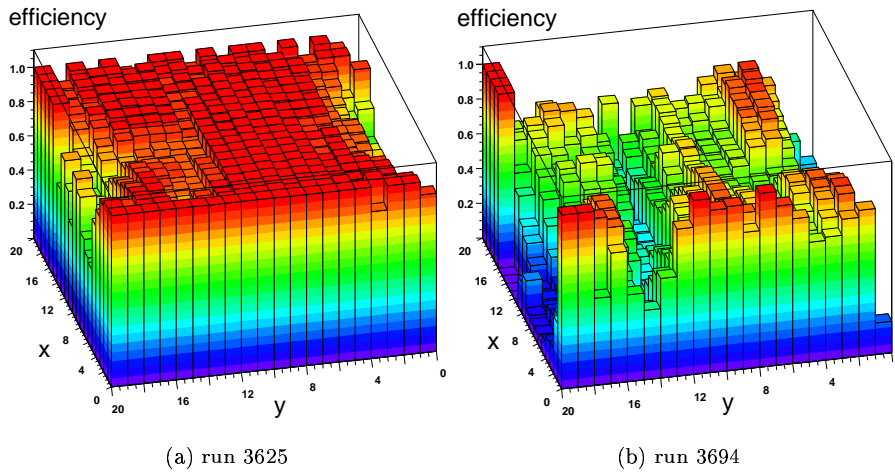


Figure 5.6: Spatial efficiency distribution ($2 \times 2 \text{ cm}^2$ cells) in the Y plane of chamber 1 for a run in the beginning and end of the beam time. The horizontal (x) and vertical (y) axis are plotted in units of cells.

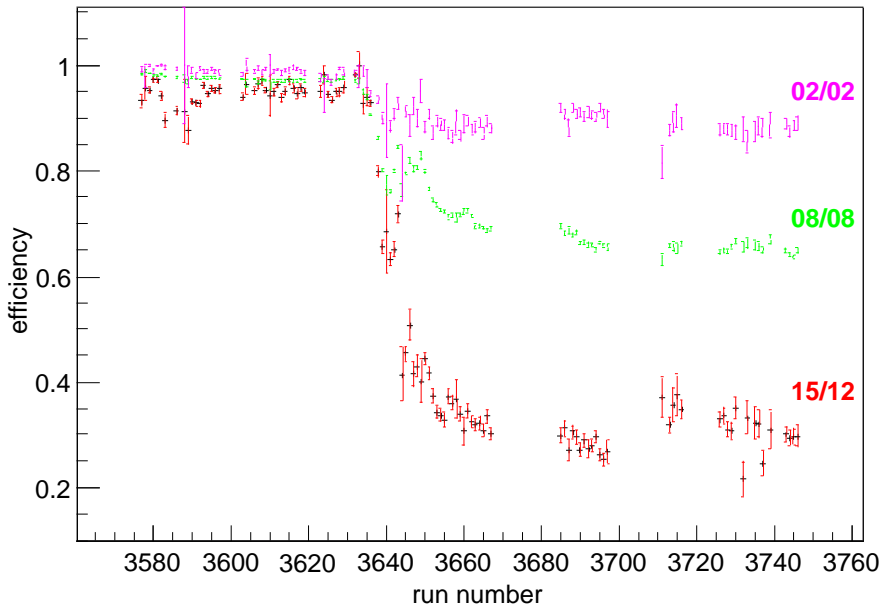


Figure 5.7: Efficiency of some selected cells in the Y plane of chamber 1 as development over run numbers. Please note, that in these cells rather high statistics is gathered and thus the statistical errors shown are small compared to cells at the border regions.

5.3.4 Chosen Procedure

The final procedure to determine efficiency maps has been chosen, combining the maximum reduction of uncertainties with a reasonable loss in statistics due to rejected data. At first, files which showed a strong decrease in average efficiency, as observed in Fig. 5.5 were excluded. Furthermore, all runs under doubt for other reasons were rejected as well from the analysis at this stage. In table C.2 on page 100 all these runs are listed marked with the reason for exclusion. Two time periods where the average efficiencies stayed within $\pm 2\%$ constant have been identified, i.e.:

- the beginning of the beam time from run 3577 to run 3625,
- and the end of the beam time for the runs 3663 to 3746.

However, the structure of the maps with the 20×20 cells has been preserved. As mentioned before, the behaviour of the average is reflected generally also in the individual cells, as shown for example in Fig. 5.7. Subsequently, two sets of maps are produced merging the individual cells over the accepted runs:

Cells with low total statistics (≤ 100 events) or very low efficiency ($\leq 25\%$) have been identified in both of the two sets. Any cell which fulfils this condition in either one or both of the sets has been removed thereafter and consequently excluded from the acceptance for the detection of particles in this system.

5.3.5 Cross-Checks of the Method

The data have been corrected with the provided maps. The efficiency with which a track is reconstructed is thus determined by the product of the four individual efficiencies in the cells lying on the particle trajectory. This value can either be introduced in the simulations (as done later) or the inverse value can be used to weight the reconstructed tracks in the data analysis⁵. The latter approach is used for the two cross-checks presented in this section.

Consistency Check

Please recall the strongly changing efficiency in Fig. 5.5 on page 41. For one beam momentum – namely $2.6 \text{ GeV}/c$ – data were taken for the two strongly differing efficiency regimes in which the two sets of efficiency maps were produced. The fact, that the conditions in terms of efficiency changed completely but the beam settings were unchanged from one to the other regime, can be used as a check of the correction method. Thus, in Fig. 5.8 the distribution of the tracks on the exit window of D2 is shown for the first and second part of the data at $2.6 \text{ GeV}/c$ with high and low efficiency respectively. The solid lines are uncorrected distributions, showing a significantly different shape, whereas the corrected values (points with statistical error-bars) follow a similar shape for both data sets.

⁵Both approaches have been compared to show that they produce identical results within the statistical errors of the measurement.

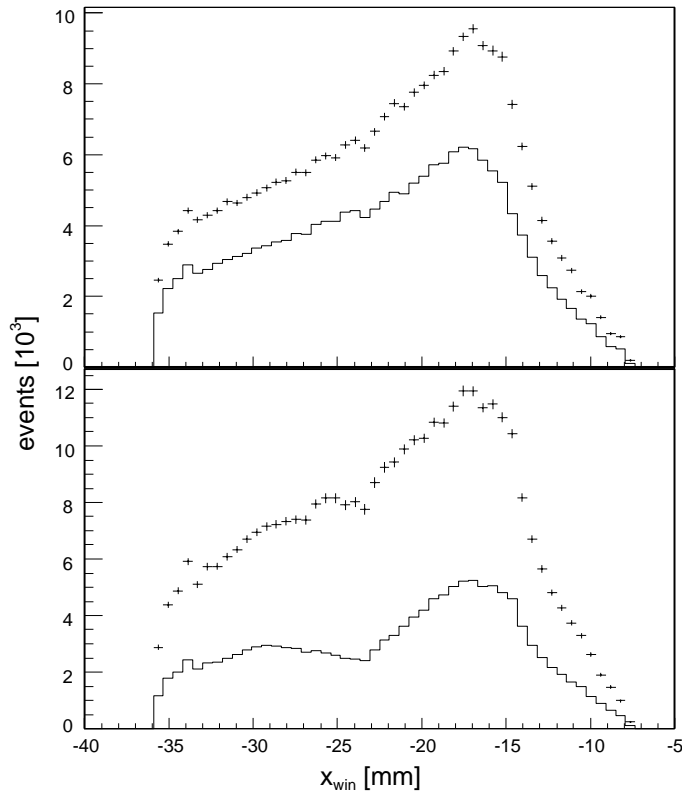


Figure 5.8: Comparison of distributions for two sets of data with different chamber efficiencies at 2.6 GeV/c. The uncorrected spectra (lines) differ significantly, whereas the efficiency-corrected distributions (points with error bars) are similar in shape to within $\pm 5\%$.

For all track parameters and physical observables, such as angles and momenta, the ratios of the two data sets were obtained. Even though, large changes were observed without correction in the distributions, they become flat within $\pm 5\%$ after applying the efficiency corrections. Thus, this value has been taken as the estimate for the systematic error in the distributions.

Independent Check by pd Elastic Scattering

Another way to check the efficiency correction is to take the pd -elastic events selected by the silicon telescope. As described at the end of Sec. 4.1 on page 25, this method covers a very restricted area of the forward system. However, as was done for the tracking, it enables us to do a completely independent check of the efficiency in this region. As shown before, the kinetic energy of deuterons in the silicon telescope corresponds to a fixed angle for forward emitted protons. As these protons also have a fixed momentum, the position in the wire chambers is determined within 2 mm. Thus, the distribution in kinetic energy of these deuterons shown in Fig. 5.9 is a very sensitive tool for the wire chamber efficiency. Moreover, the detected deuterons with $T_d \geq 8$ MeV guarantee

the coincident protons to be fully in the acceptance of the forward system⁶. Hence, the distribution obtained only from the telescope information and the trigger (solid line in Fig. 5.9) can be compared with distribution requiring a reconstructed track in the forward system additionally (dashed line). Points with error bars in Fig. 5.9 show the same events including the event-by-event efficiency correction.

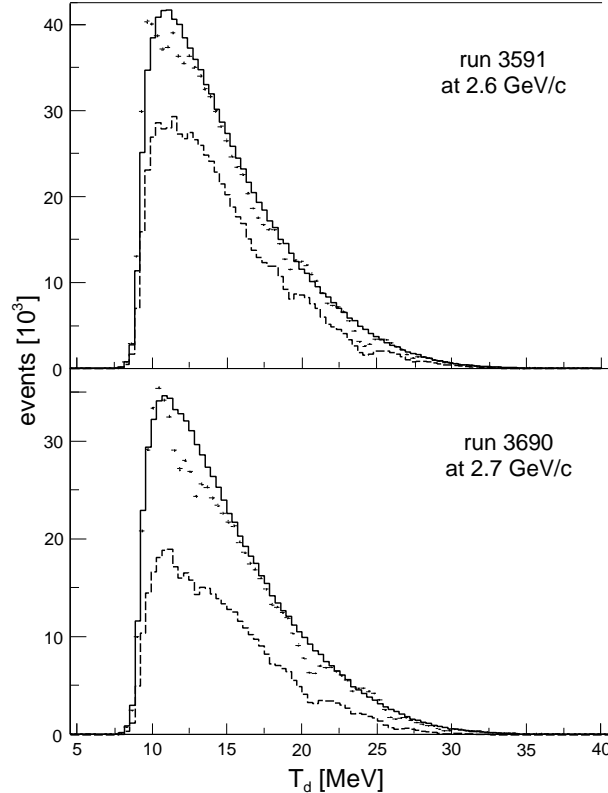


Figure 5.9: Kinetic energy distribution of deuterons from pd elastic scattering in the silicon telescope in the beginning and end of the beam time: selected by the telescope alone (solid line), with a coincident track reconstructed in forward (dashed line), and weighted by efficiency (points with error bars)

One observes the reproduction of the spectra within a few per cent. It is clear from the method that structures which are smaller than the cell size cannot be corrected for. Nevertheless, irregularities in the efficiency-corrected spectra can be understood. Note that a change in 1 MeV kinetic energy here corresponds to roughly a 1 mm shift in the wire chamber. Another effect can be attributed to the inefficiency of the scintillation counters. Though the trigger only requires an OR of both layers, a track is, however, only reconstructed if a signal in both layers has been present for the appropriate counters. This criterion is weak, as tracks reconstructed missing the fired counter by up to 1 cm, were accepted.

⁶At $p_{\text{beam}} \geq 2.8 \text{ GeV}/c$ the forward acceptance starts to cut in at $T_d \leq 10 \text{ MeV}$.

Only in the elastic channel, shown here, is such a kinematic correlation valid, whereas the deuterons from ω production are distributed very broadly across the chamber. Thus the shape on a larger scale and the integral reproduction is more important. It is observed that the overall shape is reproduced well but the integral values are slightly under-predicted by the method. Thus, the overall efficiency for the tracking together with the proposed event-by-event efficiency is deduced to be $(95 \pm 3)\%$.

5.4 Fast Deuteron Identification

Please recall that the fast deuteron identification is done in three steps, namely the anti-coincidence with a signal in the corresponding Čerenkov counter and the selection of a range of energy losses subsequently in both layers of the hodoscope. In order to obtain the efficiency for deuterons resulting from these selections, an independent criterion for the deuteron selection was chosen. The identification of a π^+ meson in the positive side detection system (PD) enables us to determine the type of the coincident particle in the forward detection system (FD) via time-of-flight (TOF)⁷.

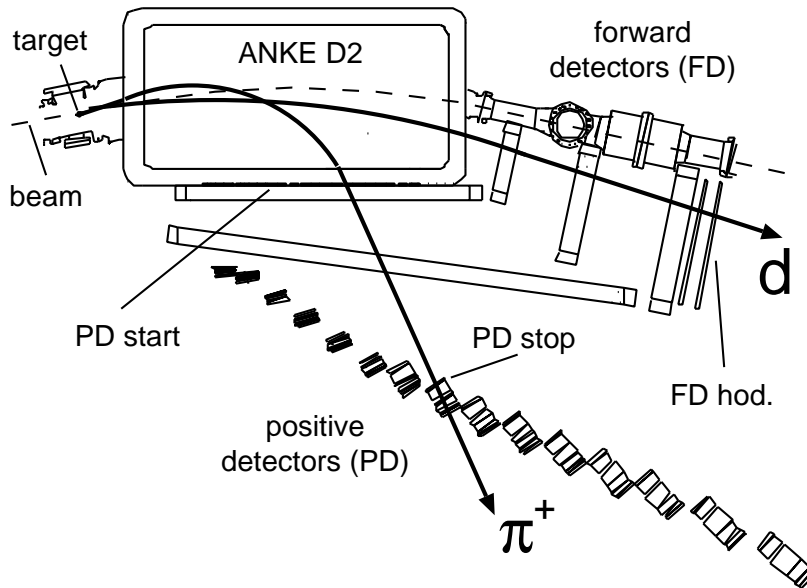


Figure 5.10: Sketch of the D2 vacuum chamber and the forward (FD) and positive side (PD) detection system. The time information from the PD start and stop counters together with the FD hodoscope provides a criterion to select coincident π^+ - d events in the set-up.

⁷Note that this criterion does not imply a single specific reaction channel, but comprises various reactions with a deuteron and pion in the final state. The analysis of $pn \rightarrow d\omega$ is not feasible with this selection due to the small acceptance.

The procedure is as follows: Pions are identified via TOF between the start and stop counters of the PD system⁸. Using correlated protons with a fixed momentum in the FD system, the timing signals in the stop counters could be adjusted for each start-stop combination in the PD system. The time difference to the forward hodoscope provides a measure for the time-of-flight of particles from the target to the hodoscope. This value is plotted in Fig. 5.11 *versus* the reconstructed momenta of the particles. Bands from protons and deuterons are clearly seen.

Projecting these events along the indicated deuteron line and requiring the tracks to be accepted geometrically, one obtains the solid line in Fig. 5.12. Applying subsequently the 92% Čerenkov suppression one obtains the dashed line. The additional energy loss cuts in the hodoscope lead to the dotted line in this figure. The total selection is identical to the selection applied for the deuteron identification in the analysis of the $pn \rightarrow d\omega$ reaction. As expected, the cuts suppress the protons by orders of magnitude, whereas the number of deuterons is only slightly reduced.

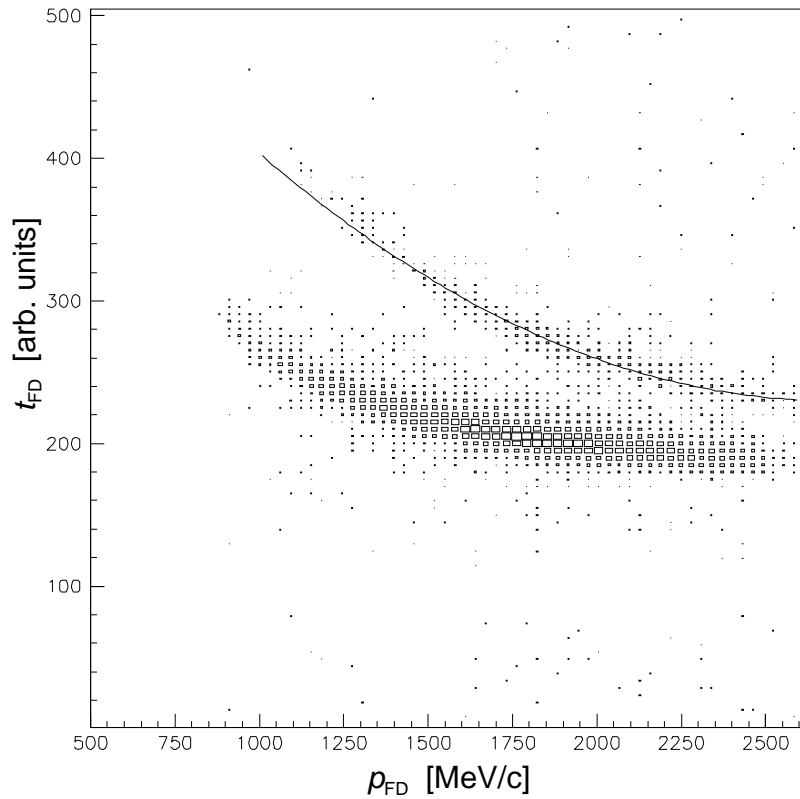


Figure 5.11: Time difference between the forward hodoscope and the adjusted PD stop counters *versus* the reconstructed momentum in the FD system. The line indicates the shape of the deuteron band.

⁸This technique is a general application of this detection system and is described in detail in Ref. [51].

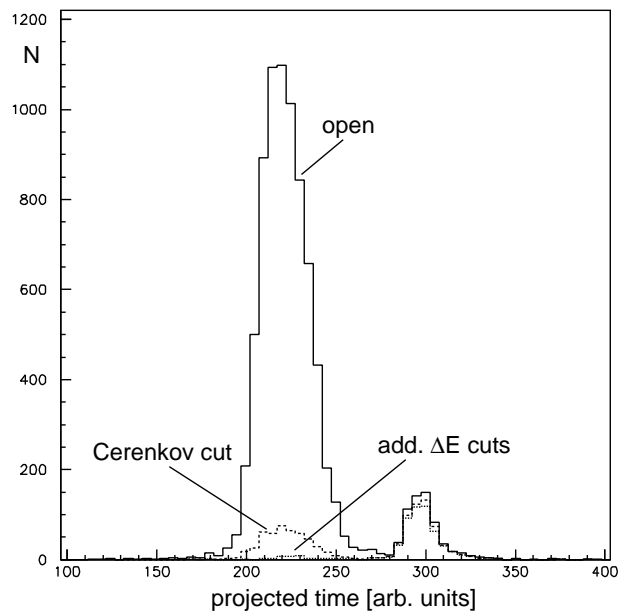


Figure 5.12: Projection of Fig. 5.11 along the deuteron line (solid line). Subsequent application of the cuts used for the $pn \rightarrow d\omega$ analysis lead finally to the dotted line.

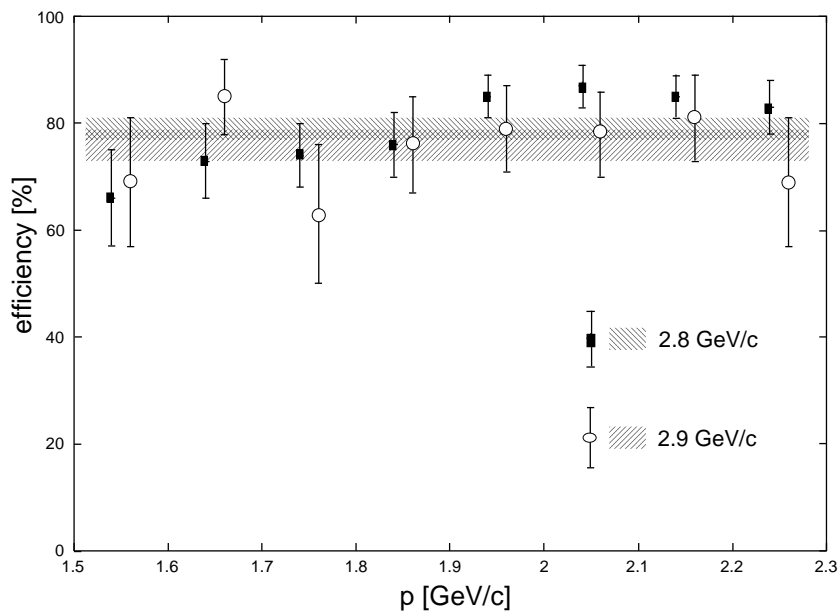


Figure 5.13: Efficiency of the deuteron selection with statistical errors *versus* momentum for 2.8 and 2.9 GeV/c beam momentum (closed squares and open circles respectively). Note that both sets are obtained within the same bins, but their markers are shifted for better illustration. The averages are shown with their statistical errors as left and right hatched areas respectively.

To study any possible systematic dependence, the efficiency of the deuteron selection is plotted for 8 bins in momentum for the two beam momenta in Fig. 5.13. This efficiency is calculated from the ratio of deuterons after applying all cuts to the initial amount in the peak. The statistical errors shown are calculated by the binomial approach as in Eq. 5.2. One observes, that all values and their averages of $(79 \pm 2)\%$ and $(76 \pm 3)\%$ for 2.8 and 2.9 GeV/c respectively (hatched areas in Fig. 5.13) coincide within statistical errors. The presented statistics comprises all available results for these considerations. Thus the overall efficiency for the deuteron identification is estimated to be 78% with a systematic error not larger than 5%. Note that the coincident selection of protons in the silicon telescope does not change the obtained ratio within the statistical errors. The proton contribution remaining after all cuts, $(11 \pm 5)\%$, is compatible with the 10% deduced before (see Sec. 4.2.2).

5.5 Overall Result for the $pd \rightarrow p_{\text{sp}}d\omega$ Reaction

All the contributions to the overall efficiency for detecting the spectator proton p_{sp} and deuteron from the reaction $pd \rightarrow p_{\text{sp}}d\omega$, the obtained efficiencies and correction factors are listed in Table 5.2. Due to the normalisation procedure, the global efficiencies of the trigger and the second layer in the silicon telescope could be set to 100%. The dead-time of the data acquisition and the multiple hits in the silicon counters are corrected for run-by-run with the factors f_{dt} and $f_{\text{m}2/3}$ respectively⁹. The efficiency of the forward tracking is taken into account by the “track-weight” individually for each event. The resulting values for the two ranges of spectator energies, displayed in the last two rows, reflect the total correction factors for the data analysis. The acceptance will be introduced by simulations, and the normalisation with pd elastic scattering is discussed in the next Chapter.

	global efficiency	correction factor	
		run-by-run	event-by-event
trigger	100%	—	—
data acquisition	—	f_{dt}	—
p_{sp} in layer 1	$(90 \pm 3)\%$	—	—
p_{sp} in layer 2	100%	$f_{\text{m}2}$	—
p_{sp} in layer 3	$(65 \pm 10)\%$	$f_{\text{m}3}$	—
d tracking	$(95 \pm 3)\%$	—	track-weight
d identification	$(78 \pm 5)\%$	—	—
overall result			
$2.6 \leq p_{\text{sp}} \leq 4.4 \text{ MeV}$	$(67 \pm 7)\%$	$f_{\text{dt}} f_{\text{m}2}$	track-weight
$8 \leq p_{\text{sp}} \leq 22 \text{ MeV}$	$(48 \pm 12)\%$	$f_{\text{dt}} f_{\text{m}2} f_{\text{m}3}$	track-weight

Table 5.2: Global efficiencies, used as reciprocal value for weighting, together with the correction factors applied individually for each run (see Table C.1) and the event-by-event determined track weight in the MWPCs.

⁹ $f_{\text{m}2/3}$ corresponds to $f_{\text{m}2}$ or $f_{\text{m}2} f_{\text{m}3}$ depending on whether the protons are stopped in the second or third layer.

Due to low statistics, the large uncertainty in geometrical acceptance, and uncertainties in the extraction of the cross section, the spectator energy range $8 \leq T_{\text{sp}} \leq 22$ MeV has not been further considered in the analysis of the $pn \rightarrow d\omega$ data.

Chapter 6

Luminosity Determination

In order to be able to scale the spectra between different beam energies and extract an ω cross section, the absolute luminosity has been determined for each run. For this purpose proton-deuteron elastic scattering, tagged by a recoil deuteron with 17 to 18 MeV kinetic energy in the silicon telescope, has been chosen. The reasons for this choice and the experimental implications in terms of acceptance and systematic uncertainties will be discussed in this chapter. The most prominent uncertainty arises from the fact that only a fraction of the target could be used for the analysis of $pd \rightarrow pd$, due to geometrical restrictions in the existing target chamber. Thus the shape of the beam-target overlap plays an important role. The silicon telescope has been used parasitically to obtain the target density distribution, which was found to vary significantly with time. Nevertheless, a method to correct for the changes could be found, leading to an absolute cross section normalisation with a total systematic uncertainty of 15% [70]. Calculations of the differential cross section of $pd \rightarrow pd$ at our energies have been performed within the Glauber model [71]. Such estimates agree with the available experimental data at 2.78 GeV/c [72] within the quoted error of about 10%. Hence, the luminosity could be calculated for each run individually with an absolute systematic error of 20%.

6.1 Normalisation Concept

Count rates resulting from the combination of several stop counters of the telescopes installed at ANKE provide a means to monitor the interaction rates during an experiment. These can be used for relative normalisation at ANKE. However, this method does not enable us to make comparisons if experimental conditions – such as beam momentum and geometrical settings – change. In order to compare spectra obtained below and above the threshold for ω -production and to extract cross sections, it is finally necessary to normalise the data absolutely. Now the cross section is the rate dN/dt of a reaction taking place divided by the luminosity L . Consider now N_{exp} to be the number of reactions experimentally identified, ϵ_{eff} the efficiency and ϵ_{acc} the acceptance for this measurement, then

$$\sigma := \frac{1}{L} \frac{dN}{dt} = \frac{1}{L \epsilon_{\text{eff}} \epsilon_{\text{acc}}} \frac{dN_{\text{exp}}}{dt} \quad (6.1)$$

is the experimentally accessible cross section for this reaction. For the determination of the values ϵ_{eff} and ϵ_{acc} in $pn \rightarrow d\omega$, please refer to Chaps. 5 and 7. The luminosity L is an observable, which is defined by the intensity of the beam and the overlap with the target at a mean area density of ρ_A :

$$L := \frac{dN_{\text{beam}}}{dt} \rho_A = N_{\text{beam}} \nu \rho_A \quad (6.2)$$

At a storage ring this can be expressed in terms of the number of circulating particles in the ring N_{beam} and their revolution frequency ν . However, the value of ρ_A cannot be determined very accurately. Thus it is more convenient to invert Eq. 6.1 and determine the luminosity via the measurement of a reaction with well known cross section. As mentioned before, typically only a fraction of the reactions can be identified in the detection system. Consider $\Delta\sigma = \int_{\text{acc}} \frac{d\sigma}{d\Omega} d\Omega$ to be the integrated differential cross section in the acceptance of the system and ϵ_{eff} the average efficiency of the detection¹, then the luminosity can be expressed as:

$$L = \frac{1}{\Delta\sigma \epsilon_{\text{eff}}} \frac{dN_{\text{exp}}}{dt}. \quad (6.3)$$

Having obtained this value from any known reaction, another process can be normalised using Eq. 6.1. In quasi-free pn reactions the Fermi momentum allows us to select a certain range in centre-of-mass energy. This, however, reduces the available luminosity correspondingly in addition to the shadowing effect discussed in Sec. 1.2. The principle will be presented in the end of this Chapter, whereas the description how this factor, convoluted with the acceptance, can be extracted from phase-space simulations will follow in the next Chapter.

In the following it will be shown why pd -elastic scattering is a suitable reaction to determine the absolute luminosity. Furthermore, the selections to obtain N_{exp} are listed and the method to extract $\Delta\sigma$ at our experiment from differential cross sections and acceptance considerations is discussed. Finally some experimental correction factors (which can be ascribed to the detection efficiency ϵ_{eff}) are applied to obtain integral luminosities for each run.

6.2 Selection of pd Elastic Scattering

The silicon telescope allows one to trace deuterons with kinetic energies above 8.5 MeV originating from the target at angles larger than 80° . Purely kinematical arguments show that these particles can only stem from pd -elastic scattering. Thus the identification and energy determination of a deuteron in this range is sufficient to tag the reaction. Moreover, the corresponding protons for this range are fully covered by the acceptance of the forward hodoscope and are therefore triggered with the same coincidence trigger as the $pn \rightarrow d\omega$ candidates. This reduces systematic uncertainties for the normalisation (see Sec. 5.2). Nevertheless, to minimise uncertainties, the following two selections have been made in the silicon-telescope:

- Deuterons were restricted to an energy range of $17 \leq T_{\text{kin}} \leq 18$ MeV leading to:

¹In general the efficiency ϵ_{eff} should also be integrated over $d\Omega$ but we will see later that for the consideration on luminosity the efficiency can be assumed to be homogeneous.

- 100% acceptance of coincident protons in the forward hodoscope in order to be able to use the same trigger as for the experiment,
 - angular straggling below 2° in σ and thus low uncertainty for the last layer acceptance (see Sec. 6.4.2),
 - small acceptance corrections from the resistor chain read-out gaps, as these gaps decrease with deposited energy in the detector (see Sec. 5.2),
 - a maximised visible part of the target (to be discussed in Sec. 6.4.3),
 - and a count rate, where statistical errors for each run are small in comparison to systematic uncertainties.
- The central area of the second layer (strips 7 to 32) was selected to:
 - reduce background from rescattered particles in the frame of the first layer surface barrier detector,
 - and to further decrease the uncertainty for the last layer acceptance (see also Sec. 6.4.2).

The total number N_d of events fulfilling these criteria has been recorded for each run and will be used to determine the integrated luminosity as in Eq. 6.6 on page 62.

6.3 *pd* Elastic Cross Section

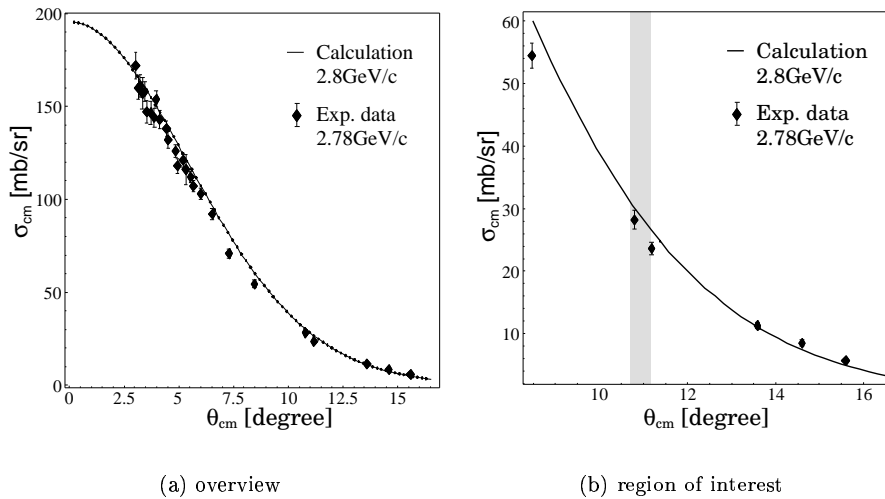


Figure 6.1: Experimental differential cross section at 2.78 GeV/c [72] and calculations at 2.8 GeV/c [71] *versus* the polar angle in the centre-of-mass system. Shaded is the range used for the normalisation.

For the beam momenta used at the experiment, 2.6, 2.7, 2.807 and 2.9 GeV/c, Yu. Uzikov [71] calculated the dependence on the polar angle of the proton emitted at small angles. The calculated behaviour at 2.807 GeV/c is shown as the solid line in Fig. 6.1 in the centre-of-mass system. The differential cross section has been measured at a beam momentum of 2.78 GeV/c [72], which is in the middle of the momentum range used for the ω -experiment at ANKE. These experimental values are plotted for comparison in Fig. 6.1. The selected range ($17 \leq T_d \leq 18$ MeV) for the detected deuterons translates into the ranges of centre-of-mass angles for protons listed in Table 6.1 and is indicated for 2.807 GeV/c as shaded area in Fig. 6.1(b).

$p_{\text{beam}}^{\text{lab}}$ [GeV/c]	θ_p^{cm} [°]	$(d\sigma/d\Omega)^{\text{cm}}$ [mb/sr]
2.600	11.42 to 11.75	25.8 to 23.1
2.700	11.13 to 11.45	27.0 to 24.2
2.807	10.84 to 11.16	28.2 to 25.2
2.900	10.60 to 10.90	28.6 to 25.6

Table 6.1: Proton range corresponding to the selected deuterons with $17 \leq T_d^{\text{lab}} \leq 18$ MeV and differential cross section for the beam momenta in August 2001.

In order to obtain the luminosity from Eq. 6.3, the differential cross section has to be integrated over the experimental acceptance, which has been approximated as follows:

$$\Delta\sigma_{pd} = \int_{\text{acc}} \frac{d\sigma_{pd}}{d\Omega} d\Omega \approx \langle (d\sigma_{pd}/d\Omega)^{\text{cm}} \rangle [\cos(\theta_p^{\text{cm}})]_{\theta_{\text{min}}}^{\theta_{\text{max}}} \Delta\phi \epsilon_{\text{acc}} \quad (6.4)$$

The mean differential cross section $\langle (d\sigma_{pd}/d\Omega)^{\text{cm}} \rangle$ has been determined taking the arithmetical average from the calculated values in Table 6.1. Similarly, the polar angles θ_{min} and θ_{max} are identified with the angles corresponding to 17 and 18 MeV protons shown in the same table. The azimuthal angular range $\Delta\phi$ and further acceptance factors gathered in the value ϵ_{acc} will be discussed in the next sections. From these considerations it will also become clear, why these factors can be treated independently of the integration in Eq. 6.4.

To estimate the systematic error of this method the following contributions have been considered. The overall uncertainty of the calculation of the differential cross section is stated to be 10% [71]. Note, that the systematic error of the experimental points in Fig. 6.1 is claimed to be 7% [72]. Two additional uncertainties arise from the determination of the deuteron energy. From Table 6.1 one obtains the differential relation of this energy T_d^{lab} to the differential cross section $(d\sigma_{pd}/d\Omega)^{\text{cm}}$:

$$\frac{\Delta (d\sigma_{pd}/d\Omega)^{\text{cm}}}{\Delta T_d^{\text{lab}}} \approx \frac{11\%}{\text{MeV}} (d\sigma_{pd}/d\Omega)^{\text{cm}} \quad (6.5)$$

The first error corresponds to the uncertainty of the mean cross section arising from the systematic uncertainty of 1% in the determination of T_d . This translates into a 2% error in the mean cross section. Additionally the error in the event by event determination of the kinetic energy leads to a systematic

uncertainty. This is due to the fact that the cross section is not constant. Thus events gained from the higher σ -side by statistical fluctuations outnumber the events lost due to the same reasons on the lower σ -side. To account for that a systematic error of 1.5% has been introduced.

6.4 Acceptance Determination

The acceptance is already strongly restricted by the selection of the deuteron energy; the deuterons fall within a cone with a polar angle of $83.12^\circ \pm 0.10^\circ$. At the location of the telescope, the smearing of this cone due to the angular resolution ($\leq 2^\circ$ i.e. ≤ 2 mm in the last detector) is still small in comparison to the effect coming from the finite target extension. Hence, let us separate the considerations in two tasks:

- the determination of the angular acceptance for a point of the target which is in the visible region of the target,
- and the extrapolation of the visible fraction of the target to the whole density distribution of the beam-target overlap.

In order to obtain this, the target dimensions and its position relative to the detectors have first to be determined, and only thereafter the two items will be discussed.

6.4.1 Target Geometry

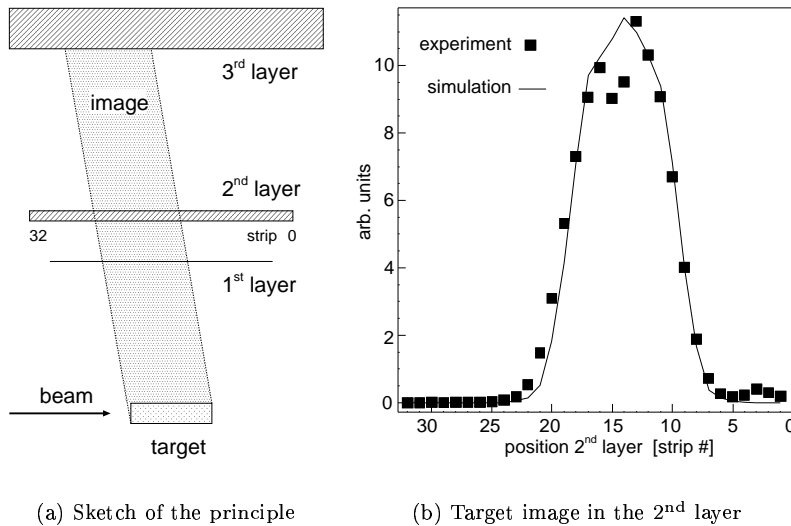


Figure 6.2: The target is projected onto a plane in the telescope by the selection of a fixed angle. The image (squares) is compared with the distribution from Monte Carlo simulations (line) [62] assuming a rectangular shaped target with a length of 9.5 mm.

A measurement of the target position and dimensions was performed by the Münster group [73] after the installation of the target in September 2000. Rods which were inserted about 25cm above and below the beam overlap region were moved while monitoring the vacuum conditions in the region just below the target. From the obtained vacuum changes, the target sizes were estimated by linear interpolation or extrapolation to the nozzle. Unfortunately this measurement could only be done at target densities which are orders of magnitude lower than the ones used in the experiment. The results are listed in Table 6.2 in comparison with those obtained from the analysis described in the following. All values except the width ΔX can also be obtained directly from the experimental data using the silicon telescope, and thus under the conditions during the measurements. The kinematic relations in pd -elastic scattering provided accurately the relative positions of the second and third layer.

An effective tool to study the geometry is the production of so-called target images in the detectors. One selects identified protons with low angular straggling ($T_{\text{kin}} \geq 16$ MeV) and fixed reconstructed angle. This is schematically sketched in Fig. 6.2(a). The resulting distribution in the second detector plane is shown in Fig. 6.2(b). The latter is simply the projection of the beam target overlap along the given angle, folded by a contribution from angular straggling. This is due to the fact that, no matter which reactions contribute, their cross section for a fixed angle does not depend upon the interaction point.

The dip around strip 15 in Fig. 6.2(b) can be explained by a known acceptance gap due to the resistor chain read-out². The acceptance loss is determined to be 10 to 15%. Though it will be discussed later, note already here that significant changes in these images have been observed not only in position but also in shape. The following tasks have been addressed by the use of such images:

- The relative luminosity has been monitored just by the count rate within this distribution. This has been cross-checked with other relative luminosity monitors, such as a coincidence rate of the stop counters in the telescopes and the bare forward trigger rate (see Fig. C.1). Their ratios are stable within a few per cent for all runs finally analysed.
- The density distribution of the beam target overlap has been monitored along the beam axis (Z) by selecting angles as close to 90° as possible. A range of 93.5° to 95.5° was chosen³ such that the effect from straggling in the frame of the first layer detector could be neglected. Monte Carlo simulations [62] show that a target with 9.5 mm length and a rectangular shape reproduces the observed image integrated over the whole beam time very well (see Fig. 6.2(b)).
- As will be shown later, the density distribution and its variations can be used to extract, not only a single correction factor for the absolute luminosity determination, but also a correction for the distribution run by run. Furthermore, the method even allows us to find the cut level from the data, not having to rely on geometry.

²The correspondence of this effect to the gap from the resistor chain was verified by changing the angular range.

³This corresponds to a change in Z of 0.3 mm within the target region from the ideal perpendicular cut.

- The mean position of the beam-target overlap perpendicular to the beam in the horizontal plane (X) can be determined from the variation of the selected angular range. The dependence of the middle of the images on the X-coordinate has been studied using Monte Carlo simulations [62] and the experimentally obtained values. A shift of the overlap region to the outer side of the ring by 4.7 mm has been found consistently for all beam momenta.

	X [mm]	ΔX [mm]	Z [mm]	ΔZ [mm]
Münster [73]	2.4 ± 1	4.9^{+1}_{-0}	-1.0 ± 1	12^{+0}_{-1}
telescope	4.7 ± 1.0	—	-0.8 ± 0.5	9.5 ± 0.5

Table 6.2: Target geometry determined by the Münster group [73] and the analysis performed with the silicon telescope described in this chapter.

Our results, labelled by “telescope”, are compared with the specifications given by the Münster group in Table 6.2. Significant deviations are found for the horizontal coordinate X and the length of the target along the beam ΔZ . These might be explained by the fact that the values are based on measurements under quite different conditions. The latter measurements were done simultaneously with the experimental data used for the ω analysis. Thus the values reflect the experimental conditions rather than a determination done a year before at orders of magnitude lower target densities. It is for this reason that the telescope values are used in the further analysis.

6.4.2 Transverse Slice of the Target

Consider an infinitesimally thin slice perpendicular to the beam axis. From the choice of deuterons with $17 \leq T_d \leq 18$ MeV a cone with an opening angle of 83.02 to 83.22° is selected. Due to the transverse width of the target (ΔX), a length of 0.6 mm (ΔZ) is scanned. Together with the opening angle, the arc of the cone has a spread of about 1 mm in the last layer neglecting straggling. The contribution to the acceptance from the angular straggling and the restriction in azimuth are the effects considered to be significant for the analysis:

- The angular straggling in the first two layers of the detector alter the acceptance of the third layer. For the azimuthal angle this has no quantitative effect, as the number of particles scattered out of the acceptance is roughly the same as the amount scattered into the acceptance. Furthermore, this effect is included in the Monte Carlo simulations [62]. However, for the polar angle⁴ the angular straggling in the second layer of the silicon telescope will scatter particles out of the acceptance of the third layer, but not into it. This effect can be illustrated in the distribution of the last layer, selecting a single strip in the second layer additionally to the narrow energy interval already selected. Consequently the initial scattering angle is fixed to be 83° and the width of the distribution in the last layer is dominantly determined by angular straggling. This distribution

⁴The acceptance for the selected energy range has been included by the “ $\cos \theta$ ”-term in Eq. 6.4 already.

is presented in Fig. 6.3 for the two strips closest to the counter border (number 7 and 8). From the distributions of the strips used (number 7 and higher numbers) the loss due to scattering out of the acceptance can easily be estimated to be $(10 \pm 2)\%$.

- A restricted angular range in azimuth is accepted from the cone in the telescope. Both geometrical considerations and Monte Carlo simulations [62] lead to an angular range of $\Delta\phi \approx 12^\circ$ accepted in the telescope. This is of course the same for the laboratory as for the centre-of-mass system and can thus be used directly in Eq. 6.4. The largest uncertainty is due to that in the distance of the beam-target overlap region to the detectors. The sensitivity to such a shift is 0.8% per 1 mm transverse beam shift. The previous analysis shows that a deviation by more than 1 mm is unlikely and thus the uncertainty for the acceptance calculation is below 1%.

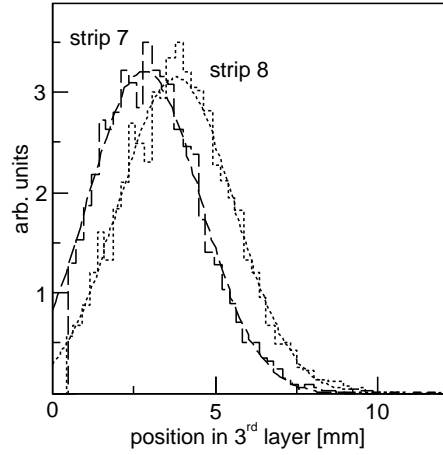


Figure 6.3: Spatial distribution in the 3rd layer for the strips number 7 and 8 in the 2nd layer and deuterons with $17 \leq T_d \leq 18$ MeV selected.

6.4.3 Fraction Observed Along the Beam

A large correction factor arises from the fact that, for geometrical reasons, only part of the target can be observed by this method. (It will be denoted by ϵ_{tg} in the following.) This restriction is only related to the limited space inside the target chamber and will be overcome already for the next experiment in August 2003 with the chamber installed in December 2002. However, for the described experiment the observed fraction of the target had to be determined, thus imposing an additional significant uncertainty to the normalisation. Moreover, the density distribution of the target is *a priori* not known and – as the following analysis shows – even changes with time. Thus, from the simultaneous monitoring of the target image presented in Sec. 6.4.1, the fraction of the target observed with $pd \rightarrow pd$ run by run has been derived.

A first indication that the fraction of the target seen indeed varies was found in the comparison with relative luminosity monitors. Even though the ratios of

the relative monitors to each other are stable within a few per cent, the ratio of the counts in the target image to the pd -elastic events revealed changes by factors of up to 3. The clear correlation of this ratio to the average position determined by the target image confirms this assumption (see Fig.6.4).

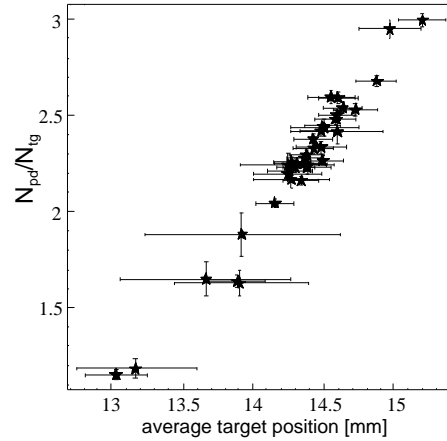
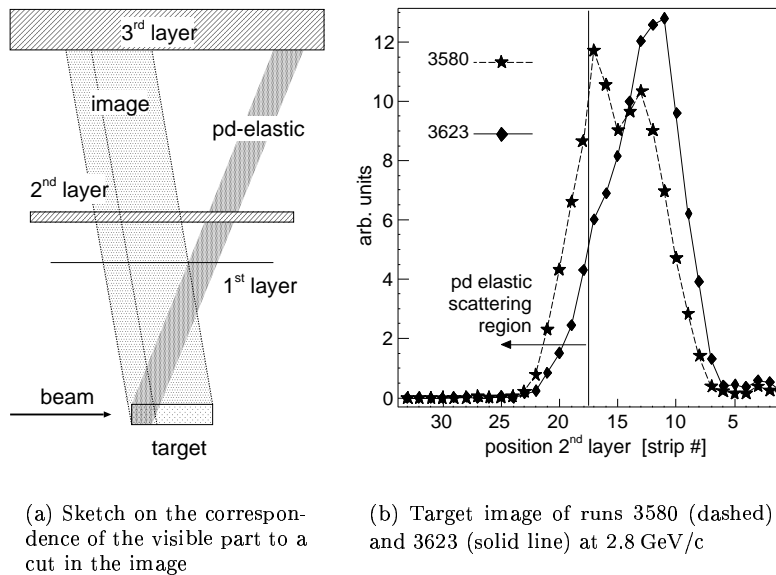


Figure 6.4: Ratio of events recorded at 2.8 GeV/c by pd -elastic N_{pd} and counts inside the target image N_{tg} versus the average target position



(a) Sketch on the correspondence of the visible part to a cut in the image

(b) Target image of runs 3580 (dashed) and 3623 (solid line) at 2.8 GeV/c

Figure 6.5: Within the changing target image the part visible for absolute normalisation can be determined with a fixed cut level. This region is the one to the left of the vertical line in (b)

The observed correlation can be understood from Fig. 6.5(a). Despite a shift of the target image along the detector, which reflects a change of the target density along the beam direction, the elastically scattered deuterons can only be detected being emitted from the same space volume. The boundary of the volume is determined by the the edge of 7th strip in the second layer and the selected energy (i.e., angular) range and can be considered as a cut on the target image. Note, that the position of the cut is the same for all runs at one beam energy and changes only very slightly for different beam energies. Moreover, the proximity to 90° of both the tracks from $pd \rightarrow pd$ ($83^\circ \pm 0.2^\circ$) and from the target image ($94.5^\circ \pm 1.0^\circ$) allows us to translate the cut on the deuterons to a cut in the target image (see Fig. 6.5(a)). Once the position of the cut in the second layer of the detector is fixed, one can correct for the fraction of the target observed by the elastic reaction run by run. Comparing the corrected numbers with other relative monitors, such as the combination of stop counters in the telescopes, their ratios are constant within $\pm 5\%$.⁵

Runs with extreme shifts of the target have been used to calibrate the cut level from the obtained data. As an example, the target images of two runs at 2.8 GeV/c are shown in Fig. 6.5(b). For the two selected runs the change in the ratio of the absolute to relative luminosity monitor should correspond to the change in the fraction of the target seen. Varying the cut level for both runs simultaneously in the target image until the ratio of the target fractions coincides with the ratio of luminosity monitors defines the cut level indicated in Fig. 6.5(b) by a vertical line.

This procedure has been repeated with several sets of runs and the maximum deviation found was 0.3 mm. This translates into a change of the visible fraction of the target or luminosity of about 15%, which should be considered as the best estimate for the systematic error. Note that the average fraction of the target seen is about 20%, but the correction factor ϵ_{tg} was determined individually for each run by the previously mentioned method.

6.5 Luminosity in August 2001

From Eq. 6.3 the integrated luminosity during a certain measurement period is:

$$\int L dt = \int \frac{1}{\Delta\sigma_{pd} \epsilon_{\text{eff}}} \frac{dN_{\text{exp}}}{dt} dt \quad (6.6)$$

Neither the accepted part of the cross section $\Delta\sigma_{pd}$ nor the experimental efficiency ϵ_{eff} can be treated as constant over the whole beam time. A sensible division, due to statistics, seems the one by runs. Moreover, several variables are constant within one beam setting, i.e. beam energy. Let us try to separate those contributions. The efficiency has been factorised as $\epsilon_{\text{eff}} = \epsilon_{\text{si}} (f_{\text{dt}} f_{\text{mult}})$, where ϵ_{si} is the contribution from the charge collection in silicon and has been neglected, due to the cancellation for the normalisation (see discussion in Sec. 5.2). The factors due to the dead time of the system f_{dt} (see Sec. 5.1) and the multiplicity of the hits in the telescopes $f_{\text{mult}} = f_{\text{m2}} f_{\text{m3}}$ (see Sec. 3.2) are taken into account run by run. $\Delta\sigma_{pd}$ is also taken to be constant except for the acceptance correction due to the fraction of the target observed ϵ_{tg} . Recalling Eq. 6.4, one can write $\Delta\sigma_{pd} = \Delta\sigma_{\text{const}} \epsilon_{\text{tg}}$ with:

⁵The few runs deviating from this have been dropped from the analysis.

$$\Delta\sigma_{\text{const}} \approx \langle (d\sigma_{pd}/d\Omega)^{\text{cm}} \rangle [\cos(\theta_p^{\text{cm}})]_{\theta_{\text{min}}}^{\theta_{\text{max}}} \Delta\phi \quad (6.7)$$

The integrated luminosity can now be calculated for the four sets of runs corresponding to the four beam momenta as follows:

$$\int L dt \approx \frac{1}{\Delta\sigma_{\text{const}}} \sum_{\text{runs}} \frac{N_d f_{m2} f_{m3} f_{dt}}{\epsilon_{\text{tg}}} \quad (6.8)$$

In Table C.1 on page 99 the correction factors and luminosities obtained are listed run by run. From Eq. 6.8 it is clear, that these can be used to obtain integrated luminosities for a set of runs simply by adding the run by run values. The results are shown in Table 6.3 together with the constant part of the fraction of the total cross section in the acceptance. Nevertheless, to normalise the data from any other reaction one has to take the non-constant factors in Eq. 6.1 into account run by run. This will be done in the next section to scale the results from simulations in $pn \rightarrow dX$, where X are either several pions or an ω meson.

p_{beam}	$\Delta\sigma_{\text{const}}$ [μb]	integrated luminosity [1/nb]	
		total collected	analysed for $pn \rightarrow d\omega$
2.6 GeV/c	5.10	0.931	0.171
2.7 GeV/c	5.07	0.490	0.384
2.8 GeV/c	5.01	0.974	0.581
2.9 GeV/c	4.88	0.486	0.445

Table 6.3: Overview over the total statistics collected and finally used for the data analysis in terms of integrated luminosity

All the systematic errors have been discussed in the corresponding sections. They are summarised here in order to compute an overall uncertainty of the method. The errors considered are:

- 10% due to the calculation of the $pd \rightarrow pd$ cross section [71],
- 2 and 1.5% arising from the uncertainty in the deuteron energy,
- 1% from the azimuthal acceptance,
- 2% from angular straggling in the second layer,
- 15% due to the correction for the fraction of the target seen.

As these errors are uncorrelated, we add them quadratically even though they are not statistical fluctuations. The result is that the luminosity can be determined within a systematic uncertainty of about 20%. Note that the error for the relative normalisation between different beam momenta will be considerably smaller.

6.6 Cross-Check by Other Methods

During run 3687 in August 2001 a measurement of the change in the revolution frequency has been performed with a coasting beam [74]. This observable can be determined very accurately by the analysis of the longitudinal Schottky signal with a fast Fourier transformer [75]. This frequency change is a measure of the energy loss of the proton beam due to the target interaction [74]. The determined luminosity is presented in Table 6.4 and compared to the value obtained by the previously discussed method. Both results agree well within the systematic errors.

run	luminosity [$10^{30} \text{ cm}^{-2} \text{ s}^{-1}$]	
	silicon telescope (1)	cross-check
3687	$8.1 \pm 0.4_{\text{stat}} \pm 1.7_{\text{sys}}$	7.0 ± 1.0 (2)
3407	$0.24 \pm 0.03_{\text{stat}} \pm 0.05_{\text{sys}}$	$0.297 \pm 0.012 \pm 7\%$
3408	$0.36 \pm 0.03_{\text{stat}} \pm 0.07_{\text{sys}}$	$0.432 \pm 0.018 \pm 7\%$
3409	$0.34 \pm 0.03_{\text{stat}} \pm 0.07_{\text{sys}}$	$0.360 \pm 0.014 \pm 7\%$ (3)
3410	$0.71 \pm 0.05_{\text{stat}} \pm 0.14_{\text{sys}}$	$0.700 \pm 0.029 \pm 7\%$
3411	$1.14 \pm 0.07_{\text{stat}} \pm 0.22_{\text{sys}}$	$1.212 \pm 0.052 \pm 7\%$

Table 6.4: Comparison of luminosities calculated using three approaches. By the: (1) information from the silicon telescope as presented in this chapter (middle column); (2) p -beam frequency shift (cross check for run 3687) [74]; (3) diffractive pd -scattering (5 lower rows in the right column) [71, 76].

Another cross check could be done at a beam time in February 2001 [64]. Measurements under quite similar conditions – i.e. deuterium cluster target, unpolarised proton beam – have been performed at a maximum beam momentum of $2.679 \text{ GeV}/c$ ($T = 1.9 \text{ GeV}$)⁶. The use of the forward trigger alone enables us to determine the luminosity in two ways. The results from the method discussed previously shown in the middle column of Table 6.4 [70] can be compared with results using the detection of fast protons in the forward detectors and calculations from diffractive pd -scattering [76] in the right column⁷. Note, that this is a rather independent method as it includes deuteron dissociation processes with small momentum transfer, whereas the use of the silicon telescope restricts the reactions to high momentum transfer. Also here the values agree within errors⁸. Thus one can conclude that the method presented in this chapter is indeed suitable to determine the luminosity within 20% systematics.

6.7 Luminosity in the pn System

Studying pn collisions in the spectator model we have to deal with neutrons moving with respect to the laboratory system. The luminosity integrated over

⁶The aim of the beam time was to study break-up reactions with small relative momenta from two nucleons.

⁷The first errors include systematic as well as statistical errors and the 7% is the given systematic error due to the cross section calculation [71].

⁸Note, however, that the systematics from the model calculations on the cross section are partially redundant, as the predictions were obtained with the same model [71]

the Fermi distribution of these neutrons can be obtained by decreasing the collective luminosity by 5% to account for the shadowing [31] (see Sec. 1.2). However, the acceptance of the silicon telescope for the spectator detection restricts the range of the neutron momenta such, that a range in centre-of-mass energy

$$\sqrt{s_{pn}} = \sqrt{(p_{\text{beam}}^\mu + p_{\text{target}}^\mu - p_{\text{sp}}^\mu)^2} \quad (6.9)$$

is covered. Here p_{beam}^μ , p_{target}^μ and p_{sp}^μ are the four-momenta the beam proton, target deuteron and spectator proton respectively. (Refer to Sec. A.1 for a more detailed discussion on kinematics.) Experimentally we would like to know the luminosity within this range in order to normalise our data.

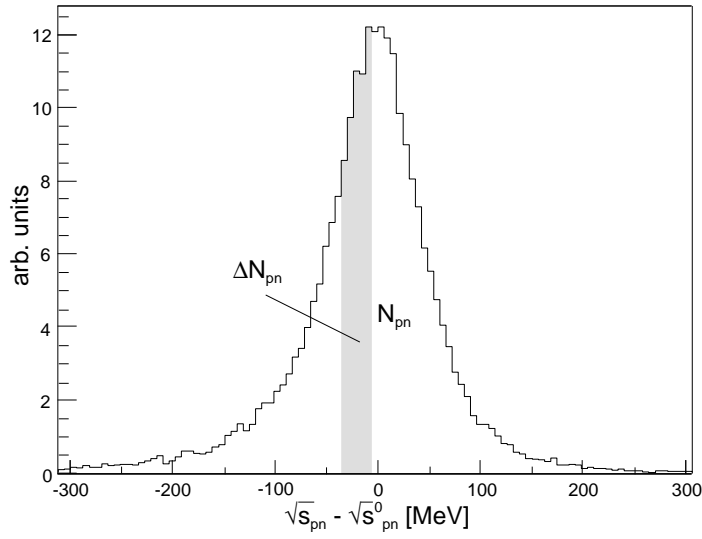


Figure 6.6: Centre-of-mass energy distribution in pn reactions at a fixed proton beam momentum and a stationary deuteron as target. The shaded area shows the part of the distribution covered by the acceptance for spectator detection.

To illustrate the situation let us consider e.g. the situation in Fig. 6.6. The centre-of-mass energy in the pn system $\sqrt{s_{pn}}$ is spread around the value for a stationary neutron $\sqrt{s_{pn}^0}$. The total number of entries N_{pn} under this distribution defines the luminosity for pn reactions, which can be computed from the coherent pd luminosity. Selecting now a certain $\sqrt{s_{pn}}$ bin (shaded area in Fig. 6.6), corresponding to ΔN_{pn} events, the fraction

$$f_L := \frac{\Delta L}{L} = \frac{1}{L} \int_{\text{bin}} \frac{dL(s)}{ds} ds = \frac{\Delta N_{pn}}{N_{pn}}, \quad (6.10)$$

will determine the part of the luminosity ΔL provided in this bin. This factor can be obtained for any arbitrary bin. Hence we can select the range of our acceptance and determine the effective luminosity for our pn reaction in this $\sqrt{s_{pn}}$ range.

Chapter 7

Experimental Results

As shown in Sec. 3 and 4, the kinematics and identity of the spectator proton and fast deuteron can be determined in the silicon telescope and the forward detection system respectively. Acceptance calculations, using phase-space simulations, together with the determined luminosity provide the factors for an absolute normalisation of the quasi-free pn reactions in a certain centre-of-mass energy range. The missing-mass method has been used for the identification of the ω -meson. The reconstruction of the neutron and $\Delta^0(1232)$ in the $pn \rightarrow pX$ channels show the feasibility of this approach.

Experience with ω production in proton-proton collisions shows there to be considerable multi-pion production under the ω peak [47]. This can be estimated by comparing the data above and below the ω threshold. In result total cross sections averaged in two excess-energy ranges around $Q = 26$ and 60 MeV were obtained. We can conclude that the situation in the ω case differs significantly from η production and all published model predictions.

7.1 Acceptance Determination

It is the goal of this work to extract cross sections for $pn \rightarrow d\omega$ at defined Q values. However the measurements were done for the reaction $pd \rightarrow p_{sp}d\omega$ at fixed beam energies. The translation is done on the event-by-event basis using the measured spectator momentum and Eq. 6.9. The ranges of \sqrt{s}_{pn} are determined by the spectator detection alone. The experimental excess energies $Q = \sqrt{s}_{pn} - m_d - m_\omega$ in the reaction $pn \rightarrow d\omega$ are calculated with respect to the nominal ω mass value $782.6 \text{ MeV}/c^2$. In Fig. 7.1 the obtained distributions are shown.¹ The mean values $\langle Q \rangle$ are deduced from these distributions and are taken together with the full-width-half-maximum as labels for the excess energy ranges. Here $Q = (26 \pm 18) \text{ MeV}$ and $Q = (60 \pm 18) \text{ MeV}$ are obtained for the beam momenta $2.8 \text{ GeV}/c$ and $2.9 \text{ GeV}/c$ respectively. Note that both ranges start well above the threshold for ω production ($\geq 10 \text{ MeV}$) compared to the ω width $\Gamma_\omega = 8.4 \text{ MeV}$. From simulations it was found, that the mean Q

¹Due to the limited statistics for $pn \rightarrow d\omega$ the distributions include all background channels. Nevertheless, it could be shown by simulations, that their shape does not differ significantly from the case of ω production.

value due to our acceptance and cross section dependence differs only slightly from the arithmetical mean values 26 and 60 MeV.

For the acceptance determination the same restrictions as in the experimental analysis are applied. All particles have to pass the geometrical boundaries of the detectors and to fulfil the experimental selection criteria, which were applied in the analysis. In our case a spectator proton with $2.6 \leq T_{sp} \leq 4.4$ MeV is required in the silicon telescope in coincidence with a deuteron in the forward acceptance. The latter condition implies the passage through valid cells in all four planes of the chambers (see Chap. 5), both layers of the hodoscope (excluding the first counters in both layers) and finally the lower Čerenkov counters (number 1 to 5).

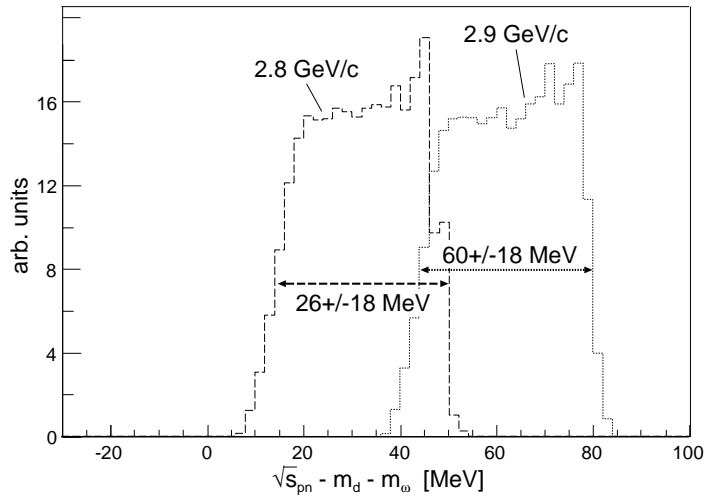


Figure 7.1: Experimental excess energy in $pn \rightarrow d\omega$ with $m_\omega = 782.6 \text{ MeV}/c^2$ in selected $pd \rightarrow p_{sp}dX$ events with $2.6 < T_{sp} < 4.4$ MeV at 2.8 and 2.9 GeV/c beam momentum (dashed and dotted lines respectively).

In the cross section measurement of $pn \rightarrow d\omega$, the range in Q covered was summed over, due to the restricted statistics obtained. Thus the acceptance in the same range has to be determined for the normalisation. Of course, this range has to be identical to the $\sqrt{s_{pn}}$ range chosen to determine the fraction of luminosity used (see Sec. 6.7). It can be shown, however, that both the determination of the acceptance ϵ_{acc} and the luminosity fraction f_L can be done in a single step, making considerations on the exact range to be chosen irrelevant. To illustrate this, consider the situation where N_{acc} events were accepted from N_ω events. Then $\epsilon_{acc} = N_{acc}/N_\omega$ is the acceptance for the reaction which is defined for the Q range covered. Recalling now Eq. 6.10, the fraction of luminosity $f_L = \Delta N_{pn}/N_{pn}$ has to be determined within the same range. Here the transformation from $\sqrt{s_{pn}}$ to Q enters. This is, however, not a source of systematic uncertainty as the $\sqrt{s_{pn}}$ distribution in Fig. 6.6 can be smeared with the ω mass and the fraction f_L can be extracted in the same way as in $\sqrt{s_{pn}}$. However if we normalise both equations with $f_n = \Delta N_{pn}/N_\omega$, the

convolution of both factors contributing to the normalisation is just

$$f_L \epsilon_{\text{acc}} = \frac{\Delta N_{pn}}{N_{pn}} \frac{N_{\text{acc}}}{N_{\omega}} = f_n \frac{N_{\text{acc}}}{N_{pn}}. \quad (7.1)$$

As we will see in the following, this combined normalisation factor can be easily extracted from phase-space simulations.

To simulate the $pd \rightarrow p_{\text{sp}}dX$ reactions, where X are either several pions or the ω meson, the PLUTO event generator [77] has been used. This employs the Hamada-Johnston wave function [78] to smear over the Fermi motion in the deuteron. From Fig. 7.2 it becomes clear that the results from this function are virtually indistinguishable from more realistic wave functions at these small values of spectator momenta. The generated events were traced through ANKE using an implementation of the set-up in the program GEANT3 [62].

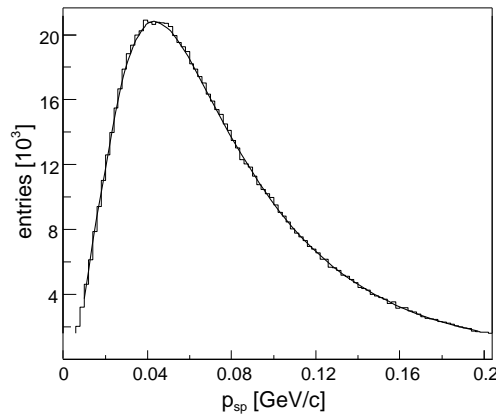


Figure 7.2: Comparison of the momentum distribution of spectator protons from the PLUTO event generator [77] (histogram) with results from the Paris wave function [79] (curve). Within the momentum range of interest no difference is observed.

The events were generated by taking a constant cross section above threshold. Thus the initial distribution from Fig. 6.6 will be reproduced above the ω threshold and the pn events ΔN_{pn} in our range will be automatically equal to the generated $pn \rightarrow d\omega$ events N_{ω} . The factor f_n in Eq. 7.1 is then equal to 1 and, by counting additionally the events which were rejected due to a negative Q , the total number of entries in the pn distribution N_{pn} is obtained. This can be used as a normalisation factor under the condition that the Q range has to be small enough for the cross section not to change too strongly. However this condition may be dropped, if the acceptance within this range is fairly constant. Both requirements may, *a priori*, not be true. In order to estimate the error induced by taking the cross section to be constant over the Q bin, simulations assuming a constant matrix element (i.e. the cross section developing according to phase space) have been performed. The resulting difference in acceptance is small (5% and 1% for 2.8 and 2.9 GeV/c respectively [70]). Furthermore, the change in the mean Q value by 1 – 2 MeV is negligible in comparison to the

bin size of 36 MeV. Thus we conclude, that the uncertainty for the cross section measurements due to this method can be neglected.

The restricted angular acceptance for the $pd \rightarrow p_{sp}d\omega$ reaction is another source of systematic uncertainty becoming more serious with increasing Q . This is due to the fact that, because of the restriction of the deuteron angles, not all of the total phase-space is covered at the high excess energies. In Fig. 7.3 the deuteron angular distribution in the centre-of-mass system for S -wave production is shown in the ANKE acceptance at both energies above threshold. Although at our energies we might expect S -wave production to dominate, pure P -wave angular dependencies of $\cos^2\theta$ or $\sin^2\theta$ would change the estimate of the acceptance by factors of 1.33 and 0.83 respectively for 2.8 GeV/c. At our highest energy point the variation is between 1.7 and 0.65. These are, however, extreme scenarios and half of the deviations are taken as conservative estimates of the errors. Values of (-9%, +17%) and (-17%, +35%) are concluded for the ranges around 26 and 60 MeV respectively.

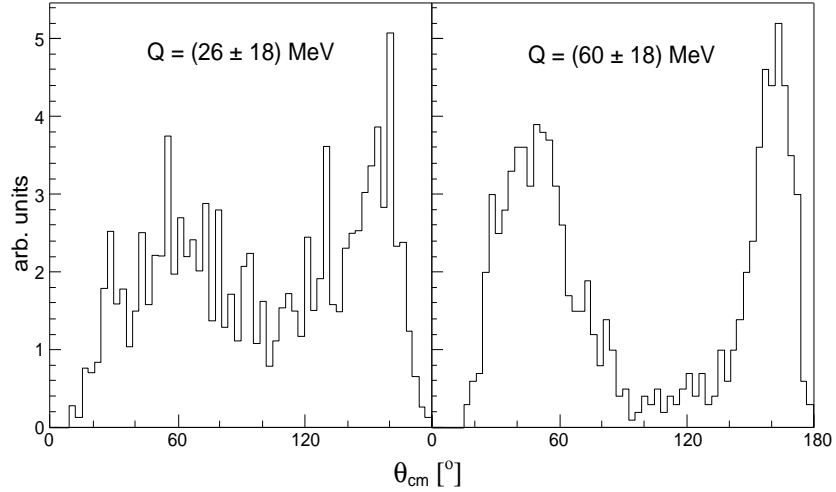


Figure 7.3: Distribution of the $d\omega$ polar angle in the cm system for the reaction $pd \rightarrow p_{sp}d\omega$ at 2.8 and 2.9 GeV/c (left and right distribution respectively): The acceptance of the set-up restricts the covered phase-space significantly at the highest energy. Note however, that the acceptance corrected distributions have to be symmetric around 90° .

7.2 Missing-Mass Distributions

Equation 7.2 illustrates how the quantity m_X is determined in the measured reaction $pd \rightarrow p_{sp}AX$, where A stands for a detected proton or deuteron in the forward system and X can be any final state particle or several of them.

$$m_X = \sqrt{(p_{\text{beam}}^\mu + p_{\text{target}}^\mu - p_{\text{sp}}^\mu - p_A^\mu)^2} \quad (7.2)$$

The contributions are the four-momenta p^μ of the beam proton, target deuteron, spectator proton (sp) and nucleus in the final state (A) respectively (see App. A for a more detailed discussion on kinematics).

A proof of principle for the full analysis procedure is obtained by using a proton in the final state instead of a deuteron. As the vast majority of particles reaching the forward system are indeed protons, it is enough to open the cuts on fast deuterons (see Sec. 4.2) and to use the proton mass in p_A^μ in Eq. 7.2. One obtains the distribution shown in Fig. 7.4(a), which shows a prominent peak at a mass of $(953 \pm 3) \text{ MeV}/c^2$ ($\sigma = 38 \text{ MeV}/c^2$). It comprises quasi-free pn -elastic scattering with a spectator proton in the silicon telescope and quasi-free pp -elastic events. Nevertheless, in both cases the missing masses reconstructed should be equal within our experimental accuracy. The experimental result corresponds to the nominal value within little more than 1%. If one restricts the momenta of these particles such that the elastic channels are mostly suppressed, one obtains Fig. 7.4(b). On a broad background, which rises to the kinematical limit due to the acceptance of the system, a peak at $(1239 \pm 1) \text{ MeV}/c^2$ ($\sigma = 45 \text{ MeV}/c^2$) is observed. It can be clearly identified with the reaction $pn \rightarrow p\Delta^0$, where the central mass value of the Δ^0 is stated to be $1232 \text{ MeV}/c^2$ [80].²

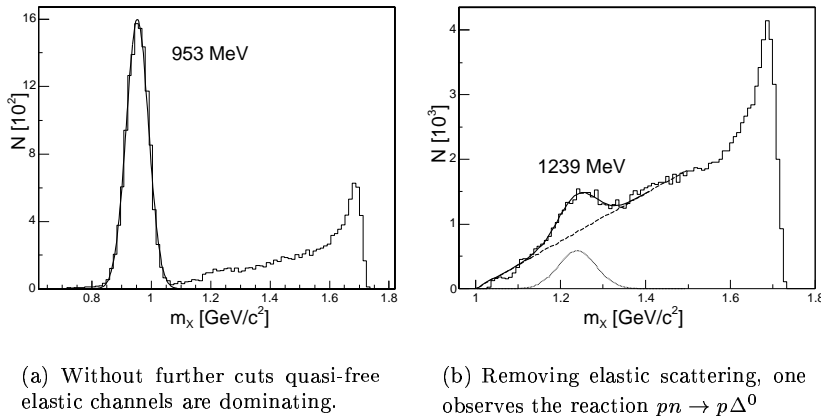


Figure 7.4: Missing mass distributions for $pd \rightarrow p_{sp}pX$. The observed peaks agree within the expected experimental accuracy with the masses of the neutron and the Δ with 939 MeV and 1232 MeV respectively.

Experimental distributions of the missing mass m_X using now selected fast deuterons (see Chap. 4) are shown in Fig. 7.5. Here all the available statistics for the four beam energies are included. The distributions are shown selecting protons in the 1st and 2nd layers of the silicon telescope. Thus the lower energy range $2.6 \leq T_{sp} \leq 4.4 \text{ MeV}$ of the spectator protons is covered.

From the experimental results (circles with error bars in Fig. 7.5), one observes a wide asymmetric peak, shifting with beam momentum but changing its shape only slightly. Most of it can be described by pure phase space for multipion production convoluted with the ANKE acceptance, which provides a severe cut at lower m_X . There is a clear indication of an ω signal at the highest Q interval but, in order to judge its significance, we have to model the large multi-pion background.

²Note, that this result was obtained fitting a straight line and a Gaussian to the distribution. Furthermore, the central mass value deduced from pion-induced reactions may well be altered due to the reaction mechanism and acceptance.

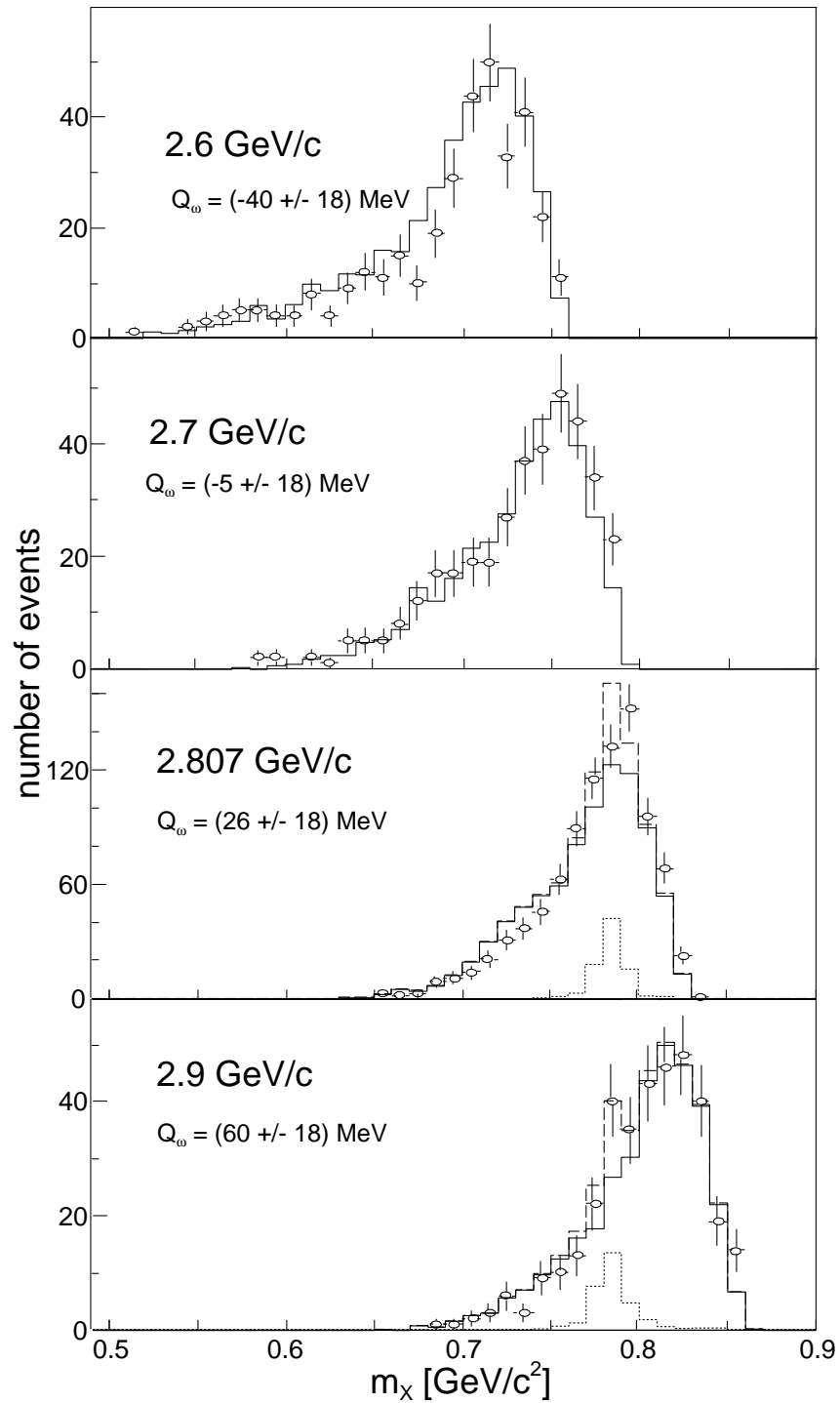


Figure 7.5: Experimental missing-mass spectra for $2.6 \leq T_{sp} \leq 4.4$ MeV and all beam momenta below and above the ω -threshold (from top to bottom): The estimated $N\pi$ -background (solid line) and ω -signal (dotted line) are described in section 7.3. Their sum is shown as dashed line.

7.3 Background Parametrisation

Although the interpolation of the background from just below to just above the ω threshold could equally well be taken from a purely empirical representation, phase-space simulations of multipion production together with a parametrisation of pion production in proton-proton collisions [81] have been taken to fit our data. We assume that, as in pp collisions [47], most of our background can be attributed to multi-pion production of type $pn \rightarrow d(N\pi)$. Due to the lack of data on multi-pion production in the pn -channel we have made the following approach to get an effective description of the shape of the background. Within our experimental errors the shape of our missing-mass spectra can be well described by multi-pion reactions from $pn \rightarrow d(N\pi)$ where $N = 2, 3, 4$. Smaller contributions like $pn \rightarrow pX$ ($\leq 10\%$), $pn \rightarrow d(5\pi)$ or $pn \rightarrow d\rho$ have been neglected.

In the absence of good pn data, we used three specific pp -reactions for multipion production [82] (see table 7.1). To fit these experimental data the total cross section $\sigma(s)$ has been parametrised as

$$\sigma(s) = A f\left(\frac{s_0}{s}\right) = A \left(1 - \frac{s_0}{s}\right)^{p_1} \left(\frac{s_0}{s}\right)^{p_2}, \quad (7.3)$$

which is a function of the centre-of-mass energy s in the pp channels, and s_0 is its value at the production threshold for the individual pion-channel. The parameter p_1 describes the phase-space behaviour near threshold. Together with the fitted parameter p_2 it determines the energy dependence $f(s_0/s)$ in Eq. 7.3 [81].³

	parametrisation for pp -data				fit to pn -data
	used reaction	p_1	p_2	A_{pp} [mb]	A_{pn} [mb]
2π	$pp \rightarrow d\pi^+\pi^0$	2	12.24	256	205
3π	$pp \rightarrow d2\pi^+\pi^-$	3,5	5.4	32	17
4π	$pp \rightarrow d2\pi^+\pi^-\pi^0$	5	5.2	110	14

Table 7.1: Parameters of Eq. 7.3 for pion channels contributing to the background in the ω -region. p_1 is fixed by phase space, p_2 and A_{pp} are extrapolated [81] from pp -data [82] on the reactions shown. The amplitude A_{pn} is the only parameter adjusted to describe our data in $pn \rightarrow dX$ (right column).

We assume that this parametrisation holds also for the description of the energy dependence in $pn \rightarrow d(N\pi)$ with $\sigma(s) = A_{pn} f(s_0/s)$. There are of course several channels contributing to a certain number of pions produced. For example in the 2π -production there are $pn \rightarrow d\pi^+\pi^-$ and $pn \rightarrow d2\pi^0$. We take the sum of their contributions without caring about their ratios. Only the determination of one parameter, the amplitude A_{pn} for the whole 2π -channel, has then to be done. The same considerations can, of course, be applied for all the pion-channels.

Phase-space simulations for the 2, 3 and 4 pion channel have been done at the four beam momenta as described above [70]. In the normalisation the

³A relativistic approach has also been investigated but, within our statistical errors, it does not change the description.

cross section parametrised by Eq. 7.3 leaves only the amplitude A_{pn} as a free parameter. The missing mass spectra in Fig. 7.5 were fitted such that an optimal description below threshold was obtained simultaneously with the reproduction of the shoulder at $Q = 60$ MeV. The resulting missing mass distributions are shown as solid lines in Fig. 7.5. Through this procedure the three amplitudes A_{pn} for the contributions from the 2, 3 and 4 π -channel are fixed to the values given in the right column of Table 7.1.

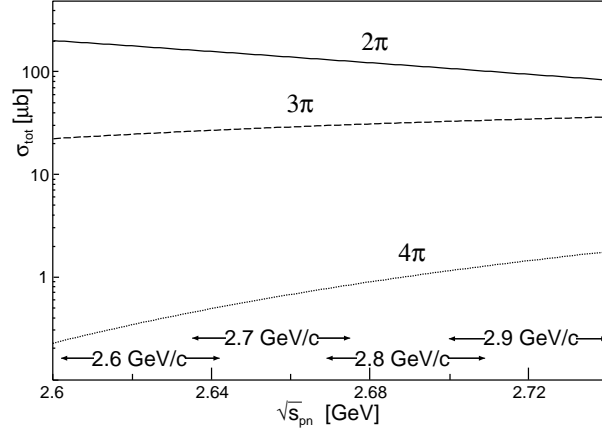


Figure 7.6: Parametrisation of the total cross section of multi-pion production. The cross section behaviour for 2, 3 and 4 pion production in $pn \rightarrow d(N\pi)$ is shown as solid, dashed and dotted lines respectively.

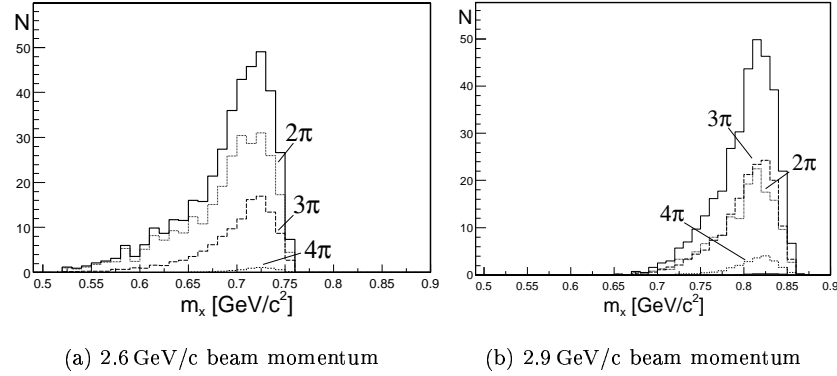


Figure 7.7: Due to cross section and acceptance changes with excess energy the ratio of the multi-pion production channels changes with beam momentum. Shown are the 2, 3 and 4 pion contribution and their sum as dotted, dashed, short dashed and solid lines respectively.

Note that, without any further free parameters, a plausible description of the background is obtained in all $\sqrt{s_{pn}}$ ranges. It should be emphasised that the parametrisation found is not claimed to necessarily describe the real total cross

sections for the pion production channels in $pn \rightarrow d(N\pi)$. This is mainly due to the fact, that only a small part of the phase space is accepted and no higher partial wave contributions have been used in the simulations⁴. Furthermore, the fit includes background apart from the three pion production channels, such as the residual proton contribution ($\leq 10\%$).

7.4 Cross Section for $pn \rightarrow d\omega$

At $Q = (60 \pm 18)$ MeV a clear peak for the ω is observed on the background, whereas at (26 ± 18) MeV the ω signal comes around the maximum of the acceptance and any evaluation of its strength depends much more critically upon the background assumptions. Nevertheless, within the parametrisation of Eq. 7.3, it is impossible to describe the maxima at the four excess energies in Fig. 7.5 without invoking some ω signal in the latter bin.

To quantify the ω contribution, phase space simulations for the channel $pn \rightarrow d\omega$ have been done. For that we take the $pn \rightarrow d\omega$ cross section to be constant over the Q -bin and equal to the physical cross section at the mean value of Q as described before. The optimal fit to the data is shown in Fig. 7.5, where the short dashed line is the ω signal and the long dashed line shows the sum with the pion background. To estimate the systematic error of the background description, the three parameters A_{pn} have been varied and the residual ω signal has been recorded for extreme cases, but still reproducing the background in all spectra within the statistic errors. From this analysis the upper and lower limit for the number of entries in the residual ω peak N_ω , shown in table 7.2, were obtained.

p_{beam} Q [MeV]	2.8 GeV/c 26 ± 18	2.9 GeV/c 60 ± 18
N_ω	60 – 100	27 – 33
\mathcal{L} [1/nb]	581	445
$\mathcal{L}_{\text{corr}}$ [1/nb]	385	254
$f_L \epsilon_{\text{acc}}$	12.6×10^{-5}	4.94×10^{-5}
$\langle \epsilon_{\text{eff}}^{\text{ev}} \rangle$	60.8%	41.6%
$\epsilon_{\text{eff}}^{\text{glo}}$	67%	
σ [μb]	3.0 – 5.0	7.7 – 9.5
stat. error	11%	18%

Table 7.2: Ranges for the residual ω signal obtained by the variation of the three parameters of the background description.

From the experimental number of $pn \rightarrow d\omega$ events N_ω the total cross section

$$\sigma_{\text{tot}} = \frac{N_\omega}{\mathcal{L}_{\text{corr}} f_L \epsilon_{\text{acc}} \langle \epsilon_{\text{eff}}^{\text{ev}} \rangle \epsilon_{\text{eff}}^{\text{glo}}} \quad \text{where} \quad \mathcal{L}_{\text{corr}} = f_{\text{sh}} \sum_{\text{run}} \frac{L \Delta t}{f_{\text{dt}} f_{\text{m2}}} \quad (7.4)$$

can be calculated with the integral luminosity $\mathcal{L}_{\text{corr}}$ corrected for shadowing $f_{\text{sh}} = 0.95$ and run-by-run for the dead time f_{dt} and multiplicity in the silicon-

⁴However, available $np \rightarrow d\pi^+\pi^-$ data in our energy range show the deuteron distribution to be fairly isotropic in the centre-of-mass system [83].

strip detector f_{m2} . Note, that these two latter factors have been used to determine the luminosity in Chap. 6 and thus effectively cancel out. The correction f_L for the fraction of luminosity in the centre-of-mass energy range is listed as a convolution with the acceptance ϵ_{acc} of the detection system in Table 7.2. Also from simulations the mean efficiency of the wire chambers $\langle \epsilon_{eff}^{ev} \rangle$ is obtained applying the “track-weight” event by event⁵. The contributions to the global efficiency $\epsilon_{eff}^{glo} = (67 \pm 7)\%$ are listed in Table 5.2 on page 50.

The value of the cross section were calculated using Eq. 7.4 with the given limits for the experimental events N_ω . The statistical error is deduced from the corresponding number of entries. The statistical uncertainty of the background is incorporated in the systematic error of the fit, which has been approximated by the variation in the number of detected events N_ω shown in Table 7.2. This will be discussed with other systematic errors in the following section.

7.5 Systematic Uncertainties

The total systematic error of the resulting cross sections comprises the systematic errors of the following five procedures carried out to obtain this quantitative result:

- The **efficiency determination** for the detection of a coincident spectator proton and fast deuteron at the experiment. A systematic error of 7% is taken as illustrated in Chap. 5.
- The **luminosity determination** by pd -elastic scattering, as discussed in Chap. 6, reveals a systematic error of 20%.
- The **fit of the background** in the missing mass distributions imposes a systematic uncertainty to the residual ω signal, as shown by the range of variation in table 7.2. The minimum and maximum value deviate by about $\pm 25\%$ for the Q interval around 26 MeV and by about $\pm 10\%$ for the highest Q -bin. These values are taken as estimates of the uncertainty from the background description.
- The **geometrical acceptance** introduces an uncertainty as the geometry of the set-up is only known with a certain precision. Studies show possible geometrical deviations in positions or beam angle, from which an systematic uncertainty of $\pm 7\%$ was deduced.
- The possible **contribution of higher partial waves** are taken as systematic uncertainties. For $Q = (60 \pm 18)$ MeV -17% and +35% are concluded as errors. For the $Q = (26 \pm 18)$ MeV point the uncertainty is, with -9% and +17%, much smaller.

It is assumed that all errors can be treated as σ of a dispersion. Thus the final result is obtained by adding all these values quadratically. They are listed for an overview in Table 7.3. Even though the individual contributions at the two excess energy ranges are quite different, the overall uncertainty is in both cases around 35%. For the excess energy range around 60 MeV there are two major

⁵The approach to introduce this efficiency to weight the experimental events yields the same results.

contributions. One comes from the luminosity L used for absolute normalisation and the second is due to the possible contribution of higher partial waves. In the $Q = (26 \pm 18)$ MeV range, the fit of the background plays a significant role, whereas the higher partial wave contribution is smaller.

Q [MeV]	26 ± 18		60 ± 18	
ϵ_{eff}	$\pm 7\%$			
L	$\pm 20\%$			
bg fit	$\pm 25\%$		$\pm 10\%$	
ϵ_{geo}	$\pm 7\%$			
P -wave	-9%	+17%	-17%	+35%
result	-35%	+38%	-29%	+42%

Table 7.3: Systematic errors in σ for the efficiency ϵ_{eff} , the luminosity L , the fit of the background “bg”, knowledge of geometry ϵ_{geo} and higher partial wave contributions denoted by “ P -wave”.

7.6 Results and Comparison with Predictions

In table 7.4 the obtained cross sections, including all corrections, are listed with statistical and systematic errors. It is found that the systematic uncertainty is larger than the error one would expect from statistical fluctuations alone. Thus the results for $pn \rightarrow d\omega$, shown as closed triangles in Fig. 7.8, include the systematic errors only. The FWHM of the Q ranges are drawn as horizontal bars. As there are no experimental data whatsoever existing on this channel, the $pp \rightarrow pp\omega$ data from SPESIII at SATURNE [47] and COSY-TOF [48] are shown as open circles and open square in the same plot.

p_{beam}	2.8 GeV/c	2.9 GeV/c
Q [MeV]	26 ± 18	60 ± 18
σ_{tot} [μb]	$4.0 \pm 0.4^{+1.5}_{-1.4}$	$8.6 \pm 1.5^{+3.6}_{-2.5}$

Table 7.4: Total cross sections σ_{tot} for two beam momenta p_{beam} and corresponding excess energy ranges Q . Shown are first the statistical errors and secondly the upper and lower systematic errors.

The lines and the shaded area in Fig. 7.8 indicate several theoretical calculations. The lower dash-dotted curve is a fit to the $pp \rightarrow pp\omega$ results, whereas all the other curves are the following predictions for the $pn \rightarrow d\omega$ reaction (see Sec. 1.1 for a general discussion on model calculations).

- The shaded area corresponds to cross section estimations of $pn \rightarrow d\omega$ following phase space behaviour published by V. Grishina *et al.* [84]⁶:
 $\sigma_{\text{tot}}(pn \rightarrow d\omega) \approx 2.2 \mu\text{b} \sqrt{Q/\text{MeV}}$.

⁶This is a factor of two lower than the estimate made in the initial proposal [49].

- The two extreme predictions from a relativistic meson-exchange model by Nakayama *et al.* [85] are shown as dashed lines in Fig. 7.8. The spread reflects the uncertainty remaining in this phenomenological approach after the adjustment of the parameters to the SATURNE data in the $pp \rightarrow pp\omega$ channel. The TOF data were not yet available for these calculations.
- In order to obtain a comparison with the η case, the phenomenological fit to the $pp \rightarrow pp\omega$ data given in Ref. [47] shown by the dot-dashed line has been used. Assuming a similar ratio of ω production in pn to pp collisions as in η case one obtains the solid line [35]⁷. The result lies in the middle of the previously presented model calculations.

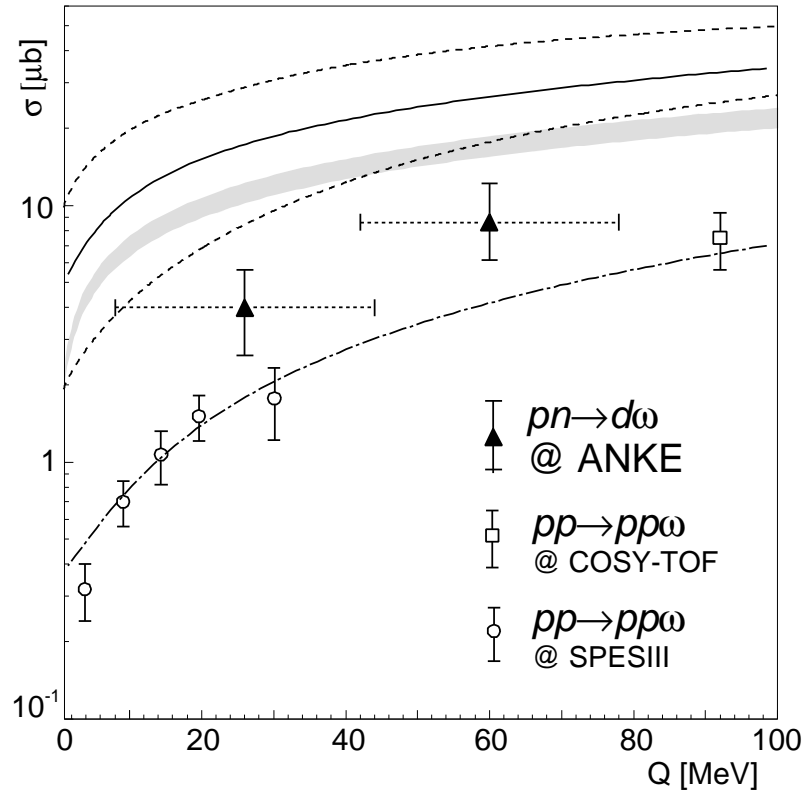


Figure 7.8: Total cross sections for ω -production. The $pp \rightarrow pp\omega$ data are taken from SATURNE [47] (open circles) and COSY-TOF [48] (open square), whereas the two ANKE $pn \rightarrow d\omega$ points from this work are given by the closed triangles. Only the systematic errors are shown as they are larger than the statistical errors. The horizontal bars indicate the Q range (FWHM) of the bins. The dot-dashed curve is the phenomenological fit to the $pp \rightarrow pp\omega$ results given in Ref. [47]. Several theoretical calculations shown as lines and shaded area overestimate the measured cross section significantly and are discussed in the text.

⁷The smearing with the width of the ω meson changes the behaviour only at $Q \leq 10$ MeV.

One sees that the experimental results on the cross section for $pn \rightarrow d\omega$ are much lower than those theoretically predicted. This corresponds to a deviation of 3σ in systematic uncertainty from the lowest theoretical model calculations. In view of this large discrepancy, one can already conclude from the present data that some other elements are required in the theoretical description.

One can try to speculate on the possible reasons for this disagreement. In Chap. 1 it is shown that a model invoking pure isoscalar exchange together with identical ISI and FSI implies a $pn \rightarrow pn\omega$ to $pp \rightarrow pp\omega$ ratio of 1. If one includes phase-space and FSI as in Ref. [8, 35] in order to deduce the $pn \rightarrow d\omega$ cross section, one finds that at about $Q = 60$ MeV it is equal to $pn \rightarrow pn\omega$. Thus, under this assumption, our point at about 60 MeV would be expected at the pp cross section. Our results lie between this scenario and the model predictions. As the model calculations turn out to be dominated by isovector exchange [85], the failure to describe such a situation is understandable. One could hence interpret the result as indication for a strong isoscalar contribution in the ω production mechanism. This would be a remarkable result, as in the η case the exchange of isovector mesons is believed to play the dominant role [2, 3, 6]. It remains to be seen how interferences of several exchange currents as well as possible isoscalar resonances, on which little knowledge is present, can change the results.

All these considerations show that further measurements are needed not only in the discussed channel $pn \rightarrow d\omega$, but also in the other channels to constrain the models.

Chapter 8

Outlook

From our first experimental data on the $pn \rightarrow d\omega$ cross section and their disagreement with all theoretical predictions, it is clear that further investigations are necessary both on the experimental as well as the theoretical side. I will restrict myself here to the experimental needs. First of all, the large uncertainties on the presented points must be reduced. In order to do that a beam time of two weeks has been allocated for August 2003. Moreover, we were encouraged by the Program Advisory Committee (PAC) for COSY to apply subsequently for further measurements closer to the threshold and with finer Q binning. In this chapter the improvements, which should lead to a significant reduction in systematics, will be discussed. Furthermore, ideas to measure the other isospin channels at ANKE or COSY11 are presented. Combining the results with those from the planned measurements of $pn \rightarrow d\phi$ at ANKE would allow a test of the OZI rule at low excess energies.

8.1 Ongoing $pn \rightarrow d\omega$ Measurements

Based on the experiences with the first generation silicon telescope and its limitations, modular self-triggering telescopes have been built [86]. Two of these set-ups, consisting of double-sided structured silicon-strip detectors, will be placed inside the COSY vacuum for the next measurements in August 2003. The basic scheme of particle identification and energy determination remains unchanged from its predecessor (see Chap. 3). Nevertheless, the following major improvements are evident:

- Since all detectors are double-sided structured silicon-strip detectors, the tracking capability for the whole energy range allows an installation close to an extended target. Particles can be traced and their angles reconstructed with an accuracy of $\sigma=1-3^\circ$, only limited by the angular straggling in the silicon.
- As a consequence of larger size detectors, the geometrical acceptance for the combination of both telescopes planned for installation in 2003 is increased by a factor of 20, compared to the first generation set-up.
- The set-up incorporates independent self-triggering capabilities in all layers. Thus an efficiency determination within the telescope is feasible for all layers.

- High rate capability is provided due to the fine segmentation. The telescope identifies a particle passage within 100 ns and provides, in combination with the self-triggering chips, a fast hit pattern recognition which improves the trigger-capabilities to handle higher rates.

In September 2001 a first prototype was installed at COSY and was commissioned parasitically during the data taking for ANKE. The results prove the excellent performance of the system in real experimental conditions.

Phase-space simulations have been performed in order to study the resolutions and optimise the geometrical arrangement of the detectors for the measurements [70]. It was proven that an arrangement of two silicon telescopes placed on opposite sides is well suited for the following reasons. Their size in combination with a large size target chamber, which has been installed at the end of 2002, will enable us to overcome most of the previously encountered systematic uncertainties for the luminosity determination. Furthermore, the combination of both telescopes will allow us to cover the full phase-space for the $pn \rightarrow d\omega$ reaction up to $Q = 100$ MeV at ANKE. In Fig. 8.1 distributions obtained by phase-space simulations of $pn \rightarrow d\omega$ in the experimental acceptance at ANKE illustrate that no severe gaps in acceptance appear. Thus the total cross section can be extracted in a model independent way. Moreover, provided enough statistics are available angular distributions could also be extracted.

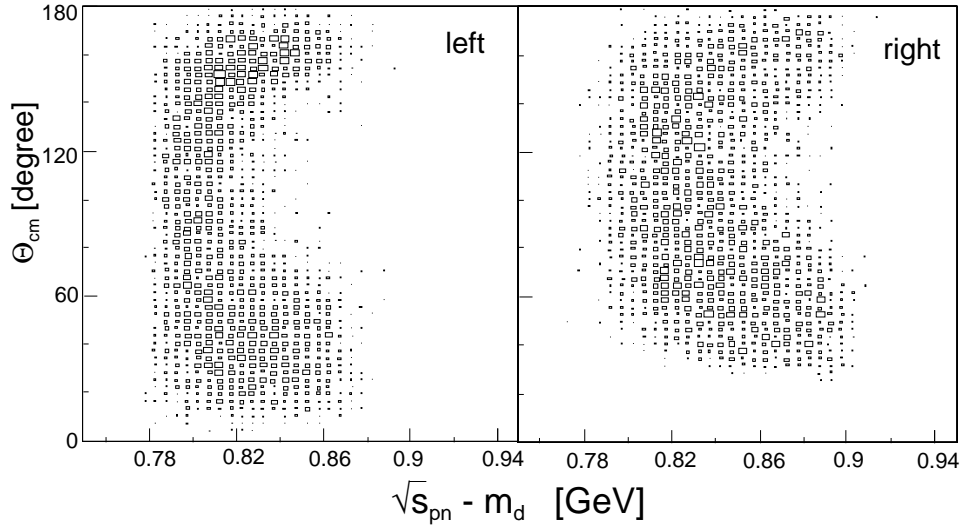


Figure 8.1: Excess energy *versus* the $d\omega$ angle in the centre-of-mass system for $pn \rightarrow p_{sp}d\omega$ in the silicon telescope placed on the left and right side of the COSY beam (left and right of the figure respectively). The combination of both telescopes allows us to cover the full phase-space over the whole Q range up to more than 100 MeV.

We conclude that measurements in an Q range from 0 to 100 MeV with a binning of 10 to 20 MeV can be performed at a single beam momentum scanning over the spectator distribution. However, the beam time required for these measurements crucially depends on the cross section of $pn \rightarrow d\omega$ and the multi-

pion background. Thus, measurement time was requested first to refine our results at energies above $Q = 50$ MeV and hence to fix the overall beam time required. Furthermore, the possibility to study angular distributions, which would allow us to draw conclusions on the contribution of higher partial waves, will be investigated. Finally we hope to extend the measurements to 5 or 10 MeV above threshold in order to study a possible close-to-threshold enhancement due to ω -nucleon interaction. This effect is observed in the η case [15] and it is of great interest whether a similar behaviour can be found in the ω production as well [27].

8.2 Further ω Production Channels

As mentioned before, it is of great theoretical interest to have data on all isospin channels. Apart from the pure $I = 0$ channel presented in this work, the $pp \rightarrow pp\omega$ reaction has been measured by two groups [47, 48], but leaving a large gap between 30 and 90 MeV excess energy. Further experimental points should be taken in. In this context it should be noted that Ref. [5] claims that the SATURNE data can not be described consistently with higher energy data. First estimates indicate that the measurements could be done at ANKE within a very short measurement time [87]. The last, not yet addressed, channel is the $pn \rightarrow pn\omega$ reaction. The studies could, in principle, be performed both at ANKE and COSY11 with some changes in the detection system. These changes seem feasible at rather low expense in money and manpower. Thus in this case joint efforts will be taken to evaluate the best choice of apparatus for the measurements. The time scale, however, for these projects will not be independent on the human resources available at the Forschungszentrum.

8.3 Test of the OZI Rule

The nine possible $q\bar{q}$ states from the u, d and s quarks form an octet containing the ϕ_8 and a singlet state denoted by ϕ_0 (both have $I = S = 0$) in the case of vector mesons. Due to SU(3) breaking, the physically observable mass eigenstates are a mixture of ϕ_8 and ϕ_0 called ω and ϕ . In case of ideal SU(3)-mixing, the ω is composed purely by u, d quarks whereas the ϕ contains only s quarks. In the quark model these mesons are then restricted both in production and decay. As the strong interaction conserves flavour, the production of a $s\bar{s}$ state (ϕ) from a non-strange initial state is only possible via three-gluon exchange. The resulting suppression is known as the Okubo-Zweig-Iizuka (OZI) rule [88–90]. If, however, the nucleons in the initial state contains strangeness, one can imagine the production as “kick out” of $s\bar{s}$ pairs. Thus, it has been suggested, e.g. in Ref. [91], to probe the intrinsic strangeness of the nucleons by measuring the ratio of cross sections $R_{\phi/\omega}$ from ϕ to ω production. Assuming a deviation of 3.7° from the ideal SU(3)-mixing angle $\theta_i = 35.3^\circ$ and the OZI rule to be strictly valid, this value can be calculated to be $R_{\phi/\omega} = f \cdot 4.2 \cdot 10^{-3}$, where f is the ratio of the phase-space factors of the two reactions. Several measurements of this ratio show inconsistent results up to $R_{\phi/\omega} = f \cdot (321 \pm 74) \cdot 10^{-3}$ [92].

A close-to-threshold measurement of the ϕ production in $pn \rightarrow d\phi$ has been proposed already in the COSY Proposal #75 [49]. However, the measurement

has not yet been performed. The comparison with the cross section of the $pn \rightarrow d\omega$ reaction would then be possible at the same momentum transfer. Neglecting differences in initial and final state interactions the ratio $R_{\phi/\omega}$ could be extracted directly from these measurements.

Appendix A

Mathematical Considerations

In this chapter a few mathematical relations are reviewed. This summary is by no means complete, but describes only relations important for the considerations required by this work. Firstly kinematical relations in spectator detection and elastic scattering are presented. Secondly error propagation in a special case is discussed. Lastly, the derivation of the ratio in different isospin channels is sketched.

A.1 Observables in Spectator Kinematics

Following the assumptions of the spectator model, discussed in Sec. 1.2, the detection of the spectator proton enables us to study the reaction $pn \rightarrow X$ by measuring $pd \rightarrow p_{\text{sp}}X$. The measurement of the three momentum of the spectator proton fixes the kinematics of the pn -entrance channel fully. The four momentum of the quasi-free neutron is then

$$p_n^\mu = p_{\text{target}}^\mu - p_{\text{sp}}^\mu, \quad (\text{A.1})$$

where p_{target}^μ and p_{sp}^μ are the four vectors of the target deuteron and spectator proton respectively. Due to momentum conservation $\mathbf{p}_n = -\mathbf{p}_{\text{sp}}$, but generally the invariant mass square of the rest particle

$$s_n = E_d - p_p = m_d^2 + m_p^2 - 2m_d \sqrt{p_{\text{sp}}^2 + m_p^2} \neq m_n^2, \quad (\text{A.2})$$

and this defines the off-shellness of this neutron.

For an incident proton beam with four momentum p_{beam}^μ this allows one to determine the centre-of-mass energy

$$\sqrt{s_{pn}} = \sqrt{(p_{\text{beam}}^\mu + p_{\text{target}}^\mu - p_{\text{sp}}^\mu)^2}, \quad (\text{A.3})$$

on a event-by-event basis. Subsequently, the excess energy Q for a certain reaction can be obtained by

$$Q := \sqrt{s_{pn}} - \sum_k m_k. \quad (\text{A.4})$$

This value can be determined from the spectator measurements alone up to the intrinsic width of the particles in the final state (with masses m_k). In case of the ω -production in the $pd \rightarrow p_{\text{sp}}d\omega$ reaction the excess energy,

$$Q = \sqrt{(p_{\text{beam}}^\mu + p_{\text{target}}^\mu - p_{\text{sp}}^\mu)^2} - m_d - m_\omega, \quad (\text{A.5})$$

is calculated with the central ω mass value $m_\omega = 782.6 \text{ MeV}/c^2$. The finite width, $\Gamma_\omega = 8.4 \text{ MeV}$, imposes an uncertainty comparable in size with the experimental resolution at ANKE. Similarly one can express the missing mass with four vectors as

$$m_X = \sqrt{(p_{\text{beam}}^\mu + p_{\text{target}}^\mu - p_{\text{sp}}^\mu - p_d^\mu)^2}. \quad (\text{A.6})$$

In the lab system the four vectors for the beam proton p_{beam}^μ , target deuteron p_{target}^μ , spectator proton p_{sp}^μ and deuteron in the final state p_d^μ can be expressed in masses m and three momenta \mathbf{p} of the respective particles:

$$p_{\text{beam}}^\mu = \left(\sqrt{m_p^2 + p_{\text{beam}}^2}, \mathbf{p}_{\text{beam}} \right) \quad ; \quad p_{\text{target}}^\mu = (m_d, \mathbf{0}) \quad (\text{A.7})$$

$$p_{\text{sp}}^\mu = (T_{\text{sp}} + m_p, \mathbf{p}_{\text{sp}}) \quad ; \quad p_d^\mu = \left(\sqrt{m_d^2 + p_d^2}, \mathbf{p}_d \right). \quad (\text{A.8})$$

Although in the analysis of the data this and other observables are evaluated using fully relativistic kinematics, the sensitivity to the measured quantities can be illustrated in a non-relativistic approximation in the spectator momentum p_{sp} . To order p_{sp}^2/m_p the square of the centre-of-mass energy is given by

$$s_{pn} = \tilde{s}_{pn} + 2 p_{\text{beam}} p_{\text{sp}} \cos \theta_{\text{sp}} - (E_{\text{beam}} + m_d) \frac{p_{\text{sp}}^2}{m_p} + O\left(\left(\frac{p_{\text{sp}}^2}{m_p}\right)^2\right), \quad (\text{A.9})$$

where \tilde{s}_{pn} is the value for a stationary neutron, i.e. corresponding to free pn -kinematics. Since the telescope is placed around $\theta_{\text{sp}} \approx 90^\circ$, $\partial s_{pn}/\partial \theta_{\text{sp}}$ is maximal there and so the value of Q depends sensitively upon the determination of the polar angle of the spectator.

Similarly the missing mass can be developed non-relativistically in terms of \mathbf{p}_{sp} to deduce the sensitivity to the spectator detection:

$$m_X^2 = \tilde{m}_X^2 + 2(\mathbf{p}_d - \mathbf{p}_{\text{beam}}) \mathbf{p}_{\text{sp}} - 2(E_{\text{beam}} - E_d + m_d) \frac{p_{\text{sp}}^2}{m_p} + O\left(\left(\frac{p_{\text{sp}}^2}{m_p}\right)^2\right), \quad (\text{A.10})$$

where \tilde{m}_X is the value obtained at $\mathbf{p}_{\text{sp}} = \mathbf{0}$. Since in our set-up the fast deuteron is measured near the forward direction, the same sort of sensitivity is found also for m_X when using Eq. A.9. However, in view of the ω width, the uncertainty in the beam momentum ($< 1 \text{ MeV}/c$) is unimportant for both Q and m_X at this level of accuracy.

A.2 Elastic Kinematics

A simple situation in terms of kinematics is the case of two particles scattering elastically. Then the momentum transfer and the particle types fix also the

energy transfer. Thus, knowing the initial state in pd elastic scattering (beam proton with known momentum impinging on a deuteron at rest), either the energy or the polar angle of a single identified particle in the final state fixes the reaction kinematics completely. One can calculate from the experimentally measured deuteron kinetic energy T_d both the momentum p_p and polar angle θ_p of the forward scattered proton. On the basis of energy conservation one gets

$$p_p^2 = p_{\text{beam}}^2 + T_d^2 - 2T_d \sqrt{m_p^2 + p_{\text{beam}}^2}, \quad (\text{A.11})$$

and momentum conservation is used together with the trigonometrical relation (cos-rule) to obtain

$$\cos \theta_p = \frac{p_{\text{beam}}^2 + p_p^2 - p_d^2}{2 p_p p_{\text{beam}}}. \quad (\text{A.12})$$

A.3 Error Propagation

Independent errors are usually added quadratically. However, two values are statistically independent only, if their fluctuations are completely uncorrelated. Let us e.g. consider the efficiency determination for a detector. The efficiency value can be defined straightforward by

$$\epsilon_D = \frac{N_D}{N}, \quad (\text{A.13})$$

the number of detected events N_D over the total number of events N in the acceptance of the system. If one tries to calculate the statistical error of this value one realises that, even though these numbers can not be directly expressed by each other, statistically they are not independent. This is because N_D is a subsample of all events N . To get two independent samples of events one should therefore take N_D and the number of missed events $N_M = N - N_D$ and calculate the error from

$$\epsilon_D(N_D, N_M) = \frac{N_D}{N_D + N_M} \quad (\text{A.14})$$

by the quadratic sum

$$\sigma \epsilon_D^2 = \left(\frac{\delta \epsilon_D}{\delta N_D} \sigma N_D \right)^2 + \left(\frac{\delta \epsilon_D}{\delta N_M} \sigma N_M \right)^2 \quad (\text{A.15})$$

$$\sigma \epsilon_D = \frac{1}{N^2} \sqrt{N_M^2 \sigma N_D^2 + N_D^2 \sigma N_M^2}. \quad (\text{A.16})$$

If one assumes Gaussian distributions one can approximate σN with \sqrt{N} and obtains:

$$\sigma \epsilon_D = \frac{1}{N^2} \sqrt{N_M^2 N_D + N_D^2 N_M} \quad (\text{A.17})$$

The binomial approach deviates from this result by an additional factor $\sqrt{N/(N-1)}$ in Eq. A.17 only. The difference becomes significant, if either N_D or N_M is a very small number. This latter approach was used for the calculations of the statistical errors in the cells of the efficiency maps.

A.4 Ratio of Isospin Channels

The amplitude A for the transition from an isospin state $|T\rangle$ to the same state as in the production of an isoscalar meson is purely defined by the coupling operators $\hat{\tau}_1$ and $\hat{\tau}_2$ of the nucleons to the intermediate meson. Thus using the expectation value $\langle \hat{\tau}_i^2 \rangle = 4t_i(t_i+1)$ with $t_i = 1/2$ for $i = 1, 2$ and an isovector meson exchanged

$$A \propto \langle T | \hat{\tau}_1 \cdot \hat{\tau}_2 | T \rangle = \frac{1}{2} \langle T | \hat{T}^2 - \hat{\tau}_1^2 - \hat{\tau}_2^2 | T \rangle = \begin{cases} -3 & \text{for } T = 0 \\ +1 & \text{for } T = 1 \end{cases} \quad (\text{A.18})$$

defines the ratio of amplitudes for $\langle 0 | \hat{\tau}_1 \hat{\tau}_2 | 0 \rangle$ to $\langle 1 | \hat{\tau}_1 \hat{\tau}_2 | 1 \rangle$ to be 3 for isovector meson exchange. For the exchange of isoscalar mesons the operator is the unity operator and hence $\langle T | \hat{1} | T \rangle = 1$ for any isospin state T [27]. These amplitudes enter quadratically in the cross section and thus $\sigma_{I=0}/\sigma_{I=1} = 9$. The ratio $R_{pn/pp}$ in Eq. 1.1 is then calculated to be $1/2(9+1) = 5$ for the exchange of an isovector meson like a pion. The same isospin considerations imply $R_{pn/pp}$ to be 1 for the case of an isoscalar meson exchanged.

Appendix B

Silicon Telescope

The set-up is described in Sec. 2.2 and the identification of protons and deuterons is shown in Chap. 3. Thus here only details on the geometry, crucial for the angular reconstruction, on the properties of the detectors detectors, and on the read-out are presented.

B.1 Geometry and Angular Reconstruction

The same view on the silicon telescope as in Fig. 2.3 on page 11 is sketched in Fig. B.1, showing only the dimensions important for the analysis (in millimetres). The relative distances between the target and the first detector as well as the offset between the two detectors along the beam axis are obtained experimentally (see Sec. 6.4.1). The position relatively to the flange was measured by ruler.

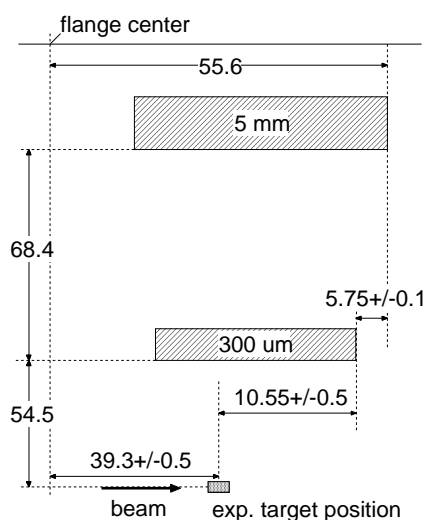


Figure B.1: Relevant geometrical dimensions (to the edges of the sensitive volumes) of the silicon telescope, as measured in August 2001.

Using this information the strip information from the detectors provide the polar angle of the particle.¹ To deduce the influence of the magnetic field, Monte Carlo simulations have been done [62, 70]. The difference to the straight line approach yielding θ_0 was parametrised as a function of the particle energy. The result for the reconstructed angle θ is,

- for protons stopped in the second layer with $2.6 < T_p < 4.4$ MeV:

$$\theta = \theta_0 + 1.56307 - 0.380564 T_p + 0.0534171 T_p^2 - 2.87111 \times 10^{-3} T_p^3 ,$$

- and for those stopped in the third layer with $7.8 < T_p < 21.8$ MeV:

$$\begin{aligned} \theta = \theta_0 + 7.12642 - 1.40573 T_p + 0.137378 T_p^2 - 6.84428 \times 10^{-3} T_p^3 \\ + 1.68783 \times 10^{-4} T_p^4 - 1.63459 \times 10^{-6} T_p^5 . \end{aligned}$$

For the analysis of the data this functionality was used, and all subsequent calculations were based on the obtained polar angles.

B.2 Silicon Detectors

If particles transverse matter there is always a certain probability of interaction, and for charged particles there are two main processes:

- inelastic collisions with the atomic electrons of the material
- elastic scattering on nuclei

The first process contributes to the main part of the particle's energy loss. By collecting the charge carriers, the ionising part of this energy loss can be measured in semiconducting materials. The collection of light, produced by de-excitation in scintillators, is much faster, but a lot less efficient than this. The requirements on energy resolution, the restricted space in the ANKE target region and the handling in ultra high vacuum, let us choose silicon semiconductor detectors for our set-up.

B.2.1 Surface Barrier Detectors

Production is done, by exposing etched silicon to air yielding a very thin layer of silicon oxide. This is then covered with a layer of gold for ohmic contact and protection. A reversed bias voltage, applied to this contact, and an indium contact on the back side (mostly covered by aluminium) create a depleted layer just below this silicon oxide layer. Therefore surface barrier detectors are most suitable for the detection of low energetic and high Z particles. The commercial ORTEC detectors we used² (see table B.1 on the next page) had a dead layer of approximately $40\mu\text{g}/\text{cm}^2$ gold, which corresponds to an energy loss of only 8.9keV for a 5.5MeV α -particle and 1.9keV for a 2MeV proton. The exit contact thickness was given to be: $40\mu\text{g}/\text{cm}^2$ aluminium. In Table B.1 on the facing page some properties are listed.

¹For protons with $T_{\text{sp}} < 4.4$ MeV the middle of the target is assumed to be their origin.

²All specifications by EG&G ORTEC

sensitive thickness	18 μm	60.9 μm
model no.	ED-095-300-25	ED-020-450-50
description	planar totally depleted	planar totally depleted
active area	300mm ²	450mm ²
si entr. window equ.	800Å	800Å
si exit window equ.	2250Å	2250Å
bias voltage	10V	35V

Table B.1: Properties of surface barrier detectors

Neglecting any mechanical contributions (mounting, connectors, *etc.*), detector noise is proportional to its capacitance, which is proportional to the active area and anti-proportional to the thickness of the depleted zone itself. Thus, it becomes clear that the larger sized 60 μm surface-barrier detector is affected less by this effect than its slightly smaller sized predecessor of only 18 μm thickness.

B.2.2 Silicon Strip Detectors

Due to this very thin oxide layer in the surface barrier detectors, the depletion zone cannot be extended very far into the silicon. Using ion implantation or diffused junction techniques, detectors can reach one or two millimetres depth of depleted zone and thus active detector thickness. By lithium drifting the density of the charge carriers in high purity silicon can be lowered even further, yielding the possibility to extend the depletion depth.

5 mm Thick Strip Detectors For our purposes D. Protić developed 5 mm thick silicon detectors. These detectors are boron-implanted from one side, and from the other lithium is thermally diffused into the detector at 350°C. The boron-doped p+ layer with a thickness of 0.1 μm is coated by 0.1 μm aluminium and represents the entrance window of this detector. This corresponds to an energy loss of approximately 30 keV for 5 MeV α particles and 3.3keV for 2MeV protons. On the back side the lithium-doped layer is between 0.5 and 0.7 μm thick and also coated with aluminium for ohmic contact to the bias voltage. Lithium of this layer has been drifted into the pure silicon by applying a strong reverse bias voltage at 60°C, to compensate for traces of boron acceptors in the highly pure silicon. In Fig. B.2 on the next page a cut through the detector is sketched showing also one representative groove between the strips.

These detectors are divided into strips of 250 μm and 234 μm pitch respectively, with a guard-ring surrounding the active area. The first type has been used at the test measurements in Cologne [55] and in another set-up previously installed at ANKE. The latter type performed well at ANKE beam time, providing us with data to determine luminosity at ANKE. (See Chap. 6) A resistor chain read-out was used on both types, but on the latter type the resistor chain was subdivided to achieve an acceptable dynamic range with a total of 200 strips. Table B.2 on the following page shows some properties of these detectors.

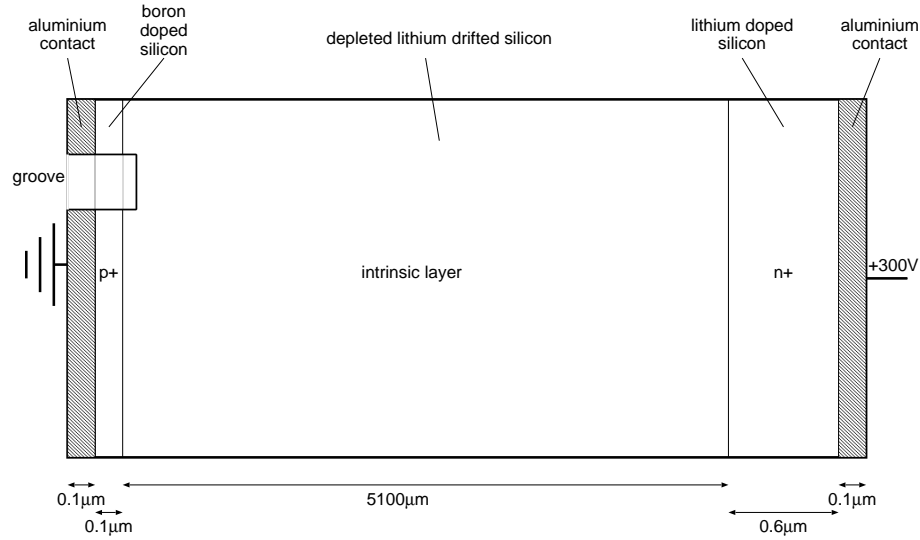


Figure B.2: Sketch of the thick strip-detector structure

	SW14-1	ST4-14B
pitch	$250\mu\text{m}$	$234\mu\text{m}$
groove width \times depth	$27(5)\mu\text{m} \times 1.5\mu\text{m}$	$23\mu\text{m} \times 4\mu\text{m}$
depletion depth	$3.0(1)$	$5.1(1)\text{mm}$
bias voltage	from 300V up to 500V	
active area ($l \times w$)	$10\text{mm} \times 20\text{mm}$	$46.8\text{mm} \times 23\text{mm}$
strips \times groups	80×1	50×4

Table B.2: Properties of the thick strip detectors

The large depletion zone makes drift times and diffusion relevant for discussion. The drift time for charge carriers sets direct constraints for electronic settings, and can lead to wrong conclusions, if not properly taken into account. Electron-hole pairs from particles, being stopped very close to the surface of the detector, create a fast signal from the positive charge carriers, and thus yield a good position resolution as diffusion is small. The drift time of the electrons then reaches its maximum value. For higher energy or lighter particles, which are stopped near the end of the detector, the drift time and the diffusion of the holes becomes maximal and therefore charges from a single hit gain their maximal spread in position at the strips. For minimum ionising particles, which deposit their charge almost evenly over the whole detector thickness, the maximum spread in charge collection time is reached.

Table B.3 on the next page shows some values for this detectors, which were obtained in two different ways. For electrons the velocity was extracted out of curves from Bertolini and Coche [93]. And for holes they were calculated by $v = \frac{q}{t} = \mu E$ with the mobility $\mu_h = 480 \text{ cm}^2/\text{Vs}$ for holes and $\mu_e = 1350 \text{ cm}^2/\text{Vs}$ for electrons [94], assuming the velocities to be far away from threshold and thus

obtaining a maximum value by this method.³ The diffusion is obtained then by: $\sigma_{diff} = \sqrt{2Dt}$ with diffusion constants calculated from the mobility. As the velocity at this field strength is still linearly dependent on the electric field, it is obvious, that the diffusion does not depend on the charge carriers.

	electrons	holes
velocity [$\frac{cm}{s}$]	8×10^5	2.8×10^5
max. drift time	640ns	1.8 μ s
diffusion constant	34.6 $\frac{cm^2}{s}$	12.3 $\frac{cm^2}{s}$
max. diffusion σ	67 μ m	67 μ m

Table B.3: Maximum diffusion and drift times in the 5 mm thick detector

As we can see in table B.3 the charge collection time due to drift time can be quite long, and should therefore be carefully considered. One disadvantage of the large integration times used to cope with the long charge collection times, is clearly the limitation in count rate imposed by it. The estimated pile-up can clearly be seen in the data obtained at the test beam time [55] with the Tandem Accelerator. The full width half maximum of the diffusion is less than 100 μ m, and therefore does not change the position resolution considerably.⁴

300 μ m Thick 32-Strip Detector In our set-up at the ANKE spectrometer we used a 300 μ m strip detector, commercially available from Canberra, as an angular sensitive intermediate layer between the 60 μ m and the 5 mm thick detector. The front surface of this “Passivated Implanted Planar Silicon (PIPS) Detector” is ion-implanted and passivated instead of coated by an evaporated metallic layer. According to Canberra this considerably reduces the entrance window thickness. This and other specifications given by Canberra are listed in table B.4.

	Canberra Detector
model no.	PF-32CD-15*32-300-EB
thickness	300 μ m
active area (l \times w)	32mm \times 15mm
si entr. window equ.	0.7 – 1.5 μ m
pitch	1mm
strips	32
bias voltage	20V

Table B.4: Properties of Canberra 300 μ m strip detector

³The minimum bias voltage was used to derive upper limits only.

⁴A slight change in the beam profile due to this effect could be seen in the data from the Cologne test beam time, but the evidence is weak.

B.3 Signal Processing

B.3.1 Shaping and Dynamic Range

The main goal for the read-out electronics is the amplification of comparatively small deposited charges in the silicon detector to a signal with a reasonable amplitude for the analysis in a multichannel analyser (typically $\lesssim 10\text{V}$). This voltage should be proportional to the deposited charge over the whole range, which is to be analysed.

The read-out chain for our silicon detectors is set up as follows: A charge-sensitive preamplifier is installed as close to the detector as possible, to reduce the input capacitance and therefore the noise produced on the very sensitive input side. The signal is amplified again in the main amplifier(s), which provide(s) adjustable amplification, shaping and pole zero correction, to be then transmitted to an analyser, which produces a channel number corresponding to the amplitude of the signal. Amplification was adjusted, to cover the amplitude range of the multichannel analyser, and a correct pole zero adjustment ensures the proportionality to the deposited charge.

Shaping Because the fast rising slope from the signal contains the basic information on the charge, differentiation is done with RC networks. Therefore the system provides a good signal from the charge even for high count-rates. The sharp differentiated signal is difficult to process and contains all high-frequency components of any noise produced in the system. Subsequent integration of the signal is often done in many steps by CR-networks, to produce a nearly Gaussian shape of the signal, which minimises noise and can be well processed in the further chain.

Triggering In order to identify an event in the detector, a certain threshold has to be set; and the read-out has to be activated only if this threshold is exceeded. Usually a fast signal is used for that, because it ensures correct timing. A discriminator is used to set a threshold and produce a logic signal, which has to be delayed by the right amount to trigger the peak of the slow signal. In the following the further processing of this trigger signal is described.

Dynamic Range The dynamic range of the individual amplifiers is determined by the linear region of the amplifiers. The charge collection in the detector itself is also not complete and depending on the charge produced per volume. On the electronic side the linearity of the channel analyser and all the components processing this slow main signal have to be considered. The fast triggering channel can also affect the dynamic range, either by the disability to trigger on certain pulse-heights or due to timing shifts, which can lead to an amplitude loss, if the gate is not adjusted widely enough.

B.3.2 Resistor-Chain Read-Out

For the read-out of a micro-strip detector, the usage of an individual read-out chain for each strip, requires an advanced technology to produce vacuum compatible preamplifier boards with the dimensions of the detector pitch or vacuum-connectors with a huge amount of cables in the vacuum. Apart from

the amount of work which is needed, this and all the other components of the read-out increases the price of the set-up by a large amount. Developments are done in this respect just now, but as a first step the read-out by resistor chain was employed.

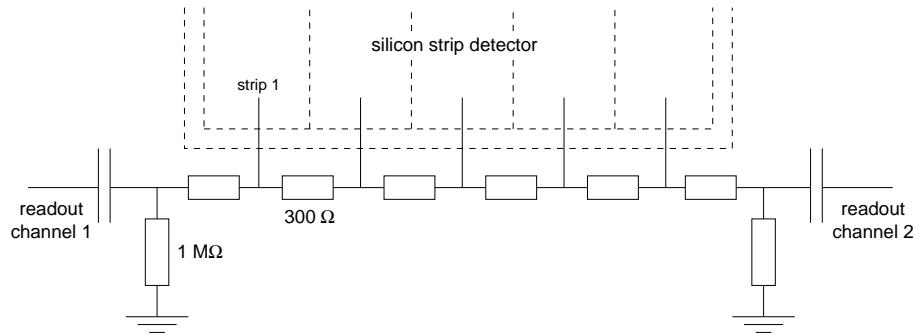


Figure B.3: Sketch of a resistor chain read-out

In Fig. B.3 is sketched how each strip is connected to its neighbouring one by a defined ohmic resistor in this type of read-out. Two read-out channels are then sufficient to get the energy and position of the incident particle. The dynamic range for deposited charges in the detector is unfortunately severely affected by this method. For a middle hit the charge is equally split into both pre-amplifiers, but for a hit in a strip at the edge of the detector the amplitude of the signal is divided by the amount of strips (-1) in the chain in the most distant channel. As a signal in both channels is needed to determine total energy loss and position of the particle, the read-out has to provide a dynamic range with a factor equally to the amount of the strips additionally to the range of deposited energies, that should be detected. Thus a huge dynamic range for the electronics is needed, if a resistor chain read-out is used. We divided the read-out chain at the ANKE beam time in four segments with 50 strips each, to cover an acceptable energy range.

B.3.3 Set-up at ANKE

The pre-amplifiers(PA) were directly mounted to the vacuum-flange to reduce cable length to a minimum for non-vacuum compatible electronics. The working scheme of is sketched in Fig. B.4. The fast and slow main amplifiers(MA) were situated in different modules and could be adjusted independently. The slow signal from the main amplifier was transferred to a stretcher module, which holds the maximum signal amplitude in the given gate by the discriminator(CFD). We can use some time delays(TD) to produce a gate with a fixed width for the digital converter(QDC). Within the gate width the QDC accumulates the charge obtained from the stretcher and converts the integrated charge into a channel information. The essential components are sketched in Fig. B.4.

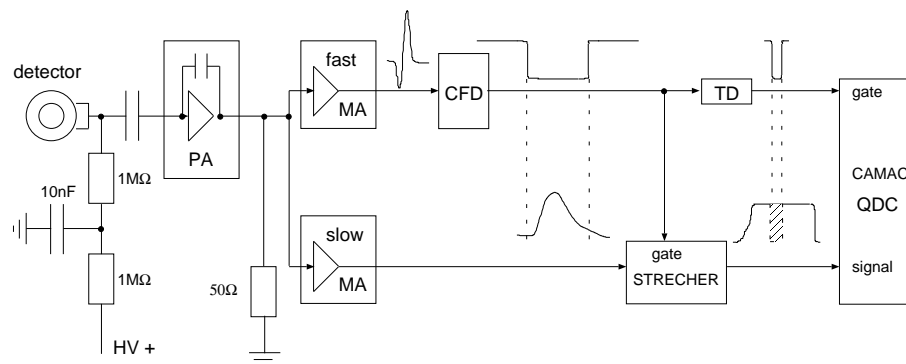


Figure B.4: Sketch of the electronic set-up at ANKE

The 41 channels used at the ANKE beam time in August 2001 were set up in this fashion with most electronics being multi-channel devices, as listed in the Table B.5.

	model
pre-amplifier	CSPA02
main amplifiers	16 ch. fast shaper NEL 4.16.02.1 16 ch. shaper NEL 4.16.01.0
discriminator	PS octal discr. 710
time delay	C.A.E.N dual timer 2255
stretcher	LeCroy 3309 PTQ
channel analyser	LeCroy 4300B FERA
controller	CAMAC-FERA-PCI

Table B.5: Electronic components

Appendix C

Figures and Tables

Listing of all runs in August 2001					
run	f_{dt}	f_{m2}	f_{m3}	$L [10^{30} \text{cm}^{-2} \text{s}^{-1}]$	$\mathcal{L} [10^{30} \text{cm}^{-2}]$
2.6 GeV/c, $\Delta\sigma = 5.10 \mu\text{b}$, $d_{\text{image-cut}} = 17.8 \text{ mm}$					
3583	1.207	1.046	1.009	3.508±0.111	12832
3586	1.206	1.048	1.009	3.578±0.075	28617
3588	1.007	1.025	1.002	0.385±0.060	557
3589	1.108	1.038	1.007	1.953±0.128	2125
3590	1.212	1.049	1.009	3.721±0.066	30793
3591	1.178	1.045	1.008	3.095±0.058	29858
3592	1.168	1.044	1.008	3.094±0.058	34521
3593	1.237	1.052	1.011	4.363±0.088	32279
3632	1.372	1.047	1.009	3.613±0.095	21560
3633	1.183	1.035	1.005	2.120±0.260	1202
3634	1.272	1.042	1.007	3.245±0.201	4587
3635	1.277	1.042	1.007	2.902±0.161	3625
3636	1.287	1.043	1.007	2.918±0.056	29946
3638	1.283	1.043	1.007	2.930±0.056	32395
3639	1.323	1.046	1.008	3.366±0.067	29479
3640	1.265	1.043	1.008	3.181±0.395	860
3641	1.409	1.053	1.011	4.442±0.096	35569
3642	1.294	1.046	1.009	3.533±0.086	32799
3643	1.206	1.040	1.007	2.562±0.072	19260
3644	1.381	1.053	1.010	4.296±0.317	2146
3645	1.514	1.061	1.012	5.848±0.124	29525
3646	1.563	1.064	1.013	6.111±0.261	7389
3647	1.515	1.061	1.012	5.610±0.211	8560
3648	1.500	1.059	1.012	5.434±0.183	10626
3649	1.482	1.059	1.012	5.979±0.402	3635
3650	1.440	1.056	1.011	4.880±0.093	34733
3651	1.410	1.052	1.010	4.407±0.086	33357
3652	1.441	1.054	1.011	5.094±0.122	26812
3653	1.481	1.057	1.011	5.131±0.103	33576
3654	1.516	1.059	1.012	5.558±0.116	34994
3655	1.445	1.055	1.011	4.787±0.092	35522
3661	1.564	1.062	1.013	6.155±0.126	39862

...continued overleaf

run	f_{dt}	f_{m2}	f_{m3}	$L [10^{30} \text{cm}^{-2} \text{s}^{-1}]$	$\mathcal{L} [10^{30} \text{cm}^{-2}]$
3662	1.796	1.075	1.016	8.032 ± 0.160	45407
3663	1.992	1.086	1.020	9.869 ± 0.230	45514
3664	1.925	1.083	1.018	9.061 ± 0.187	41918
3665	1.740	1.073	1.015	6.871 ± 0.121	36094
3666	1.671	1.069	1.015	6.994 ± 0.137	39930
3667	1.646	1.067	1.015	6.756 ± 0.138	38656

2.7 GeV/c, $\Delta\sigma = 5.07 \mu\text{b}$, $d_{\text{image-cut}} = 17.8 \text{mm}$

3685	1.512	1.058	1.013	6.005 ± 0.129	37749
3686	1.707	1.070	1.016	8.209 ± 0.205	31210
3687	1.700	1.070	1.016	8.126 ± 0.279	15862
3688	1.682	1.069	1.015	7.829 ± 0.156	44680
3689	1.721	1.071	1.016	7.970 ± 0.167	39278
3690	1.729	1.073	1.016	8.667 ± 0.186	41485
3691	1.706	1.072	1.016	8.309 ± 0.164	45540
3692	1.807	1.075	1.017	8.717 ± 0.230	25473
3693	1.989	1.083	1.019	10.473 ± 0.208	55613
3694	2.070	1.087	1.020	10.471 ± 0.202	59625
3695	1.785	1.073	1.016	8.345 ± 0.173	42145
3696	1.699	1.068	1.015	7.466 ± 0.159	39081
3697	1.626	1.064	1.014	6.429 ± 0.223	12331

2.8 GeV/c, $\Delta\sigma = 5.01 \mu\text{b}$, $d_{\text{image-cut}} = 17.6 \text{mm}$

3577	1.225	1.046	1.010	4.075 ± 0.153	11379
3578	1.185	1.043	1.009	4.001 ± 0.353	2336
3579	1.165	1.041	1.008	3.010 ± 0.057	31317
3580	1.386	1.063	1.014	6.216 ± 0.119	30770
3581	1.330	1.058	1.012	5.545 ± 0.108	35692
3582	1.132	1.038	1.007	2.446 ± 0.054	21738
3594	1.306	1.057	1.012	5.834 ± 0.101	37313
3595	1.266	1.053	1.011	5.434 ± 0.097	38743
3596	1.397	1.066	1.015	7.578 ± 0.144	39056
3597	1.344	1.061	1.012	6.585 ± 0.184	14550
3604	1.159	1.040	1.009	3.145 ± 0.278	2077
3606	1.342	1.059	1.012	6.190 ± 0.154	21126
3607	1.410	1.057	1.012	5.853 ± 0.229	9153
3608	1.392	1.055	1.011	5.528 ± 0.181	11894
3609	1.395	1.054	1.011	5.383 ± 0.094	42517
3610	1.414	1.056	1.012	6.810 ± 0.865	1542
3611	1.339	1.050	1.010	4.817 ± 0.100	33521
3612	1.308	1.047	1.009	4.359 ± 0.084	35382
3613	1.393	1.054	1.011	5.398 ± 0.125	27292
3614	1.302	1.047	1.009	4.088 ± 0.090	22541
3615	1.600	1.064	1.013	5.772 ± 0.111	30522
3616	1.359	1.048	1.009	4.491 ± 0.112	21441
3617	1.508	1.056	1.011	5.981 ± 0.123	36082
3618	1.540	1.056	1.011	5.985 ± 0.112	41657
3619	1.623	1.061	1.012	6.297 ± 0.127	32095
3623	1.407	1.045	1.010	3.863 ± 0.201	11611
3624	1.836	1.067	1.015	11.724 ± 1.578	3163
3625	1.906	1.074	1.016	8.701 ± 0.155	55759
3626	2.038	1.079	1.018	9.686 ± 0.192	51563
3627	1.580	1.056	1.011	4.948 ± 0.099	38212

...continued overleaf

run	f_{dt}	f_{m2}	f_{m3}	$L [10^{30}\text{cm}^{-2}\text{s}^{-1}]$	$\mathcal{L} [10^{30}\text{cm}^{-2}]$
3628	1.435	1.049	1.009	4.876 ± 0.117	29384
3629	1.632	1.061	1.013	5.788 ± 0.244	7416
3656	1.511	1.057	1.012	5.884 ± 0.109	42542
3657	1.536	1.059	1.012	6.150 ± 0.121	38535
3658	1.556	1.060	1.013	6.734 ± 0.330	6781
3659	1.630	1.064	1.014	7.403 ± 0.147	45629
3660	1.436	1.052	1.011	5.279 ± 0.188	11558
2.9 GeV/c, $\Delta\sigma = 4.88\mu\text{b}$, $d_{\text{image-cut}} = 17.6\text{ mm}$					
3711	1.533	1.057	1.013	7.204 ± 0.458	7595
3713	1.620	1.062	1.014	8.012 ± 0.168	46571
3714	1.654	1.063	1.014	7.386 ± 0.302	10076
3715	1.596	1.060	1.014	7.754 ± 0.409	7174
3716	1.524	1.054	1.012	6.643 ± 0.157	31634
3726	1.510	1.053	1.015	5.928 ± 0.120	36771
3727	1.504	1.051	1.015	6.040 ± 0.146	37334
3728	1.479	1.051	1.014	5.558 ± 0.111	36471
3729	1.556	1.055	1.015	6.155 ± 0.132	32440
3730	1.581	1.058	1.015	7.180 ± 0.214	19841
3732	1.545	1.055	1.014	5.721 ± 0.283	5435
3733	2.209	1.056	1.015	8.604 ± 0.461	7556
3735	1.636	1.055	1.014	6.239 ± 0.279	6813
3736	1.585	1.052	1.014	5.568 ± 0.212	8446
3737	1.450	1.053	1.013	5.837 ± 0.133	25646
3739	1.452	1.053	1.013	5.929 ± 0.257	7827
3743	1.633	1.054	1.014	6.103 ± 0.112	43509
3744	1.652	1.055	1.014	6.288 ± 0.113	49833
3745	1.635	1.054	1.014	6.241 ± 0.124	45283
3746	1.622	1.053	1.013	5.661 ± 0.163	19607

Table C.1: List of all runs showing the correction factors for dead-time f_{dt} and hit multiplicity f_{m2} and f_{m3} in the 2nd and 3rd layers of the silicon telescope respectively. Furthermore, the luminosity L and integrated luminosity \mathcal{L} are listed. For every beam momentum also the fraction of cross section $\Delta\sigma$ accepted for $pd \rightarrow pd$, defined by Eqs. 6.4 and 6.7, and the cut on the target image $d_{\text{image-cut}}$, described in Sec. 6.4.3, are shown.

run	events	reason for exclusion	region
2.6 GeV/c			
3588	$0.14 \cdot 10^6$	target & efficiency	no
3633	$0.25 \cdot 10^6$	target	yes
3634	$0.98 \cdot 10^6$	target	yes
3640	$0.20 \cdot 10^6$	target	yes
3644	$0.53 \cdot 10^6$	HV-change	yes
3645	$6.56 \cdot 10^6$	target & HV-change	yes
3649	$0.76 \cdot 10^6$	target	yes
3652	$5.68 \cdot 10^6$	target	yes
3655	$8.10 \cdot 10^6$	efficiency	yes
statistics: $23.19 \cdot 10^6$ ev (11% of total)			
2.7 GeV/c			
3685	$7.63 \cdot 10^6$	efficiency	no
3693	$9.36 \cdot 10^6$	target	no
3697	$2.63 \cdot 10^6$	target	no
statistics: $19.62 \cdot 10^6$ ev (22% of total)			
2.8 GeV/c			
3577	$2.43 \cdot 10^6$	target	no
3578	$0.48 \cdot 10^6$	target	no
3597	$3.23 \cdot 10^6$	target	no
3603	$6.66 \cdot 10^6$	electronics	no
3604	$0.47 \cdot 10^6$	target	no
3610	$0.27 \cdot 10^6$	target	no
3615	$6.36 \cdot 10^6$	efficiency	no
3624	$0.34 \cdot 10^6$	target	no
3626	$8.11 \cdot 10^6$	efficiency	yes
3627	$7.10 \cdot 10^6$	efficiency	yes
3628	$5.52 \cdot 10^6$	efficiency	yes
3629	$1.56 \cdot 10^6$	target	yes
statistics: $42.53 \cdot 10^6$ ev (21% of total)			
2.9 GeV/c			
3733	$1.48 \cdot 10^6$	target	no
3737	$5.26 \cdot 10^6$	efficiency	no
3739	$1.58 \cdot 10^6$	efficiency	no
statistics: $8.32 \cdot 10^6$ ev (9% of total)			

Table C.2: Here are listed the excluded runs, their statistics, and the reason for exclusion: **Target:** The analysis of the geometrical target position and shape, which is vitally important for the luminosity determination, shows that there are some runs where considerations on several rate informations are not conclusive. **HV-change:** A high voltage change for the photomultipliers of the forward hodoscope leaves amplitudes unclear for two runs. **Efficiency:** The single-cluster efficiency of the MWPCs dropped for a few runs dramatically. This is probably due to electronic generations, and has not been investigated further, as the loss in statistics is not significant. **Region:** Due to strong changes in MWPC efficiency the region from run 3626 to run 3662 was completely excluded. Only runs which were already excluded due to other reasons are listed explicitly and marked with “yes”.

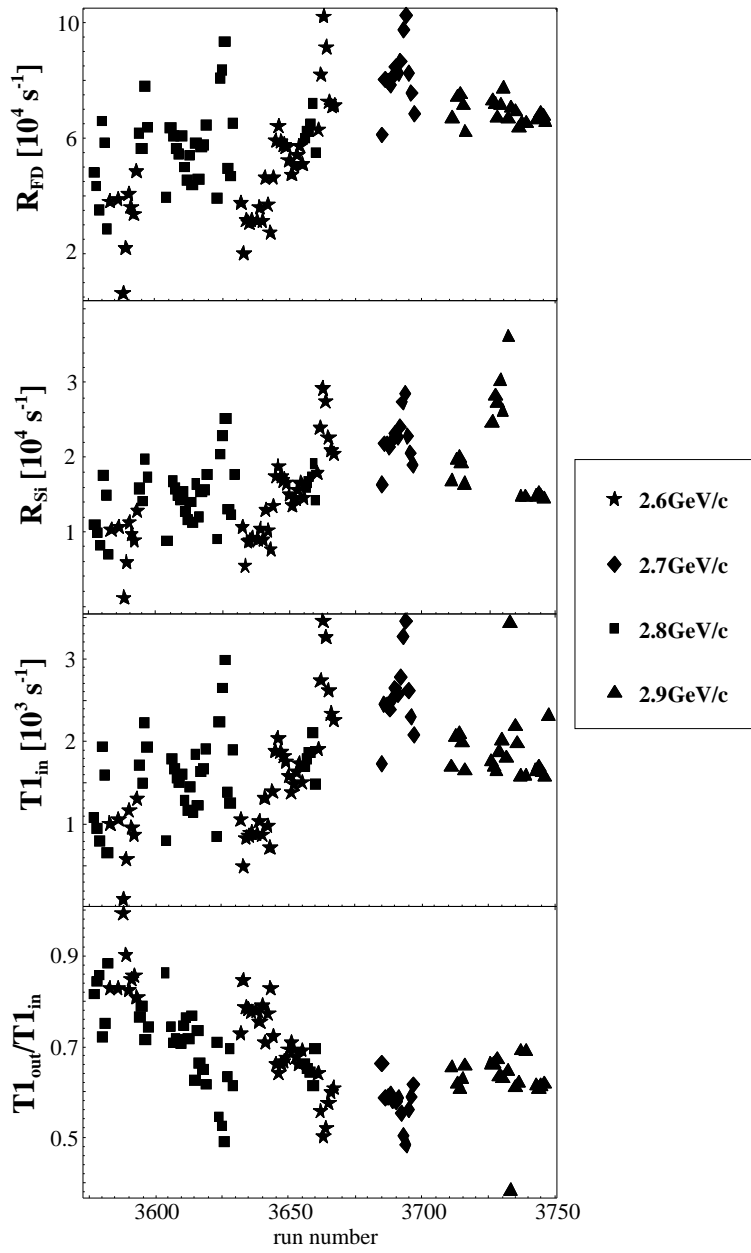


Figure C.1: Mean count rates per run of the forward hodoscope R_{FD} and the silicon telescope R_{SI} and the DAQ dead time correction $T1_{out}/T1_{in}$ for the beam time in August 2001.

Bibliography

- [1] Xavier Calmet and Harald Fritzsch. Symmetry breaking and time variation of gauge couplings. *Phys. Lett.* **B 540**, 173 (2002).
- [2] V. Baru, A.M. Gasparyan, J. Haidenbauer, C. Hanhart, A.E. Kudryavtev and J. Speth. Production of η mesons in nucleon-nucleon collisions. arXiv: nucl-th/0212014 (2002).
- [3] Göran Fäldt, Tord Johansson and Colin Wilkin. Near-Threshold Production of η and η' Mesons in pp and pd Collisions. *Physica Scripta* **T 99**, 146 (2002).
- [4] K. Tsushima and K. Nakayama. Near-Threshold ω -meson production in proton-proton collisions: With or without resonance excitations? In 6th International Conference on Particles and Nuclei (PANIC 02). Osaka, Japan. ArXiv:nucl-th/0211065 (2002).
- [5] K. Tsushima and K. Nakayama. Near-threshold ω and ϕ meson productions in pp collisions. arXiv: nucl-th/0304017 *Phys. Rev. C* (in press) (2003).
- [6] N. Kaiser. $pp \rightarrow pp\omega$ reaction near threshold. *Physical Review* **C 60** (1999).
- [7] K. Nakayama, A. Szczurek, C. Hanhart, J. Haidenbauer and J. Speth. Production of omega mesons in proton proton collisions. *Phys. Rev. C* **57**, 1580 (1998).
- [8] G. Fäldt and C. Wilkin. The production of η mesons in nucleon-nucleon collisions near threshold. *Physica Scripta* **64**, 427 (2001).
- [9] C. Hanhart and K. Nakayama. On the treatment of N N interaction effects in meson production in N N collisions. *Phys. Lett.* **B 454**, 176 (1999).
- [10] E. Chiavassa *et al.*. Measurement of the $pp \rightarrow pp\eta$ total cross section between 1.265 and 1.50 GeV. *Phys. Lett.* **B 322**, 270 (1994).
- [11] F. Hibou *et al.*. Comparison of η and η' production in the $pp \rightarrow pp\eta(\eta')$ reactions near threshold. *Phys. Lett.* **B 438**, 41 (1998).
- [12] H. Calén *et al.*. The $pp \rightarrow pp\eta$ reaction near the kinematical threshold. *Phys. Lett.* **B 366**, 39 (1996).
- [13] H. Calén *et al.*. Measurement of the Quasifree $pn \rightarrow d\eta$ Reaction near Threshold. *Physical Review Letters* **79**, 2642 (1997).

-
- [14] H. Calén *et al.*. Measurement of the quasifree $pn \rightarrow pn\eta$ reaction. *Physical Review C* **58**, 2667 (1998).
- [15] H. Calén *et al.*. Threshold structure of the quasifree $pn \rightarrow d\eta$ reaction. *Phys. Rev. Lett.* **80**, 2069 (1998).
- [16] J. Smyrski *et al.*. Near-threshold η meson production in proton-proton collisions. *Phys. Lett. B* **474**, 182 (2000).
- [17] Pavel Moskal. private communication (2002).
- [18] Tord Johansson. private communication (2003).
- [19] D. M. Binnie *et al.*. Study of narrow mesons near their thresholds. *Phys. Rev. D* **8**, 2789 (1973).
- [20] J. Keyne *et al.*. Study of ω production near threshold in the reaction $\pi^- p \rightarrow \omega n$. *Phys. Rev. D* **14**, 28 (1976).
- [21] H. Karami *et al.*. Elastic scattering and ω meson production near the threshold of $\pi^- p \rightarrow \omega n$. *Nucl. Phys. B* **154**, 503 (1979).
- [22] G. Penner and U. Mosel. Vector meson production and nucleon resonance analysis in a coupled channel approach for energies $m(N) < s^{(1/2)} < 2$ GeV. I: Pion induced results and hadronic parameters. *Phys. Rev. C* **66**, 055211 (2002).
- [23] G. Penner and U. Mosel. Vector meson production and nucleon resonance analysis in a coupled channel approach for energies $m(N) < s^{(1/2)} < 2$ GeV. II: Photon induced results. *Phys. Rev. C* **66**, 055212 (2002).
- [24] C. Hanhart, A. Sibirtsev and J. Speth. The reaction $\pi N \rightarrow \omega N$ revisited: The ωN scattering length. arXiv: hep-ph/0107245 (2001).
- [25] C. Hanhart and A. Kudryavtsev. On momentum dependence of the reaction $\pi^- p \rightarrow \omega n$ near threshold. *Eur. Phys. J. A* **6**, 325 (1999).
- [26] G. Penner and U. Mosel. What is the correct $\pi^- p \rightarrow \omega n$ cross section at threshold? arXiv: nucl-th/0111024 (2001).
- [27] Christoph Hanhart. private communication (2003).
- [28] H. Garcilazo and M. T. Pena. The reaction $np \rightarrow \eta d$ near threshold. *Phys. Rev. C* **66**, 034606 (2002).
- [29] B. Povh, K. Rith, C. Scholz and F. Zetsche. *Teilchen und Kerne*. Springer, 5 edition (1999).
- [30] R. J. Glauber. *Lectures in Theoretical Physics*, volume 1. Interscience Publishers, New York, W. Brittin edition (1959).
- [31] E. Chiavassa *et al.*. eta meson production in p d and p p collisions. *Phys. Lett. B* **337**, 192 (1994).
- [32] F. Duncan *et al.*. Differential Cross Section of the $pn \rightarrow pp(^1S_0)\pi^-$ Reaction Extracted from $pd \rightarrow ppp\pi^-$. *Physical Review Letters* **80**, 4390 (1998).

- [33] P. Moskal, M. Wolke, A. Khoukaz and W. Oelert. Close-to-threshold meson production in hadronic interactions. *Prog. Part. Nucl. Phys.* **49**, 1. ArXiv: hep-ph/0208002 (2002).
- [34] Leonid Kondratyuk. private communication (2003).
- [35] Colin Wilkin. private communication (2003).
- [36] C. H. Poppe *et al.*. Cross sections for the ${}^7\text{Li}(p,n){}^7\text{Be}$ reaction between 4.2 and 26 MeV. *Phys. Rev. C* **14**, 438 (1976).
- [37] S. G. Mashnik *et al.*. ${}^7\text{Li}(p,n)$ Nuclear Data Library for Incident Proton Energies to 150 MeV. arXiv: nucl-th/0011066 (2000).
- [38] G. Bizard *et al.*. Measurement of the cross section for stripping and dissociation of deuterons at 2.7 GeV/c on various nuclear targets (A between 9 and 207). *Nucl. Instrum. Meth.* **111**, 445 (1973).
- [39] B. S. Aladashvili *et al.*. Use of the deuteron beam for studying the dp interactions. *Nucl. Instrum. Meth.* **129**, 109 (1975).
- [40] E. Kuhlmann. Study of the Reaction $np \rightarrow pp\pi^-$ with a Deuteron Beam and Spectator Tagging. COSY-Proposal #116 (2002).
- [41] R. Bilger *et al.*. Spectator tagging in quasifree proton neutron interactions in deuterium using an internal cluster-jet target at a storage ring. *Nucl. Instrum. Meth. A* **457**, 64 (2001).
- [42] R. Schleichert. Study of ω -Meson Production in the Reaction $pn \rightarrow d\omega$. COSY-Proposal #114 (2002).
- [43] A. Khoukaz. Study of near threshold π^0 - and η -meson production in proton-neutron reactions at ANKE. COSY-Proposal #94 (2000).
- [44] P. Moskal. Investigation of the Glue Content in the η' -Meson. COSY-Proposal #100 (2001).
- [45] M. Hartmann. ϕ -meson production in proton-proton collision. COSY-Proposal #104 (2001).
- [46] M. Büscher. Investigation of Neutral Scalar Mesons a_0/f_0 with ANKE. COSY-Proposal #97 (2001).
- [47] F. Hibou *et al.*. Near-threshold production of omega mesons in the $pp \rightarrow pp\omega$ reaction. *Phys. Rev. Lett.* **83**, 492 (1999).
- [48] S. Abd El-Samad *et al.*. Production of omega mesons in proton proton collisions. *Phys. Lett. B* **522**, 16 (2001).
- [49] M. Büscher *et al.*. Study of ω - and ϕ -meson production in the reactions $pd \rightarrow dVp_{sp}$ at ANKE. COSY-Proposal #75 (1998).
- [50] R. Maier. Cooler synchrotron COSY - performance and perspectives. *Nuclear Instruments and Methods A* **390**, 1 (1997).

- [51] S. Barsov *et al.*. ANKE, a new facility for medium energy hadron physics at COSY-Juelich. Nucl. Instrum. Meth. **A 462**, 364 (2001).
- [52] V. Balanutsa *et al.*. Development of the ANKE pellet target. In Annual Report. Forschungszentrum Jülich (2002).
- [53] M. Mikirtychiants *et al.*. The polarized gas target for the ANKE spectrometer at COSY/Jülich. In Proc. 9th Int. Workshop on Polarized Sources and Targets (PST 01). Nashville, Indiana, USA (2001).
- [54] G. Riepe and D. Protic. Thick Silicon Strip Detectors. Nucl. Instrum. Meth. **A 226**, 103 (1984).
- [55] Inti Lehmann. Studies on a Detection System for Spectator Protons at ANKE. Master's thesis, Universität zu Köln. Int. Rep.: FZJ-IKP-IB-E2-1/2000 (2000).
- [56] V. Komarov *et al.*. First Module of the Forward Detector Proportional Chambers of the ANKE Spectrometer. In Annual Report, pages 67–68. Forschungszentrum Jülich (1996).
- [57] B. Chiladze *et al.*. The Forward Detector of the ANKE Spectrometer. Scintillation and Cherenkov Hodoscopes. Particles and Nuclei, Lett. **4** (2002).
- [58] A. K. Kacharava *et al.*. Beam test of Cerenkov counter prototype for ZDF setup. Nucl. Instrum. Meth. **A 376**, 356 (1996).
- [59] Ralf Schleichert. Entwicklung eines schnellen Triggersystems für das ANKE-Spektrometer am COSY-Speicherring in Jülich. Ph.D. thesis, RWTH Aachen (1996).
- [60] K. H. Watzlawik *et al.*. Control system for scalable experiments at COSY. IEEE Trans. Nucl. Sci. **43**, 44 (1996).
- [61] J.F. Ziegler, J.P. Biersack and U. Littmark. The Stopping and Range of Ions in Matter. IBM-Research, 96.xx edition (1999).
- [62] CERN, Genève, Switzerland. GEANT3: toolkit for Monte Carlo simulation of detectors in High Energy Physics.
- [63] Sergey Dymov. private communication (2002).
- [64] V. Komarov *et al.*. Exclusive Deuteron Break-up Study with Polarized Protons and Deuterons at COSY. COSY-Proposal #20 (1999).
- [65] V.M. Artemov *et al.*. Particle parameter determination at the ANKE spectrometer. In Annual Report. Forschungszentrum Jülich (1997).
- [66] A.D. Volkov *et al.*. Method for the calculation of charged particle momentum in magnetic spectrometers. Nuclear Instruments and Methods **A 306**, 278 (1991).
- [67] Sergey Yaschenko. private communication (2002).

- [68] M. Büscher, S. Dymov *et al.*. Momentum dependent efficiency of the forward Čerenkov counters at ANKE. In Annual Report, page 22. Forschungszentrum Jülich (2000).
- [69] Gogi Macharashvili. private communication (2003).
- [70] Sergey Barsov. private communication (2002).
- [71] Yu. Uzikov. Diffraction pd-scattering at COSY energies. In Annual Report. Forschungszentrum Jülich (2001).
- [72] Landolt-Börnstein. Numerical Data and Functional Relationships in Science and Technology, volume 9. Springer-Verlag. Page 294 (1980).
- [73] A. Khoukaz. private communication (2003).
- [74] H.J. Stein and D. Prashun. Determination of Effective Target Thickness and Luminosity from Beam Energy Losses at the ANKE Cluster Target. In Annual Report. Forschungszentrum Jülich (2001).
- [75] A. Schnase *et al.*. VXI-based Realtime Vectoranalyser with embeded Risc-Workstation. In Annual Report, page 188. Forschungszentrum Jülich (1997).
- [76] V. Komarov *et al.*. Proton induced deuteron breakup at GeV energies with forward emission of a fast proton pair. Phys. Lett. **B 553**, 179 (2003).
- [77] GSI, Darmstadt, Germany. PLUTO: A Monte Carlo simulation tool for hadronic physics (2000).
- [78] T. Hamada and I. D. Johnston. A Potential model representation of two nucleon data below 315 MeV. Nucl. Phys. **34**, 382 (1962).
- [79] M. Lacombe *et al.*. Parametrization of the deuteron wave function of the Paris $N - N$ potential. Phys. Lett. **B 101**, 139 (1981).
- [80] K. Hagiwara *et al.*. Review of Particle Physics. Physical Review **D 66**, 010001+ (2002).
- [81] Ye.S. Golubeva. private communication (2002).
- [82] Landolt-Börnstein. Numerical Data and Functional Relationships in Science and Technology, volume 12, page 97. Springer-Verlag. Reactions 71, 72 and 73.
- [83] A. Abdivaliev *et al.*. Analysis of the production mechanism of narrow enhancements in the effective mass spectrum ($\pi^+\pi^-$) in the reaction $np \rightarrow d\pi^+\pi^-$ at a neutron incident momentum of $P_n = 1.73$ GeV/c. Nucl. Phys. **B 168**, 385 (1980).
- [84] V. Yu. Grishina, L. A. Kondratyuk and M. Buscher. Near threshold omega and Phi meson production in $pn \rightarrow dM$ reactions and OZI-rule violation. Phys. Atom. Nucl. **63**, 1824 (2000).
- [85] K. Nakayama, J. Haidenbauer and J. Speth. The reactions $pn \rightarrow d\omega$ and $pn \rightarrow d\phi$ near threshold. Phys. Rev. **C 63**, 015201 (2001).

- [86] R. Schleichert, T. Krings, S. Merzliakov, A. Mussgiller and D. Protic. A self-triggering silicon tracking telescope for spectator proton detection. In 2001 IEEE Nuclear Science Symposium Conference Record, page 550 (2002).
- [87] Yuri Valdau. private communication (2003).
- [88] S. Okubo. Physics Letters **B 5**, 165 (1963).
- [89] G. Zweig. CERN Report 8419/TH 412 (1964).
- [90] I. Iizuka. Prog. Theor. Phys. Suppl. (1966).
- [91] J. Ellis, M. Karliner, D.E. Kharzeev and M.G. Sapozhnikov. Hadronic Probes of the Polarized Intrinsic Strangeness of the Nucleon (1999).
- [92] OBELIX collaboration. Yad. Fiz. (1996).
- [93] G. Bertolini and A. Coche, editors. Semiconductor Detectors. North-Holland Publishing Company - Amsterdam (1968).
- [94] H.F. Wolf. Semiconductors. Wiley, New York (1971).

Acknowledgements

I would like to thank:

- PROF. DR. H. STRÖHER who has spent time for giving advice and reading this thesis as my referee, and provided the possibility to do this work at the institute,
- PROF. DR. J. JOLIE for the consent to act as the co-referee,
- PROF. DR. C. KIEFER for the consent to act as the head of the examination commission,
- DR. RALF SCHLEICHERT for continuous advice day and night, many fruitful discussions, contributions and a lost year of his life,
- SERGEY BARSOV for large and valuable contributions to this work, effective help answering all questions at any time,
- VERA KLEBER for reading all the fragments of the work and helping in all details,
- COLIN WILKIN for a lot of proof reading in order to expunge the “Germanish” from this work and useful advice in physical topics,
- CHRISTOPH HANHART for many rectifications in scientific questions and help in understanding theoretical procedures,
- D. PROTÍĆ who produced and tested the thick micro-strip detectors and could help out with technical questions,
- MICHAEL, VOLKER, MARKUS, SERGEY α to ϵ , MISHA, and many others at the institute who could help out with many odds and ends or just provided a good atmosphere,

and last but not least:

- CORINNE and my FRIENDS who endured this stressed guy for so long and hopefully forgive my partial absence in personal matters.

Erklärung

Ich versichere, daß ich die von mir vorgelegte Dissertation selbständig angefertigt, die benutzten Quellen und Hilfsmittel vollständig angegeben und die Stellen der Arbeit – einschließlich Tabellen, Karten und Abbildungen –, die anderen Werken im Wortlaut oder dem Sinn nach entnommen sind, in jedem Einzelfall als Entlehnung kenntlich gemacht habe; daß diese Dissertation noch keiner anderen Fakultät oder Universität zur Prüfung vorgelegen hat; daß sie – abgesehen von unten angegebenen Teilpublikationen – noch nicht veröffentlicht worden ist sowie, daß ich eine solche Veröffentlichung vor Abschluss des Promotionsverfahrens nicht vornehmen werde. Die Bestimmungen dieser Promotionsordnung sind mir bekannt. Die von mir vorgelegte Dissertation ist von Herrn Prof. Dr. H. Ströher betreut worden.

Veröffentlichungen

- S. Barsov, I. Lehmann, R. Schleichert, C. Wilkin *et al.* „Near-threshold production of ω mesons in the $pn \rightarrow d\omega$ reaction“, eingereicht bei European Physical Journal.
- I. Lehmann, R. Schleichert, S. Barsov, A. Mussgiller *et al.* „Spectator Detection for the Measurement of Proton-Neutron Interactions at ANKE“, in Vorbereitung zur Veröffentlichung in Nuclear Instruments and Methods.

Lebenslauf



Name: **Inti Lehmann**
geboren am: 31.12.1971
geboren in: Juliaca – Peru

Eltern: Vater: Dipl. Ing. Konrad Lehmann
geb. am 7.12.1931 in Heidelberg
Bauingenieur
Mutter: Ursula Lehmann, geborene Gall
geb. am 21.12.1937 in Brühl
Volksschullehrerin

Promotion: Forschungszentrum Jülich
„ ω Meson Production in the $pn \rightarrow d\omega$ Reaction at ANKE“
ab März 2000

Diplom: Forschungszentrum Jülich
„Studies on a Detection System for Spectator Protons at ANKE“
Abschluß am 10. März 2000 mit der Gesamtnote „sehr gut“

Hauptstudium: Universität zu Köln
Wahlpflichtfächer: Kernphysik und Kristallographie
1996 – 1999

Auslandsstudium: University of Edinburgh – Schottland
1995/96

Grundstudium: Universität zu Köln
1993 – 1995

Zivildienst: Uniklinik Heidelberg
1991 – 1993

Schule/Jugend: Abitur 1991 Gesamtnote „gut“
1983-91 Heidelberg: Hölderlin-Gymnasium
1981-83 Arequipa – Peru
1979/80 Heidelberg
1977/78 La Paz – Bolivien
1975/76 Sana'a – Nordjemen
1971-75 Juliaca, Puno, Chiclayo – Peru